Development and Characterization of Nano-Structured $LiFePO_4$ Cathode and $Li_4Ti_5O_{12}$ Anode Materials for High-Performance Li-Ion Battery

by

Xiangcheng Sun

A thesis

presented to the University of Waterloo

in fulfillment of the

thesis requirement for the degree of

Doctor of Philosophy

in

Electrical and Computer Engineering

Waterloo, Ontario, Canada, 2015

AUTHOR'S DECLARATION

I hereby declare that I am the sole author of this thesis. This is a true copy of the thesis, including any required final revisions, as accepted by my examiners.

I understand that my thesis may be made electronically available to the public.

Abstract

Lithium-ion batteries with high power density and long lifetime is becoming the leading energy storage technologies for applications such as electric vehicles and large-scale electricity storage. But the state-of-the-art batteries based on current cathode and anode material can hardly meet the requirements of the large-scale applications due to the limitations on power density and safety characteristics.

My research has been dedicated to the development and characterization nano-cathode and nano-anode material for new-generation high power lithium-ion batteries. The selected material candidates for cathode is $LiFePO_4$ and that for anode is $Li_4Ti_5O_{12}$. The effective combination of solid-state reaction and hydrothermal method has been used to synthesize both $LiFePO_4$ cathode and $Li_4Ti_5O_{12}$ anode because of its low cost and availability of the precursors. The goal for my project is to elucidate the fundamental processes for controllable synthesis of stable $LiFePO_4$ cathode and $Li_4Ti_5O_{12}$ anode nanomaterials.

The first part of my thesis is the controllable synthesis and performance characterizations of carbon-coated $LiFePO_4$ nanomaterials. A variety of analytical techniques such as x-ray diffraction, scanning and transmission electron microscopy (TEM, HRTEM), electron diffraction, and X-ray photoelectron spectroscopy are applied to investigate $LiFePO_4$ morphologies and phase structures on the nanometer scale. Well-ordered olivine $LiFePO_4$ crystal with a homogenous carbon coating of ~ 3 nm thickness is clearly revealed. The state-of-the-art structural characterization techniques provide a comprehensive view of the correlation between structure and performance of these $LiFePO_4$ cathode nanomaterials. The nanostructures characteristics and the amorphous carbon-coating has been demonstrated to improve the electrical conductivity by reducing the path of both electron transfer and lithium ions diffusion, thereby is beneficial to improve electrochemical performance of these $LiFePO_4$ nanomaterials. The excellent performance in terms of enhanced rate capability, good cycling performance, and high discharge capacity, should enable the development of high power $LiFePO_4$ batteries. More importantly, the practical performance of these carbon-coated $LiFePO_4$ nanomaterials as cathode was performed with a prototype of 18650-type

battery cell manufactured by using the commercial graphite as the anode active materials. The remarkable rate capability and cycling performance are clearly demonstrated in the prototype of $LiFePO_4$ battery cell.

The second part of my thesis is the facile synthesis and performance evaluation of carbon-coated spinel $Li_4Ti_5O_{12}$ nanomaterials. Spinel $Li_4Ti_5O_{12}$ has been regarded as an attractive anode material for the development of high-power lithium-ion batteries because of its unique attributes of high safety and rate capability. Carbon-coating has been proved to be an effective method to improve electronic conductivity of $Li_4Ti_5O_{12}$ anode materials. It is critically important to investigate in depth the influence of the carbon-coating on the electrochemical performance. Comparative nanostructure analyses and various electrochemical testing demonstrated that these $Li_4Ti_5O_{12}$ anode nanomaterials have the improved capacitive, high-rate, and enhanced cycling performance. These improved lithium storage properties can be attributed to the combination of uniform thin carbon-coating and high-purity spinel $Li_4Ti_5O_{12}$ nanocrystal, which increases electron transport and facilitates lithium-ion insertion/extraction simultaneously throughout the electrode, making it a highly promising anode material for use in the development of high power density lithium-ion batteries. The practical comparison of the carbon-coated $Li_4Ti_5O_{12}$ nanomaterial and the commercial $Li_4Ti_5O_{12}$ sample was evaluated in half cells with lithium as the negative electrode. More interestingly, the improved cycling performance is demonstrated in the $Li_4Ti_5O_{12}$ battery cell.

Finally, the future outlook of the research directions and key developments of spinel $Li_4Ti_5O_{12}$ anode and olivine $LiFePO_4$ cathode are proposed from view of scientific project and industrial demand. The practical attempt is to investigate the effective combination of $Li_4Ti_5O_{12}$ anode and $LiFePO_4$ cathode to design the leading nano-battery of $Li_4Ti_5O_{12}/LiFePO_4$ with a high degree of safety, long cycle life and rapid charge for various potential applications. In addition, the prospect of newly development of graphene-$Li_4Ti_5O_{12}$ anode and graphene-$LiFePO_4$ cathode hybrid nanocomposite materials for next-generation of green and sustainable lithium-ion batteries is also presented in the last Chapter.

Acknowledgements

It is a great pleasure to acknowledge all the valuable contributions from many important people who made my PhD thesis possible and successful.

Firstly, I would like to thank the supervisor, Dr. Bo Cui, for giving me the opportunity and advice to develop the new generation nano-battery materials on both scientific and personal level. I would like to thank Dr. Hany Aziz, Dr. Yuning Li, Dr. Dayan Ban at University of Waterloo, and Dr. Xueliang Sun at University of Western Ontario, for being my committee members and offering me the valuable guidance during my PhD studying.

I am most grateful to Dr. Pavle Radovanovic and Dr. Juewen Liu for providing me the lab space, and to Dr. Ian Dean Hosein, Mr. Manu Hegde and Mr. Quansheng Quo for their supports on my sample and crystal model preparations at Department of Chemistry, University of Waterloo.

I am also grateful to Dr. Jian Wang for his valuable measurements in STXM imaging and XANES spectra in Canadian Light Sources at Saskatchewan.

I would like to acknowledge the important collaborators, Dr. Kai Sun, Dr. Haiping Sun at U of Michigan, USA, Dr. Bing Tan at IMRA America Inc, Dr. Miguel Jose Yacaman at U of Taxes, USA, Dr. Xuedong Bai, Dr. Yuefei Zhang, Dr. Lin Gu, Dr. Min He, Dr. Long Qie, Dr. Jun He, Dr. Jinyun Liao, Dr. Yongqing Wang, and Dr. Jie Shu in China for performing valuable structural and performance measurements.

I would also like to extend my sincere thanks to Mr. Celal Con, Dr. Katja Kleinke, Dr. Medrdad Irannejad, Mr. Ripon Dey, Dr. Jian Zhang, Mr. Mark Ferguson, and Ms. Lisa Nicole Hutfluss for their kind supports. A special thank also goes to all friends and group colleagues from University of Waterloo for their nice supports.

Scholarships from the Natural Sciences and Engineering Research Council of Canada (NSERC), President's Award of University of Waterloo, and Nano-fellowship from Waterloo Institute for Nanotechnology (WIN) are also greatly appreciated.

Lastly, but most importantly, I would like to thank my loved family; my dearest father; my loved mother; and my sincere sisters. To them I dedicate this thesis.

Dedication

To my loved family and my dearest father

Table of Contents

Lists of Figures

Lists of Tables

Chapter 1

Introduction and Background Overview

1.1 Why Batteries?

Energy production and storage has been and will continue to be one of the most important issues and societal challenges as the demands for advanced energy storage devices have dramatically increased due to the energy consumption continually in great scale. Energy consumption and supply has always been one of the crucial impact factors on our environment, human health and world's economy. As we know, conventional energy sources (coal, oil and natural gas) are diminishing and non-renewable. Moreover, massive consumption of fossil fuels leads to generation of CO_2 greenhouse gas, and further global warming and environmental degradation.[1] So it is initiated by the necessity to decrease the greenhouse gas emission and to take advantage of renewable energy sources. Thus, it will be crucial for us to aim at achieving sustainable, environmentally friendly and cheap energy supply by employing renewable energy technologies (solar energy, wind power, geothermal energy, biomass and biofuel, hydropower) associated with portable energy storage devices that can quickly capture and release energy. [1] Nowadays, advanced batteries technologies become the best positioned technology to deal with our efforts on sustainable environmental impact and renewable energy in our wide variety of applications from portable electronic consumer devices (e.g., cell phones, laptop computers) to electric vehicles and large-scale electricity storage in smart or intelligent grids (Figure 1.1).[1]

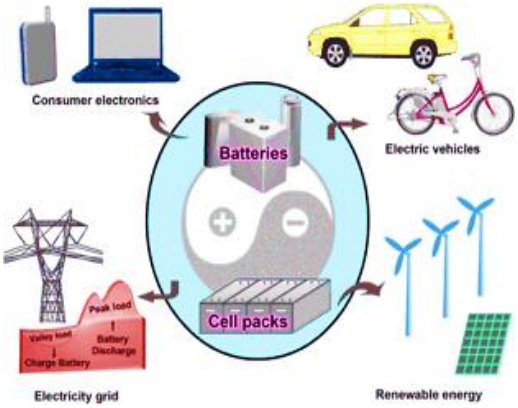

Figure 1.1 Schematic representations of applications for rechargeable batteries.[1]

1.2 How Battery Works?

A battery is a device that converts the stored chemical energy directly into electric energy by means of an electrochemical redox reaction.[2] In general, a battery may compose of one or more electrochemical cells that are connected in series and/or in parallel to provide the required voltage and capacity.[3] Each cell consists of three major components: positive electrode (cathode), negative electrode (anode) and electrolyte which conduct ions, as shown in Figure 1.2.

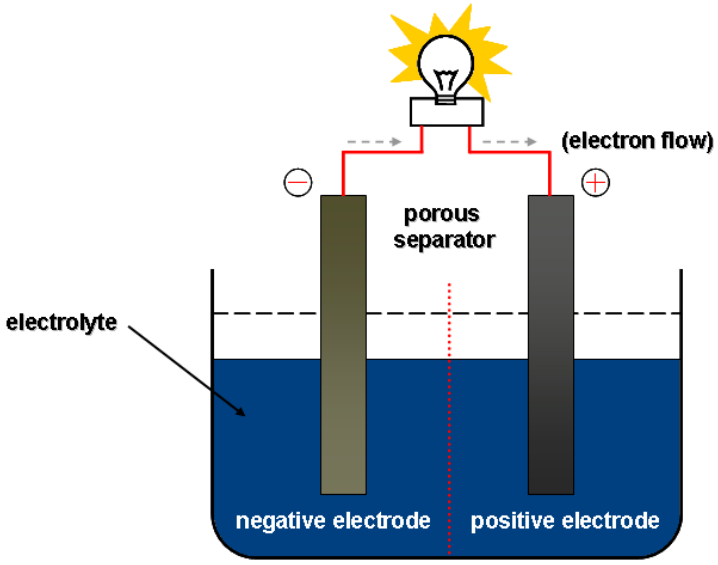

Figure 1.2 Schematics of the general principle of batteries

The electrolyte can be aqueous or non-aqueous, in liquid, paste or solid form.[2-5] When the cell is connected to an electricity consumer, the cathode supplies electrons (current) that flow through the consumer and are accepted by the anode. When the external load is removed the reaction stops.

1.3 Why Rechargeable Li-Ion Battery (LIB)?

Depending on their rechargeable capability, electrochemical batteries (or cells) are identified as primary or secondary batteries. Primary batteries can only be used once, and not capable of being recharged electrically. For example, alkaline-manganese dioxide battery and zinc-carbon battery are typical primary batteries. The batteries with rechargeable capability are classified as secondary batteries. Major secondary batteries include

rechargeable lead-acid, Ni-Cd, Ni-MH (M-metal) and lithium ion batteries. **Table 1.1** shows the comparison of performance characteristics of these secondary batteries.[6] Compared with other secondary batteries, rechargeable lithium ion batteries show excellent electrochemical performance, which leads to their predominant position in the present battery industry. This also explains why lithium ion batteries receive most attention at both fundamental and applied levels.

Table 1.1 Comparison of performance characteristics for secondary batteries [6]

Battery type	Voltage (V)	Energy density (Wh/kg)	Energy density (Wh/L)
Ni-Cd	1.2	40	100
Ag-Zn	1.5	110	220
Ni-MH	1.2	90	245
Li-ion	3.6	155	400
Li-polymer	3.6	180	380

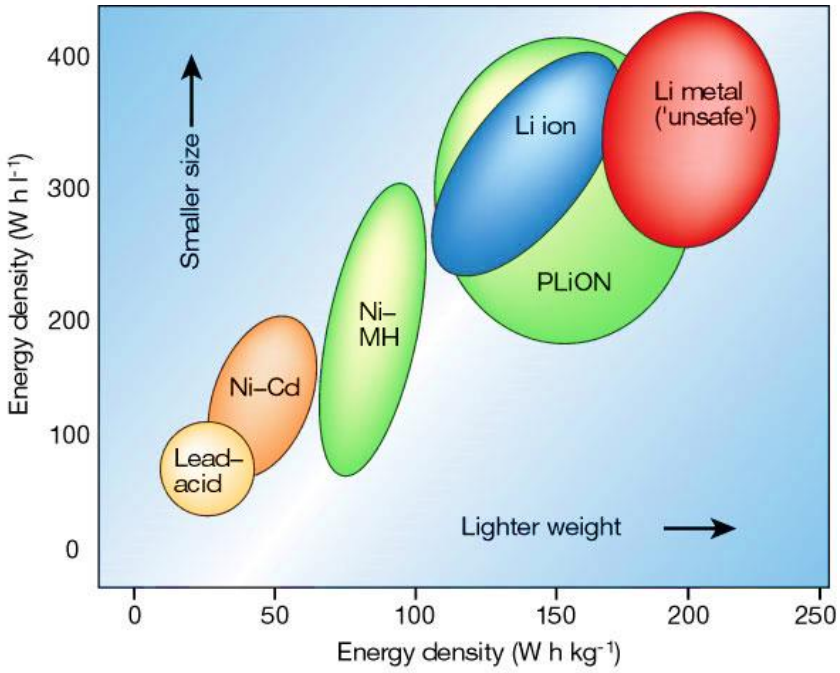

Figure 1.3 Comparison of various secondary batteries in terms of volumetric and gravimetric energy density. [3]

So far, among various existing technologies (e.g., lead-acid, nickel-cadmium, metal-lithium), rechargeable lithium-ion batteries (LIBs) have the advantage of high voltage, long cycling life, high power, high reliability and design flexibility (see Figure 1.3).[7,8] The significance and popularity of the rechargeable lithium-ion batteries are definitely resulted from its unique advantages offered over other secondary batteries:

- Lighter than other rechargeable batteries for a given capacity
- Li-ion chemistry delivers a high open-circuit voltage
- Low self-discharge rate (about 1.5% per month)
- Do not suffer from battery memory effect
- Environmental benefits in rechargeable and reduced toxic landfill

1.4 Working Principle of Li-Ion Battery

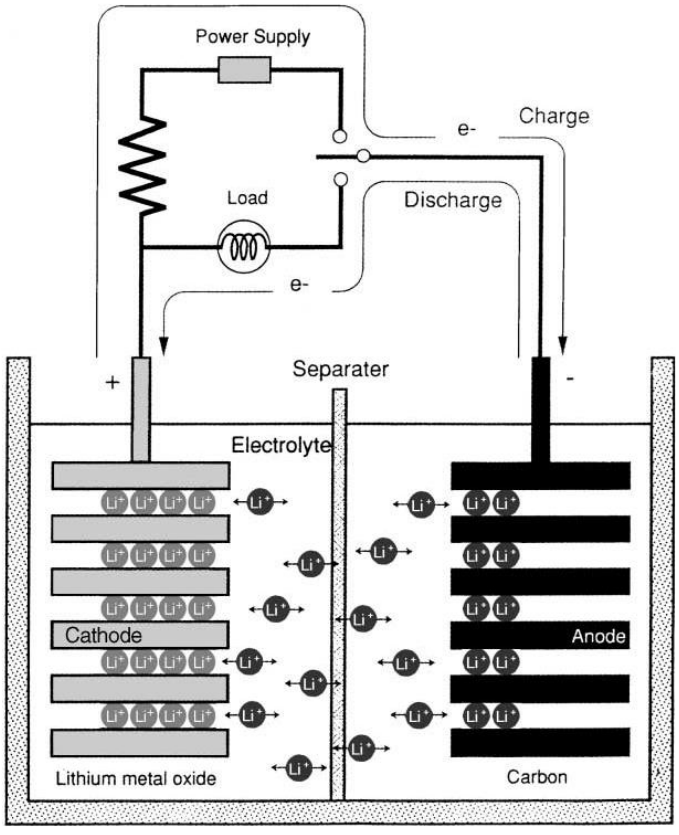

Figure 1.4 General working principle of the charging/discharging process of a rechargeable lithium-ion battery. [10,12]

In general, there are five components that constitute a lithium-ion cell. These components are two electrodes, electrolyte, and two current collectors. The main function of the electrodes is to be reduced or oxidized over a potential range measured in volts (V). The electrolyte serves as an ionic conductor between the electrodes and must be electronically insulating. The current collectors are an electrically conducting material, usually a metal that are directly in contact with each electrode. The current collectors are attached to each other by an external circuit (see Figure 1.4). [3,9]

A lithium-ion battery exhibits the electrochemical cell functions because of the potential difference between the two electrodes. It is energetically favorable for the two electrodes to come towards an equilibrium potential that is lower than the initial open-circuit cell potential where they are stable. Equilibrium between the electrodes is achieved by the oxidation of one electrode and the reduction of the other electrode. The electrode that is reduced is called the cathode, while the electrode that is oxidized is called the anode. These reactions are accomplished by two distinct paths for ions and electrons. The electrons travel through the external circuit from the anode to the cathode. At the same time, the ions travel in the same direction as the electrons between the two electrodes through the electrolyte. This completes the redox reaction of the two electrodes, as showed clearly in Figure 1.4.

Generally, the basic working principle of lithium-ion batteries is based on lithium ion (Li^+) reversible de-intercalation and intercalation processes between two electrodes.[10] As a result, during charge/discharge, Li^+ ions flow between the anode and the cathode, enabling the conversion of chemical energy into electrical energy and the storage of electrochemical energy within the battery. Here, the electrolyte should be ionically conducting and electronically insulating, however the actual properties of the electrolyte is much more complicated. During the first cycle, a solid–electrolyte-interphase (SEI) layer will be formed on the surface of electrodes due to the decomposition of organic electrolyte.[10,11] The typical electrochemical reactions involved in a typical LIB cell are described in Figure 1.4.

The charge/discharge mechanism of a LIB is also recognized as a “rocking chair” concept as Li^+ ions “rock” back and forth between anode and cathode. [10,12,13] As is shown in

Figure 1.4, lithium ions are shuttled between anode and cathode through the electrolyte during the charging and discharging processes. Lithium ions de-intercalate from the cathode into the electrolyte during the charging process under an applied current. Simultaneously, an equivalent amount of lithium ions from the electrolyte intercalate into the anode. The reverse reaction proceeds spontaneously when the battery is discharged. On both of the charging and discharging process, charge compensation is supplied by the external circuit supply.

1.5 Requisite for Cathode and Anode Materials

Many principal parameters of a LIB, e.g., energy density (Wh/kg or Wh/L) and current density strongly depend on the battery cell capacity and ionic-electronic transport properties, which is defined by crystallographic structure of both cathode and anode materials in term of lithium intercalation reaction. Therefore, it is not surprising that battery cell capacity and energy density are consequently defined by the cathode and anode materials. The number of charge and discharge cycles and cell lifetime are controlled by the processes taking place on electrode materials/electrolyte interfaces. Furthermore, safety is the function of the stability of the electrodes and electrode/electrolyte interfaces. Thus, the key for building better lithium-ion batteries with high energy density, long life, and light weight, low cost and environmental compatibility lies in the chemistry parameters of anode and cathode materials.[3]

Therefore, the performance of rechargeable LIBs depends on active materials employed for Li ions storage in both electrodes. The way for substantial improvement of electrochemical performance and principal parameters for the LIBs is absolutely to improve and upgrade the anode and cathode materials. In general, to become the suitable candidate of cathode and anode material in LIBs, the active materials should demonstrate the following specific characteristics.[14]

(a) An open structure to permit reversible lithium migration

In brief, the working principle of LIBs is the reversible migration of lithium ions between cathode and anode accompanied by a redox process, and its reversibility is the

prerequisite to LIBs. Thus, the structure of the compound should be open for lithium insertion into its lattice.

(b) Stability of electrode and electrolyte

This is the requirement for a long cycle life. Both insertion and extraction of guest lithium ions into and from host compound should ideally maintain original host structure. On the other hand, the oxidation of electrolyte should be avoided during cycling and no change in structure during over-charge/discharge.

(c) A higher specific energy density

The specific energy density (per weight or per volume) is related to both the working voltage and the reversible capacity. The former depends on the potential of the redox process and the latter is restricted by the reversible amount of lithium intercalation. The available redox pair should offer a high and suitable potential range and the structure of material should be stable in wide composition range in order to obtain a high capacity.

(d) Higher electrode conductivities

The electrochemical lithium insertion/extraction reactions involve both lithium ions diffusion in the lattice and charge transfer process on the particle surface. Thus, electrode's conductivity includes both lithium ion conductivity and electronic conductivity of electrode. Higher electronic conductivity is helpful to keep the inner resistance low and give a high power density.

(e) Low cost and environmentally benign

The cost and environmental impact should be always kept in mind for new battery design. It is one of the future challenges to develop cheaper and hazardless electrode materials with excellent battery performances.

Today, global research groups and companies are trying to optimize new cathode and anode for new rechargeable LIBs, which are usually constructed with various shapes (e.g., cylindrical, coin, or prismatic shapes). The comparison of various popular cathode and anode materials in terms of voltage and capacity is summarized in Figure 1.5.[3] Basically, compounds with a working potential of higher than 3 V can be potentially used as cathode

(positive), and lower than 1V as anode (negative) materials in lithium ion battery. In current commercialized LIB technology, the battery cell voltage and capacity are mainly determined by the cathode materials. The developments of cathode materials therefore become extremely crucial. Since 1980 when the $LiCoO_2$ was demonstrated firstly as a possible cathode material for rechargeable lithium battery, the transition metal intercalation oxides have caught the major research interests as the LIB cathodes. The conventional cathode materials can be classified into three different crystal structures: α-$NaFeO_2$ structure of layered transition metal oxides compounds $LiMO_2$ (M = Co, Ni, Mn, and e.g. $LiCoO_2$, $LiNiO_2$, $LiNi_{1/3}Mn_{1/3}Co_{1/3}O_2$), spinel structure compounds (e.g. $LiMn_2O_4$), and olivine structure compounds $LiMPO_4$ (M = Fe, Mn, Ni, Co, and e.g. $LiFePO_4$). Most of the researches are performed on these materials and their derivatives. Some research reports of new structure of intercalation materials such as silicates and borates are also gaining the attentions in recent years.[1,11]

During the materials optimization and development, the following designing criterions are considered: (1) energy density; (2) rate capability; (3) cycling performance; (4) safety; (5) cost. The energy density is determined by the material's reversible capacity and operating voltage, which is mostly determined by the material intrinsic chemistry such as the effective redox couples and maximum lithium concentration in active materials.

The working voltages and charge/discharge capacities of the most popular cathode materials are summarized in Table 1.2.[15] For anode materials, so far a variety of alternative anode materials have been extensively investigated in order to develop next-generation LIBs with high capacity, fast power capability and long cycle life. It includes carbonaceous materials (nano-carbons, carbon nanotubes, and graphene), metal alloys, and metal oxides/sulfides, as reviewed by several recent review papers.[16-17]

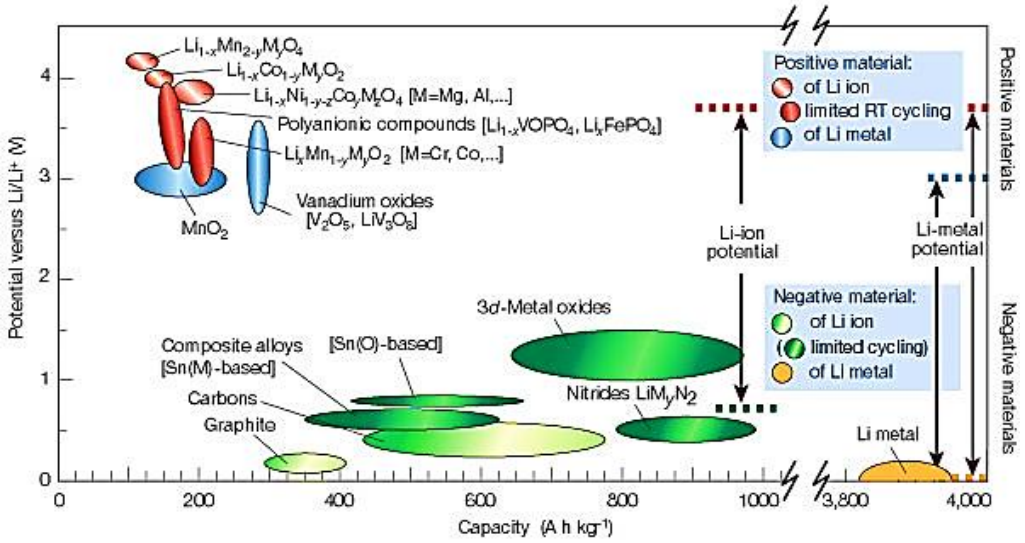

Figure 1.5 Voltage versus capacity for cathode and anode materials presently used or under serious considerations for rechargeable Li-ion cells. [3]

Table 1.2 Comparison of various cathode materials for lithium ion battery[15]

Structure	Cathode materials	Average Voltage	Practical capacities (mAh/g)	Cost	Safety
Layer	$LiCoO_2$	4V	130~140	high	acceptable
	$LiNiO_2$	4V	~220	high	unstable
	$LiNi_{1/3}Co_{1/3}Mn_{1/3}O_2$	4V	180~220	high	acceptable
	$LiNi_{0.5}Mn_{0.5}O_2$	4V	160~200	acceptable	acceptable
Spinel	$LiMn_2O_4$	4V	130~140	acceptable	good
	$LiCoMnO_4$	5V	130~140	acceptable	unstable
Olivine	$LiFePO_4$	3.5V	150~160	low	excellent
	$LiMnPO_4$	4V	~150	acceptable	excellent

1.6 Research Objectives

The main objectives of this research are to develop and characterize nanostructured novel cathode and anode material for new-generation green and sustainable lithium-ion battery system, as well as their emerging applications for high-power stationary backup

systems and/or advanced electric vehicles (EVs). My main research efforts are focused on optimizing the experimental synthesis process of those novel nano-cathode and nano-anode material in order to design the new-generation lithium-ion battery with improved energy/power density, high safety and long-cycle life. As well, my research is to provide a comprehensive understanding of the correlations of controllable synthesis, nanostructure, and improved performance of those novel nano-cathode and nano-anode materials.

The following are the specific objectives of this study:

1. Optimize novel electrode material candidates of $LiFePO_4$ cathode and $Li_4Ti_5O_{12}$ anode.
2. Study the fundamental processes of solid-state reaction and hydrothermal method for the controlled synthesis of both nano-$LiFePO_4$ cathode and nano-$Li_4Ti_5O_{12}$ anode with low cost precursors.
3. Investigate the effective strategies of combinational surface coating and nano-structuring on high-volume synthesis of carbon-coated nano-$LiFePO_4$ cathode and nano-$Li_4Ti_5O_{12}$ anode with desirable coating-thickness and enhanced electronic conductivity.
4. Investigate both nanostructure and morphologies of stable olivine-$LiFePO_4$ cathode and spinle-$Li_4Ti_5O_{12}$ anode materials at nano-scale or atomic scale using advanced analytical techniques such as scanning-transmission electron microscopy and scanning-transmission x-ray microscopy.
5. Investigate fundamental electrochemical kinetic behavior and characteristics as well as the effect of critical factors (e.g. phase, size and coating) on the electrochemical performance of both nano-$LiFePO_4$ cathode and nano-$Li_4Ti_5O_{12}$ anode.
6. Preform the practical application measurement for the prototype battery cell designed from those carbon-coated nano-$LiFePO_4$ cathode and nano-$Li_4Ti_5O_{12}$ anode.

1.7 Thesis Organizations

The organizations of this thesis is as follows:

1. Chapter 1 reviews the current Li-ion batteries, the existing cathode and anode materials and major challenges of its limitations for large-scale applications; and proposes the main

objectives of the development of novel nano-cathode and nano-anode material for the new-generation Li-ion battery.

2. Chapter 2 introduces the working principles of various analytical techniques for nanostructured electrodes characterization and electrochemical performance measurement.
3. Chapter 3 reviews briefly the existing cathode materials including layered $LiCoO_2$ cathode and olivine $LiFePO_4$ cathode; and summarizes various effective approaches to improve the performance of bulk $LiFePO_4$ cathode.
4. Chapter 4 reviews briefly the current popular anode materials including carbon, metal alloy, and spinel $Li_4Ti_5O_{12}$; and highlights the effective approaches to improve the performance of bulk $Li_4Ti_5O_{12}$ anode.
5. Chapter 5 presents the controlled synthesis of carbon-coated $LiFePO_4$ cathode and the improved electrochemical performance. It is demonstrated that nano-structuring and amorphous carbon-coating improved the electronic conductivity, thereby enhanced battery performance by reducing the path of both electron transfer and lithium ions. The practical performance of an 18650 type-$LiFePO_4$ prototype battery cell is evaluated.
6. Chapter 6 presents the facile in-situ synthesis, advanced characterizations and improved electrochemical performance of carbon-coated $Li_4Ti_5O_{12}$ anode materials. It is demonstrated that the improved lithium storage performance can be attributed to the synergistic effects of uniform carbon-coating and high-purity spinel $Li_4Ti_5O_{12}$ nanocrystal. The practical performance of such a $Li_4Ti_5O_{12}$ half-cell battery is tested.
7. Chapter 7 presents the overall conclusion, concluding remarks, and the outlook of promising new-generation of nano-Li-ion-battery from a scientific and practical point of view.

Chapter 2

Characterization Methods and Techniques

2.1 Structure and Physical Characterization

2.1.1 X-ray Diffraction

X-ray diffraction (XRD) is the most common technique for characterizing crystalline materials. The well-known Bragg's law (see Figure 2.1 and equation 2.1) was firstly introduced to precisely explain the diffraction pattern arising from the X-ray reflections on crystal planes.[18]

The term of powder implies that the crystalline domains are randomly oriented in the samples. The peaks positions and the different peaks intensities of the diffraction patterns are used to identify the crystalline structure or phase of the materials. In crystalline materials different (see Figure 2.1) sets of planes (coloured lines in the graphs) are formed by periodically arranged electron shells of atoms (blue spheres). These planes are able to interact with the incident X-ray beam (red lines) by forming constructive or destructive interferences.

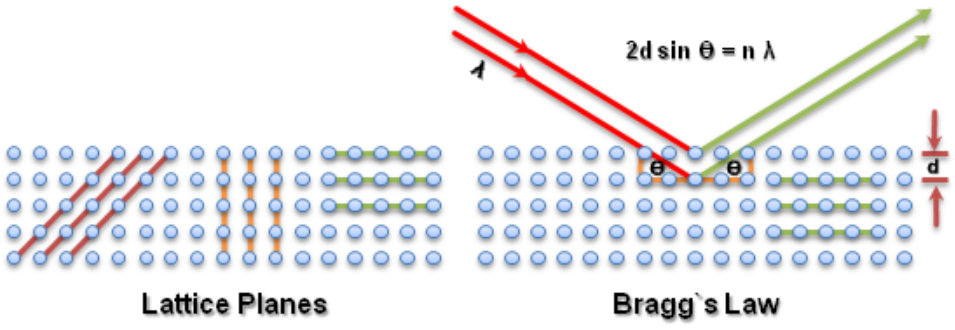

Figure 2.1 Schematics of Bragg`s Law for the scattering of X-rays at periodic crystal lattice planes [18]

The Bragg's Law is one of most important laws used for interpreting X-ray diffraction data.[18] For a given set of lattice planes with an inter-plane distance of *d*, the condition for

constructive interference, resulting in a diffraction peak, can be simply written as (Equation 2.1):

$$\mathbf{n \cdot \lambda = 2d \cdot \sin\theta} \qquad 2.1$$

Where λ is the wavelength of the X-ray beam, θ represents the angle between incident X-ray beam and crystallographic planes, and n an integer representing the order of the diffraction peak. With two parallel X-ray beams diffracted on parallel atomic planes a distance of d apart, the deeper beam travels an extra distance of $2d \cdot \sin\theta$, which is a multiple of the X-ray wavelength (λ) and an integer (n), if the two beams are in phase. Various d spacing of crystallographic planes can be obtained by scanning θ. When a beam of X-ray interacts finely with the atoms in sample, there must be a fraction of crystals with crystallographic planes orientated with a Bragg angle θ, at which Bragg diffraction can take place. With sample stage rotating with respect to the incident X-ray beam, a XRD pattern containing characteristic diffractions can be recorded by a detector. Such a XRD diffraction pattern is a fingerprint useful for identifying the crystal characteristic such as size, crystallinity, lattice parameters and phase with the help of a comprehensive XRD database.[19]

In this thesis study, XRD is used to identify crystal phases and calculate average particle size. The XRD patterns are collected on a Bruker D8-Advantage powder diffractometer equipped with a graphite monochromator and a nickel filter, operating at 40 kV and 30 mA, using Cu-Kα radiation (the wavelength λ = 0.154 nm). The conventional scan rate was 0.05° per second from $2\theta = 10^{o}$ to 80^{o}, while the high resolution scan rate was 0.02° per 8 seconds from $2\theta = 10^{o}$ to 80^{o} for refinement purposes.

2.1.2 Transmission Electron Microscopy (TEM)

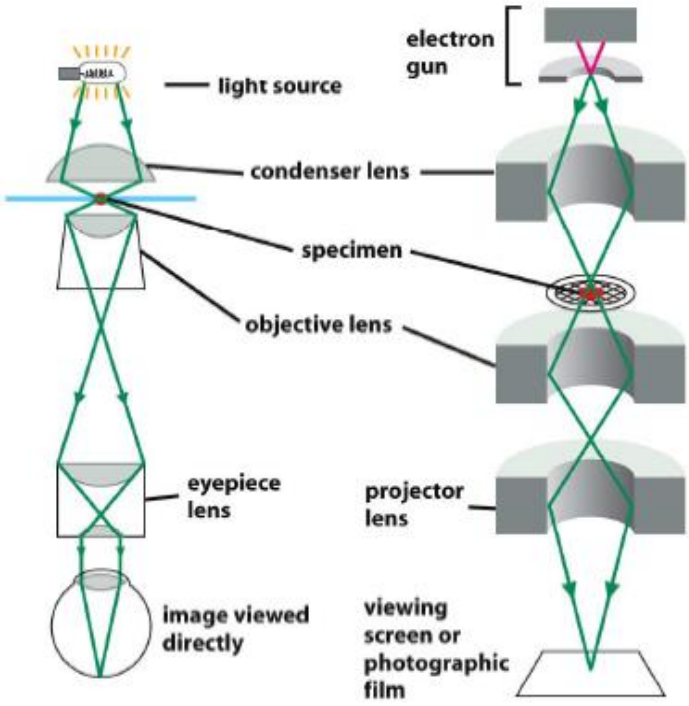

Figure 2.2 Comparison of the illumination system of TEM and light microscopy [20]

A conventional TEM uses a beam of highly energetic electrons to examine objects on a very fine scale. Morphology and crystallographic information can be obtained by TEM.[20] Figure 2.2 compares the illumination system for TEM and light microscopy, TEM has significantly higher resolution than light microscopy.[20] The Rayleigh criterion defines the light or electron microscopy resolution,[21] which is given by:

$$\mathbf{R = 0.61}\,\frac{\boldsymbol{\lambda}}{\boldsymbol{n\,sin(\theta)}} \qquad 2.2$$

Where λ is the wavelength of the radiation, n is the refractive index of the view medium and θ is the semi-angle of collection of the magnifying lens. In a TEM (n=1), emitted electrons are accelerated under higher voltage to achieve a small wavelength (for 200kV, λ = 0.0025nm) for high-resolution TEM imaging that can approach to atomic scale.

Fundamentally, TEM imaging method is to utilize the information contained in the electron waves transmitted through the sample to form an image.[20] In the standard TEM operation, by adjusting the condenser lens and the objective lens as well as the objective aperture, two basic TEM imaging modes can be realized (see Figure 2.3(a, b, c)).[22] The first is the bright-field mode (BF-TEM) (Figure 2.3(b)), where the transmitted beam (un-diffracted beam) contributes to the image; the second one is the dark-field imaging mode (DF-TEM) (Figure 2.3(c)), where a diffracted beam is selected (transmitted beam excluded) to form the image.[20, 22]

When a large objective aperture is selected that allows both the diffracted and the transmitted beams to pass through, another type of image is formed by the interference of the diffracted beams with the direct transmitted beam (see Figure 2.3(d)). While the imaging conditions are properly adjusted (lens defocus, image astigmatism, incident beam alignment) and also a suitable crystalline sample is oriented along a zone axis, high-resolution TEM lattice image (HR-TEM) is obtained by this way. Since transmitted beam interferes with one or more diffracted beams and the contrast for the HR-TEM image depends on the relative phases of the various beams, such an imaging mode is often referred as phase contrast imaging. HR-TEM imaging has been proven to be effective in determining the atomic arrangements within the nanostructures.

In this thesis study, both JEOL-JEM-2100F and JEOL-3010F transmission electron microscopes equipped with both energy-dispersive x-ray spectroscopy and electron energy loss spectroscopy are used to produce TEM images (BF-TEM, DF-TEM), HR-TEM images, and electron diffraction patterns on the particles samples.

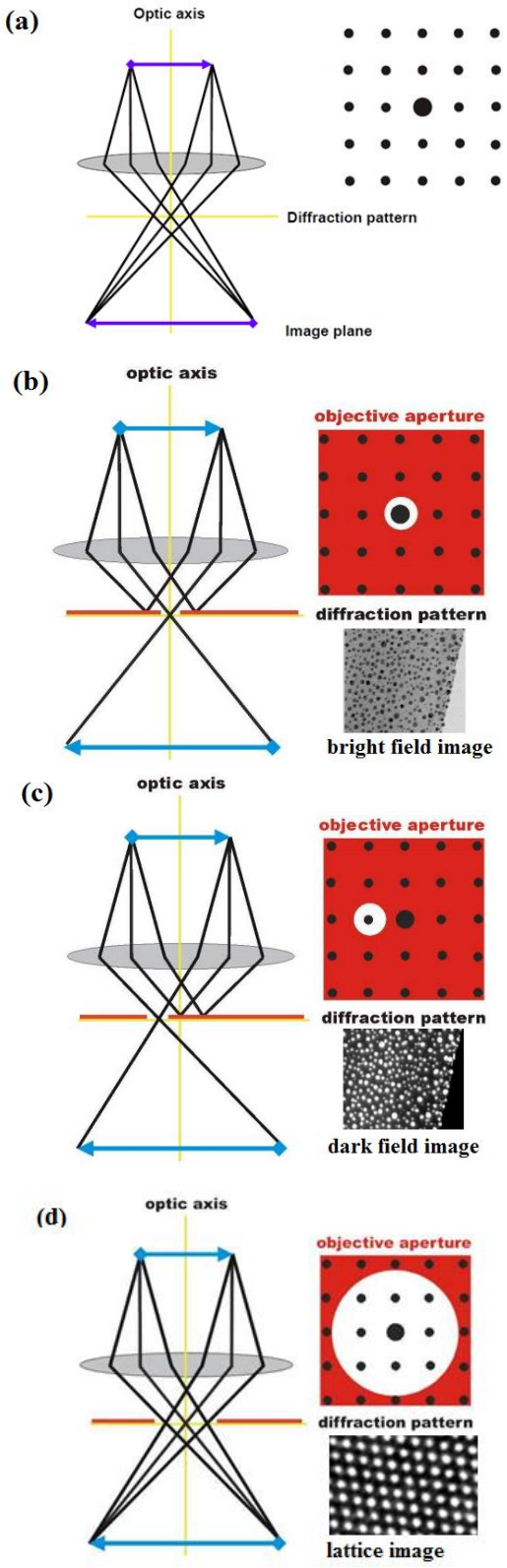

Figure 2.3 (a ,b, c) Schematic diagram of the TEM imaging modes by diffraction contrast, (d) Schematic diagram of the TEM imaging modes by phase contrast.[22]

2.1.3 Scanning Transmission Electron Microscopy (STEM)

Scanning transmission electron microscopy (STEM) was developed in the 1950s.[23] A STEM is distinguished from a TEM by focusing the electron beam into a narrow spot which is scanned over the sample in a raster. [23] Schematic drawing of the formation of a STEM images model is shown at Figure 2.4. The rastering of the beam across the sample makes the microscope suitable for analysis techniques such as mapping by electron energy loss spectroscopy (EELS) and imaging by high-angle annular dark-field imaging (HAADF). These signals can be obtained simultaneously, allowing direct correlation of image and quantitative data. By using a STEM-HAADF imaging, it is feasible to form atomic-resolution images, where the contrast is directly related to the atomic number of the elements (i.e., "Z-contrast" image, HAADF-STEM imaging).[23] This is in contrast to the conventional high resolution electron microscope technique, which uses the phase-contrast to form the HR-TEM images.

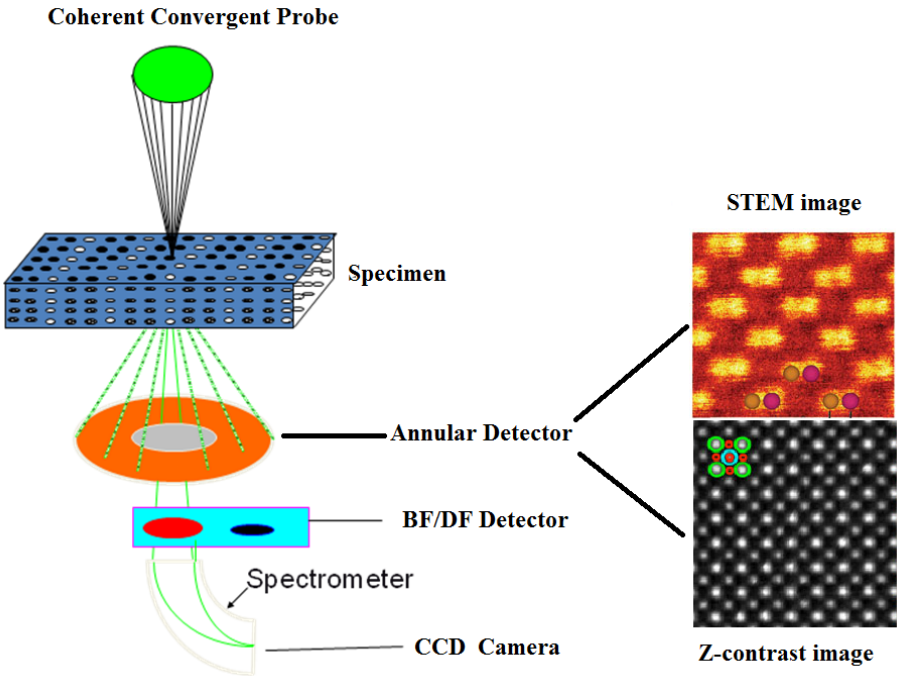

Figure 2.4 Schematic drawing of atomic-scale image formation model in a STEM.[23]

In this thesis study, an aberration-corrected scanning transmission electron microscope (JEOL-2100F, STEM/TEM) operated at 200 kV is used to obtain the STEM-HAADF images at nanoscale or atomic-scale for the particles samples.

2.1.4 Electron Energy Loss Spectroscopy (EELS)

In a TEM or STEM, when a sample is exposed to a beam of electrons with different range of kinetic energies, some of the electrons will undergo inelastic scattering, which means that they lose energy and their paths are deflected slightly and randomly, as showed in Figure 2.5. The amount of energy loss can be measured via an electron spectrometer and interpreted in terms of what caused the energy loss. Such a technique is called electron energy loss spectroscopy (EELS).[24]

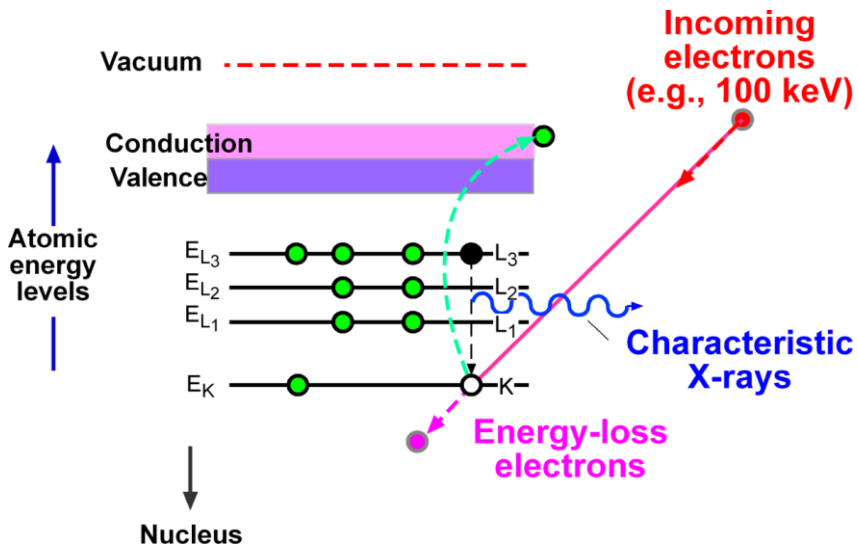

Figure 2.5 Ionization process due to inelastic scattering

In order to perform EELS, it is necessary to detect very small differences in the kinetic energies of the electrons. This is accomplished by using a magnetic prism that exerts a centripetal force on each electron, causing a circular motion. In addition to

detecting/quantifying particular elements in a sample, EELS also provides detailed information such as the electronic structure, bonding, and nearest neighbour distribution of the atoms in the sample,[24] as typically shown with zero-loss peak, low-loss region and high-loss region in the Figure 2.6. It is amazing to note that, EELS signals can be obtained simultaneously together with an atomic-resolution STEM image, and it is often referenced as being complementary to energy-dispersive x-ray spectroscopy (EDX).

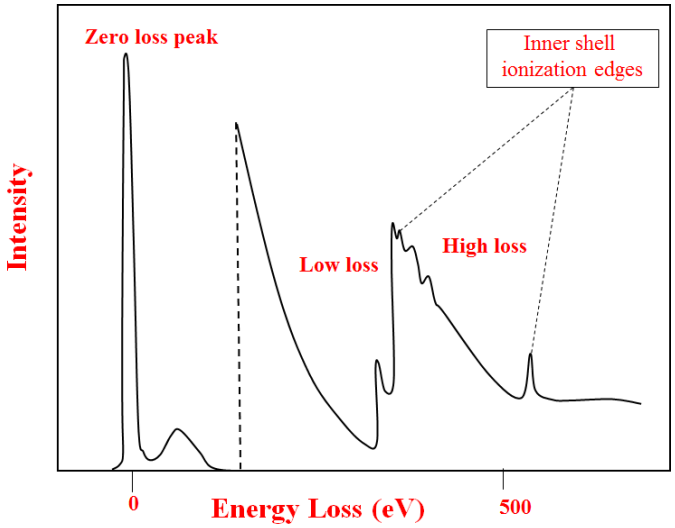

Figure 2.6 The representative of a typical EELS spectrum with zero-loss peak, low-loss region and high-loss region.

2.1.5 X-ray Photoelectron Spectroscopy (XPS)

Kai M. Siegbahn,[25] who won the Nobel Prize in physics in 1981 for his research, developed X-ray photoelectron spectroscopy (XPS) in the 1960s. XPS reveals which chemical elements are present at the surface and the nature of the chemical bond that exists between these elements. XPS is a quantitative spectroscopic technique that measures the elemental composition, chemical state and electronic state within a material. Photoemission principle is as: when an X-ray bombards a sample, some electrons of the sample become excited enough to escape the atom, as shown in Figure 2.7 (a). The chemical state of an atom

alters the binding energy (BE) of a photoelectron which results in a change in the measured kinetic energy (KE). The BE is related to the measured photoelectron KE by the simple equation; BE = hν – KE – F, where hν is the photon (x-ray) energy, and F is the work function, as shown in Figure 2.7 (b).

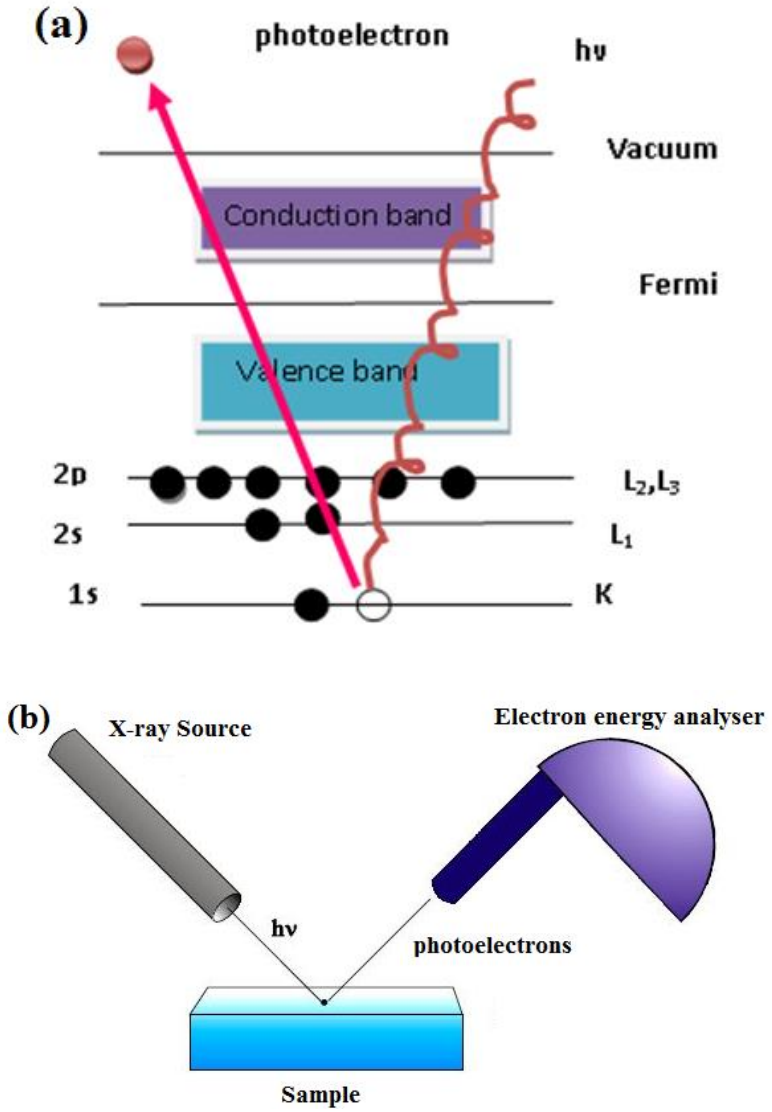

Figure 2.7 (a, b) The XPS working principle and signal measuring technique [26]

The chemical or bonding information of the element is derived from these chemical shifts. XPS spectra [26] are obtained by irradiating a material with a beam of X-rays while

simultaneously measuring the kinetic energy and number of electrons that escape from the top 1 to 10 nm of the material being analyzed under ultra-high vacuum (UHV) conditions.

Normally, XPS is a surface chemical analysis technique to analyze the surface chemistry of a material in its initial state and post-treatment such as ion beam etching, or to measure for elemental composition of the surface chemical or electronic state of each element in the surface and uniformity of elemental composition across the top surface (or line profiling or mapping).

In this thesis study, X-ray photoelectron spectrometer (XPS) was used to analyze sample surface chemistry by a Kratos ULTRA DLD XPS with a mono-chromated Al source that gives an energy resolution better than 0.5 eV. The binding energy scale was calibrated by setting the P peak as the inner standard.

2.1.6 X-ray Absorption Spectroscopy (XAS)

a). XAS is a widely used technique for determining the local geometric and/or electronic structure of matter. The experiment is usually performed at synchrotron radiation sources, which provide intense and tunable X-ray beams. XAS can yield information about the type, number, and arrangement of scattering atoms. In this thesis research, the XAS technique was used to probe the electronic structure of the titanium in its crystalline surroundings.

XAS data are obtained by tuning the photon energy to a range where core electrons can be excited (0.1-100 keV photon energy). The "name" of the edge depends upon the core electron which is excited: the principal quantum numbers n=1, 2, and 3, correspond to the K-, L-, and M-edges, respectively. For instance, excitation of a 1s electron occurs at the K-edge, while excitation of a 2s or 2p electron occurs at an L-edge, as shown in Figure 2.8.

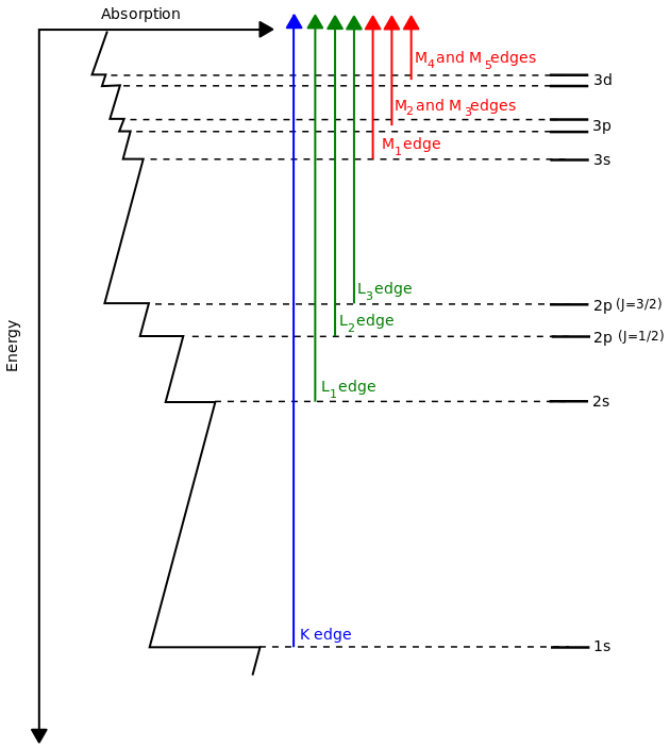

Figure 2.8 Transitions that contribute to various edges of X-ray absorption spectroscopy.

XAS is a type of absorption spectroscopy from a core initial state with a well-defined symmetry. Since the binding energy of core electrons is element specific, XAS is element and core level specific (e.g. Si K-edge at 1840 eV is the 1s electronic excitation threshold of silicon). [27]

As core electron is excited with hv > the threshold (E_o), it is excited to a final state defined by the chemical environment, which modulates the absorption coefficient relative to that of a free atom. This modulation is known as the X-ray absorption fine structures (XAFS), XAFS contains all the information about the local structure and bonding of the absorbing atom. XAFS study requires a tunable X-ray source–synchrotron radiation.[28] Among XAFS, the spectral region near the edge, which is indicative of a core excitation, is called XANES (X-ray Absorption Near-Edge Structures),[28] and extends to roughly 40 eV above the edge. The oscillations in the XANES spectrum provide information on vacant orbitals, electronic configuration and the site symmetry of the absorbing atom. Because the

shielding of the core electrons depend on the occupation of the other electronic levels, the absolute position of the edge is directly linked to the oxidation state of the element and the electronic structure of the absorbing atom, including valence, the local environment, and valance changes of the elements. XANES can supply detailed information on the electronic structure and the local chemistry of the absorbing atom.

b). Scanning Transmission X-ray Microscopy (STXM)

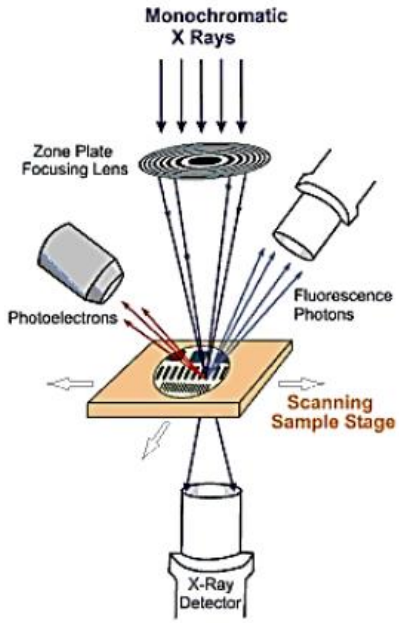

Figure 2.9 Schematic illustration of a typical STXM

STXM is a synchrotron-based spectromicroscopy technique that combines the analytical capabilities of XANES spectroscopy with high spatial resolution. A STXM, based on the X-ray absorption process, has a chemical contrast mechanism to allow for imaging at the nano-scale. A simplified view of STXM is shown in Figure 2.9. A Fresnel zone plate focuses mono-energetic X-rays provided by a suitable monochromator beamline mounted on a suitable, bright synchrotron source. The focal point is typically 50 nm in diameter over a 3-10 mm waist. An image is generated by monitoring the X-ray signal transmitted through a thin section of a specimen as it is raster-scanned at the focus of the x-rays. Micro-spectra are measured by holding the beam at the spot of interest on the sample while the photon energy is scanned. Synchrotron-based STXM with nanometer resolution has effectively provided

an excellent combination of microscopic examination and chemical/electronic structure speciation via XANES spectroscopy.[29,30] Spectro-microscopy studies were done using STXM, allowing for the generation of the spectra with high spectral and spatial resolution. So the combination of STXM/XANES has a major impact exploring the structure and the composition of element phases with spatial information.

In this thesis study, both XANES spectrum and STXM imaging have been done in Canadian Light Sources at Saskatchewan (Canada). There, synchrotron radiation provides the X-rays that are used for a wide range of analytical techniques. Beamlines that offer X-ray beam size at micron or sub-micron dimensions are available.

2.2 Electrodes Preparation

2.2.1 Electrode Foils Fabrication

When testing electrode materials, thin sheets are fabricated for ease of handling and assuring optimal electrochemical performance. In order to fabricate the sheets of cathode and anode, the electrode material is casted onto a thin sheet of metal substrate (Al or Cu foil) that will serve as a current collector. A poly-vinyl diflouride (PVDF) polymer is used as binder glue between the powder and the substrate. The mixture of active materials and binder materials are well mixed by mortar or pestle. Slurry is formed when liquid n-methyl pyrroli-done (NMP) is added to this mixture. This liquid acts as a solvent towards the PVDF binder and will evaporate out of the mixture once heated. The amount of NMP used for the slurry depends on the amount of graphite and the active material used in the mixture. The doctor-blade technique is used to form the electrode film, then the film is placed in an oven at 120^{o}C to remove the NMP. The final film has a good balance between the active material and the current collector.

2.2.2 Coin Cell Fabrication

The cathode or anode testing material in the form of an electrode foil film, Li metal (counter electrode), and a polyethylene separator sheet are punched out as disks. These disks are placed in a coin cell can in the following sequence: electrode foil film, separator, and Li

metal. A gasket spring is inserted into the cell can along with a flat metal disk that sits on top of the electrode stack. Liquid Li-conducting electrolyte is added before the cell can is sealed. Finally, the coin cell lid is crimped into the can using the gasket as a seal. Schematic diagram of the coin-cell assembly is shown in Figure 2.10.

In this thesis study, the cathode foil film or anode foil film was prepared using a mixture comprising of 80 wt% active cathode or anode materials, 10 wt% acetylene black, and 10 wt% polyvinylidene fluoride (PVDF) binder. The electrolyte is a 1M solution of $LiPF_6$ in ethylene carbonate/dimethyl carbonate (EC/DMC, 1:1). All the cells (half-cell) were assembled and handled in an Ar-filled glove box.

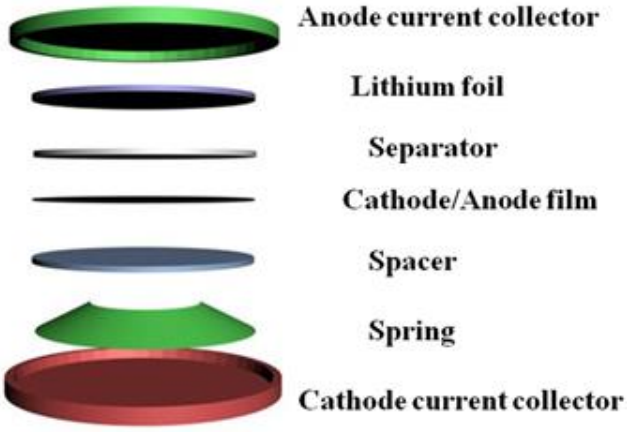

Figure 2.10 Schematic diagram of the coin-cell assembly

2.3 Electrochemical Characterizations

2.3.1 Galvanostatic Discharge/Charge Tests

Because of its potential stability, Li metal can be used as a reference electrode. In addition, Li metal provides a large Li source for the cell and thus can be used as a counter electrode as well.

In this thesis study, all the potentials for the cathode or anode material at half-cell coin battery is measured against the potential of Li metal. In the galvanostatic mode, a constant current is applied to a cell. Voltage is recorded as a function of the number of lithium ions insertion and extraction from electrodes. The current direction is inverted at the trigger cut-

off potentials. Electrode characteristics, such as discharge capacity and rate capability can be determined by this technique. In this thesis study, cathode materials are characterized in coin-type half-cell using a program-controlled LAND Cell test-2001A system between 2.5 V and 4.2 V versus the Li metal counter electrode (anode); anode materials are studied in coin-type half-cell using a galvanostatic/potentiostat between 1.0 V and 3.5 V versus the Li metal counter electrode (cathode).

2.3.2 Cyclic Voltammetry (CV)

CV is a type of potentiodynamic electrochemical measurement,[31] and is one of the most frequently used electrochemical methods because of its relative simplicity and its high information content. During the CV testing, a cyclic linear potential scan (i.e., electrode potential ramps linearly versus time) is imposed onto the electrode and the resulting current is recorded (see Figure 2.11(a)). This ramping is known as scan rate (V/s). A current-voltage curve (or cyclic voltammogram) shows the current response as a function of voltage rather than time (see Figure 2.11(b)), which can give information on the kinetics and thermodynamics of the electrode reaction. The simplest system involves a reversible redox reaction with single electron transfer in a solution medium where the forward and reverse reaction rates are close to equilibrium. CV is often used to reveal diffusion-controlled process in which the electroactive species insert into the electrode. The chemical diffusion coefficient of lithium ion in the electrode is calculated from the CV data. In short, CV is a convenient tool for obtaining qualitative information about electron transfer processes, as well as a rapid method for obtaining good estimate of reduction potentials and formation constants.

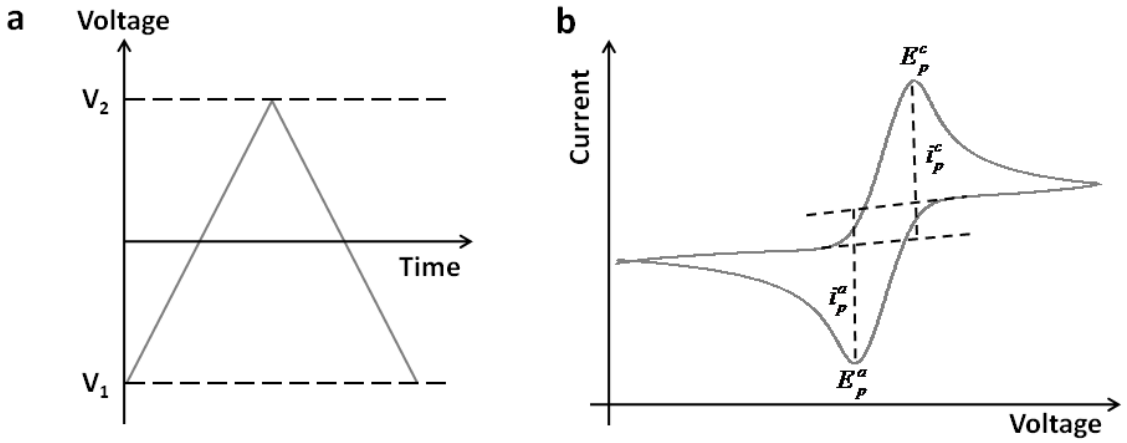

Figure 2.11 (a, b) Typical cyclic voltammogram for a reversible redox process.

2.3.3 Electrochemical Impedance Spectroscopy (EIS)

EIS is a very powerful tool for the analysis of electrochemical complex systems. This technique measures the impedance of a system over a range of frequencies. The EIS method is based on the frequency dependences of the electrochemical cell impedance, which is the opposition to the flow of alternating current (AC) in a complex system.

The EIS data expression is composed of a real and an imaginary part. If the real part is plotted on the X-axis and the imaginary part is plotted on the Y-axis of a chart, a "Nyquist plot" is obtained (see Figure 2.12). Such an interpretation of Nyquist plot can be carried out using an equivalent circuits (EC), which is used to determine the kinetic behavior and diffusion parameters for an electrochemical system.[32] So far the EIS method has been broadly applied to investigate the reversible lithium intercalation into electrodes for LIBs, which is related to the diffusion kinetics of lithium ions in electrodes.[33,34]

Figure 2.12 shows the typical Nyquist plot of an electrochemical system.[35] Basically, the Nyquist plot has an intercept at high frequency, followed by a depressed semicircular in the medium-to-high frequency region and a ~45^{o} sloping line in the low frequency region.

The intercept at the Z_{re} axis in the high frequency region was attributed to the Ohmic resistance, representing the resistance of the electrolyte. The semicircular plot in the medium frequency range is associated with the charge transfer resistance (R_{ct}) of the electrochemical reaction, and the ~45° sloping line in the low frequency region represents the Li-ions diffusion within electrode, namely the Warburg impedance. The Warburg impedance is independent of frequency.

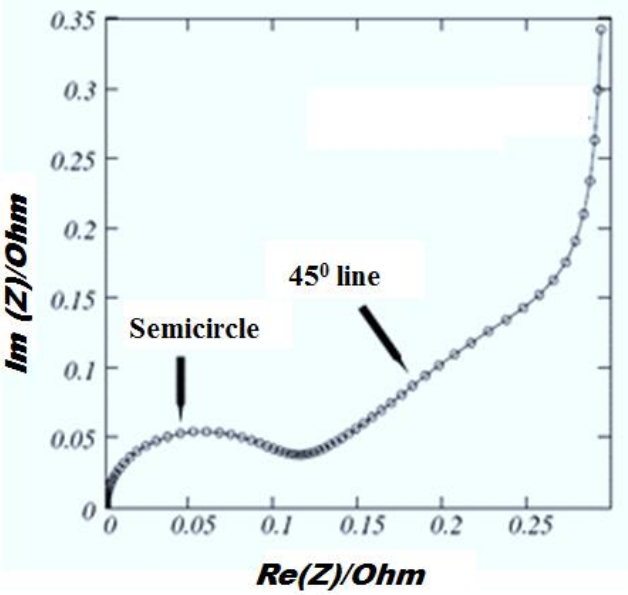

Figure 2.12 A typical Nyquist plot of an electrochemical system.

Chapter 3

Cathode Materials for lithium ion battery

Cathode materials that have high theoretical potentials as the candidates of future generation LIBs are always under intensive studies. Many significant property improvements have been achieved during the past decade with assistance of newly developed technologies. In this chapter, following up the structural category on battery cell chemistry, the research progress of various cathode materials in the past decade is briefly discussed in order to provide inspiring perspectives for the cathode material optimizations.

3.1 Layered transition metal oxides

As stated in Chapter 1, the layered metal oxides have a general formula of $LiMO_2$ (M = transition metal such as Co, Ni and Mn), in which the Li ion and M ion occupy the alternate (111) planes of the rock salt structure. The structure has an oxygen stacking sequence of …ABCABC… along the c axis and the Li and M ions occupy alternatively the octahedral sites. There are three MO_2 sheets per unit cell. This structure can be described as a layered structure with a space group of R3m, and the unit cell parameters are usually defined in terms of the hexagonal setting.[13,14,36] An ideal schematic structure of layered compound $LiMO_2$ is presented in Figure 3.1. The structure with MO_2 layers allows a reversible extraction/insertion of lithium ions from/into the lithium layer.

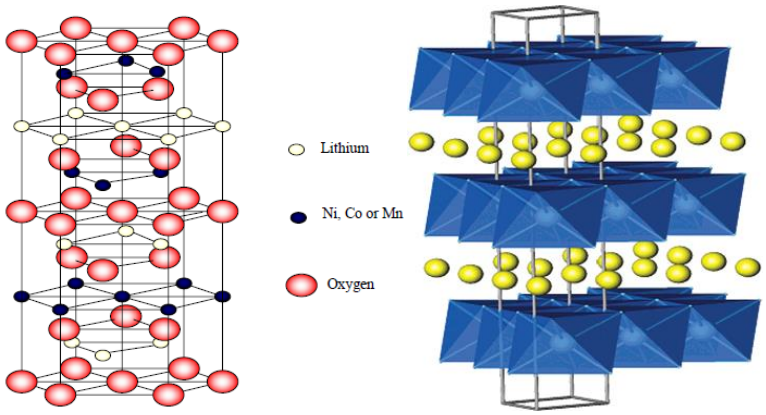

Figure 3.1 Schematic model of an ideal layered $LiMO_2$ structure. [12, 13]

3.2 Layered $LiCoO_2$

Among the layered metal oxides, $LiCoO_2$ has attracted particular attention. $LiCoO_2$ was first reported by Goodenough's group[13] in early 1980s. Since then, it has received tremendous development due to its reasonably high capacity, long cycle life, and ease to synthesize. After intensive R&D work, SONY successfully commercialized $LiCoO_2$ cathode lithium ion battery with a carbon anode (C-$LiCoO_2$) in 1991. It was then considered a 'mature' cathode material, though there were still a lot of studies to improve the stability and safety.

$LiCoO_2$ has 2D crystal structure of the α-$NaFeO_2$ structure (R3m) with consecutive alternating CoO_2 and Li layers,[37-39] and the oxygen atoms are in a cubic close-packed arrangement (see Figure 3.2). The lattice parameters of $LiCoO_2$ crystal are a = 2.8161 Å and c = 14.0536 Å. Both Co and Li are octahedrally coordinated. [37-39]

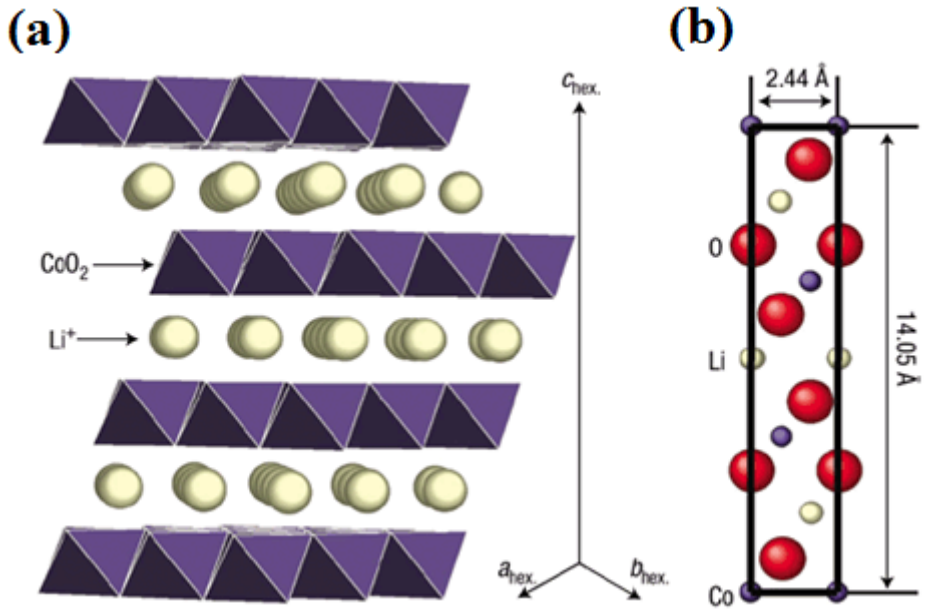

Figure 3.2 a), Layered structure $LiCoO_2$ where lithium ions lie horizontally between CoO_2 octahedra, **b**), Projection along the [110] zone axis shows lithium, cobalt and oxygen atoms in columns.[39] The projected cell is 2.44 Å by 14.05 Å. A cubic-close-packed oxygen array provides a two-dimensional network of edge shared CoO_2 octahedra for Li^+ ions.

$LiCoO_2$ is at present the most popular active cathode materials in commercial lithium ion rechargeable batteries, with a high gravimetric energy density as high as 120-150 Wh/kg (two to three times that of usual Ni-Cd batteries) because of its high voltage (4V) and moderate specific capacity. Carbon is usually used as the anode. Non-aqueous electrolyte is a better choice since it is stable at high charge voltage (~ up to 4.5 V). The voltage variation and chemical reactions taken place in the cell can be described as the following in Figure 3.3 (a, b): [8,13,14]

Anode:

$$xLi^+ + xe^- + 6C \underset{\text{Discharge}}{\overset{\text{Charge}}{\rightleftharpoons}} Li_xC_6$$

Cathode:

$$LiCoO_2 \underset{\text{Discharge}}{\overset{\text{Charge}}{\rightleftharpoons}} Li_{1-x}CoO_2 + xLi^+ + xe^-$$

Overall:

$$LiCoO_2 + 6C \underset{\text{Discharge}}{\overset{\text{Charge}}{\rightleftharpoons}} Li_{1-x}CoO_2 + Li_xC_6$$

Generally, $LiCoO_2$ can deliver a high operating voltage plateau, and if all of the Li^+ can be extracted, it gives a theoretical capacity of 274 mAh/g corresponds to extraction of 1 mole of Li^+ from the $LiCoO_2$. However, only a little over half of the theoretical capacity is practically reversible for intercalation/de-intercalation (< 4.2 V vs Li/Li^+) when charged and discharged. Complete removal of lithium from $LiCoO_2$ can't be accomplished due to a series of phase transformation, such as hexagonal and monoclinic occurred when the cathode is charged above 4.2V.[40-42] This phase transformation leads to the deterioration of cycling performance.[14]

The practical chemical reactions taken place in the cell can be described as:

- Overall reaction on a Li-ion cell: $0.5C_6 + LiCoO_2 \leftrightarrow 0.5LiC_6 + Li_{0.5}CoO_2$
- At the cathode: $Li_{0.5}CoO_2 + 0.5Li^+ + 0.5e^- \leftrightarrow LiCoO_2$
- At the anode: $0.5C_6 + 0.5Li^+ + 0.5e^- \leftrightarrow 0.5LiC_6$

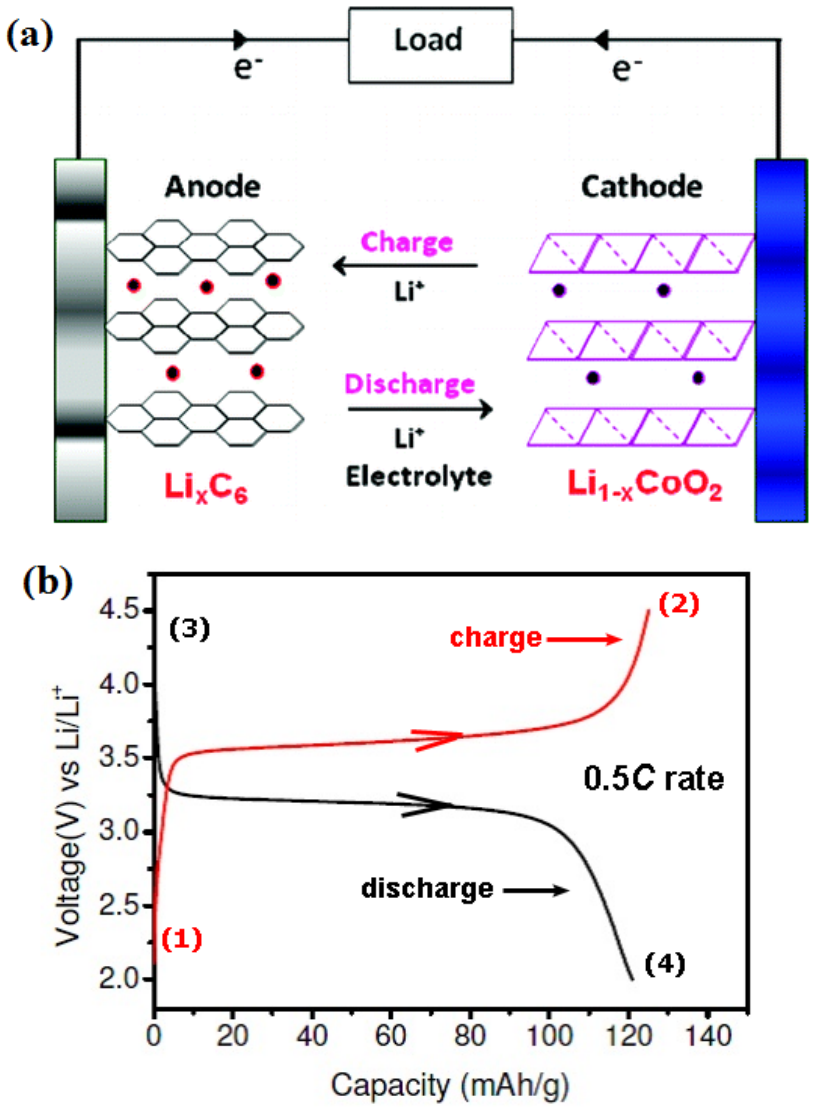

Figure 3.3 (a), Schematic representation of a typical commercial $LiCoO_2$ lithium-ion battery showing the discharge intercalation mechanism with graphite as the anode. [8,13,14] (b), A discharge-charge voltage profile (one cycle from mark 1 to mark 4) recorded at current density of 0.5*C* rate, here a "*C*" rate is defined as full theoretical lithium discharge/charge in one hour.

Moreover, several other reasons for the capacity degradation during cycling have been reported.[43,44] For example, some capacity degradation can be attributed to side reaction, as cobalt is dissolved remarkably at high voltage of > 4.2 V, from oxide compound into

electrolyte when the $LiCoO_2$ is delithiated during charging,[45] such a less lithium can be intercalated during the discharging process, which results in lower capacity for lithium intercalation.

In order to suppress phase transformation and obtain higher capacity, many works of substitution of foreign elements such as Mg,[46,47] Ni,[48-51] and Mn[52,53] for Co in the new type of M-$LiCoO_2$ have been conducted. In particular, Zou et al reported that small amount of foreign element can give stable cycling performance due to suppression of phase transformation at 4.2 V during intercalation/de-intercalation process at higher cut-off voltage of 4.5 V.[54,55] Nowadays, Mg doped $LiCoO_2$ has been proven quite successful to be widely used for the commercial lithium ion battery in application of portable devices (e.g., cell phones, digital cameras, laptops). In addition, it has been found that the cycle ability (cycling rate) of the $LiCoO_2$ cathode material could be improved significantly by modifying its surface with metal oxide such as Al_2O_3 and ZrO_2.[56,57]

Recently, there has been a dramatic increase in research and commercialization activities of lithium ion batteries for large scale energy storage in electric vehicles (EV) and hybrid electric vehicles (HEV). Challenges remain in making low-cost and high-safety lithium ion batteries for vehicle applications. Large scale applications of $LiCoO_2$ material in EV and HEV are prohibited due to its safety risk, high cost, and environmental concern.[11,58,59] Alternative cathode materials (e.g., olivine lithium iron phosphate, $LiFePO_4$) need to be investigated and developed for auto-transportation applications (HEV and EV).[60,61]

3.3 Olivine Structure $LiFePO_4$

Polyanion-based compounds, $Li_xM_y(XO_4)_z$ (M = metal, X = P, S, Si), are now regarded to be the most promising cathode materials for LIBs with improved energy density and power density as well as an extended cycle life. Among them, lithium iron phosphate, $LiFePO_4$, has been so far most studied since its discovery in 1997.[62] As a cathode for rechargeable LIBs, this new cathode material has attracted much attention because of its high energy density, high thermal stability at full state-of-charge, low cost and

environmental friendliness. The olivine $LiFePO_4$ now stands as a competitive candidate of cathode material for the next generation of a green lithium-ion battery system due to its long life span, abundant resources, low toxicity, and high structural stability. Since the pioneering work of Li^+ intercalation in $LiFePO_4$ by John B. Goodenough and his co-workers at University of Texas in 1997,[62-64] numerous works have been done to study its synthesis, structure, and physical, electrochemical properties.[3,65-67]

3.3.1 Structure and Chemical Properties of LiFePO4

The olivine structure of $LiFePO_4$ crystal, as shown in Figure 3.4, consists of a poly-oxyanionic framework containing LiO_6 octahedra, FeO_6 octahedra and PO_4 tetrahedra. Strong P-O covalent bonds in $(PO_4)^{3-}$ polyanion stabilize the oxygen when fully charged and avoid O_2 release at high states of charge, making $LiFePO_4$ a stable and safe cathode material.[62]

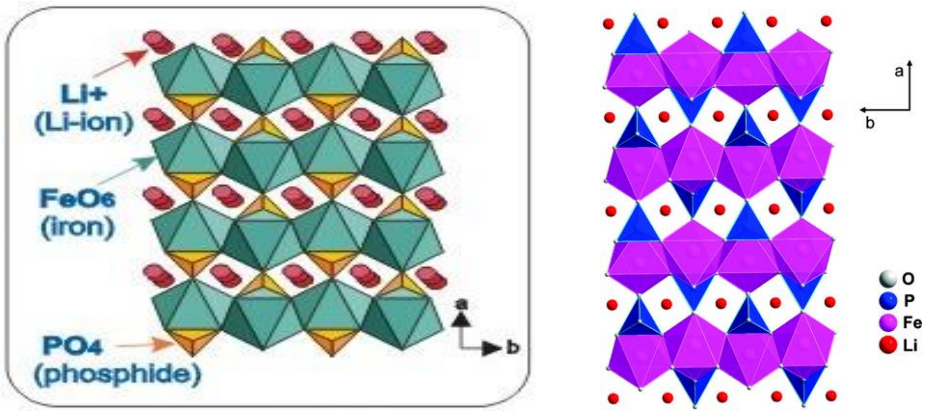

Figure 3.4 The olivine structure of $LiFePO_4$ in projection along [001], showing the FeO_6 octahedra, PO_4 tetrahedra, and one-dimensional tunnels in which the lithium ions reside.[62,68]

Electrochemical extraction of lithium from the $LiFePO_4$ phase to the isostructural $FePO_4$ phase is completed by a direct first-order transition during charge and discharge process,[62-64] as shown in Figure 3.5 and Figure 3.6, in which the Fe^{2+} ions are oxidized to

Fe^{3+}, leaving the olivine framework intact. The total reversible redox reaction may be written as:

$$LiFePO_4 - xLi^+ - xe^- \leftrightarrow Li_{1-x}FePO_4$$

There is no structural change during lithium insertion and extraction. The Fe-P-O bonds in $LiFePO_4$ are stronger than the Co-O bonds in $LiCoO_2$ and thus the oxygen atoms are much harder to remove, which leads to a higher stability upon short-circuit and overheating in real applications.

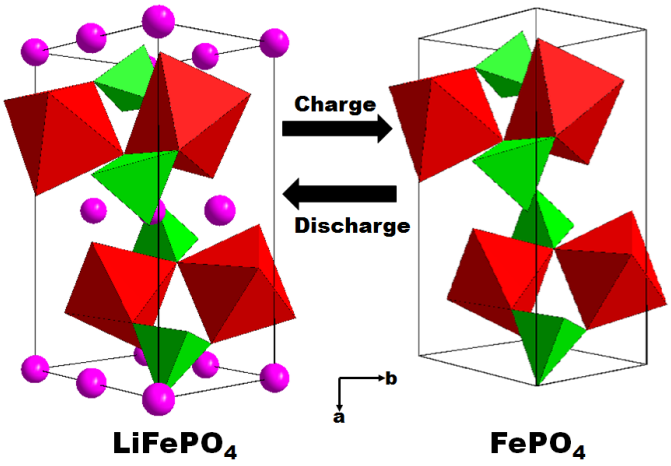

Figure 3.5 Structure transformation of $LiFePO_4$ and $FePO_4$ during charge/discharge

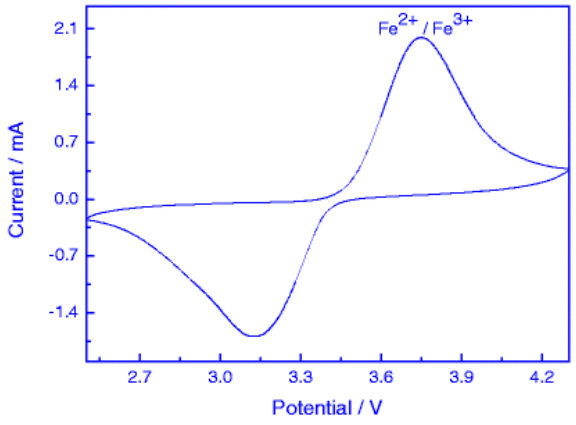

Figure 3.6 Cyclic voltammograms of $LiFePO_4$ at a scan rate of 0.1 mV/s between 2.5 V and 4.3 V (vs. Li/Li^+).[69]

In addition, as compared with the capacity of 140 mAh/g for $LiCoO_2$, the $LiFePO_4$ battery cell has a discharge potential around 3.4 V vs lithium and high energy density of 170 $mAhg^{-1}$, with excellent cycling stability of up to 2000 cycles and good availability of the abundant Fe resource in natural sources. [3,62-64,68]

It is also clear from Figure 3.5 that the cation arrangement in $LiFePO_4$ differs from that in the layered $LiCoO_2$. The divalent Fe^{2+} ions occupy the corner-shared octahedral; the P^{5+} is located in tetrahedral sites, and Li^+ resides in chains of edge-shared octahedra. The skeleton of PO_4 polyanions is very stable thermally, but the corner-shared FeO_6 octahedra of $LiFePO_4$ are separated by the oxygen atoms of the PO_4^{3-} tetrahedra and cannot form a continuous FeO_6 network, which results in the poor electronic conductivity of $LiFePO_4$.[70] At room temperature, the electronic conductivity of pristine $LiFePO_4$ is only 10^{-9} to 10^{-10} S/cm,[71] which is much lower than those of $LiCoO_2$ (~10^{-3} S/cm).[72] Atomistic modeling and first-principle calculations indicate that the lowest Li migration energy is found for the pathway along the [010] channel, with a nonlinear, curved trajectory between adjacent Li sites (Figure 3.7).[38,73]

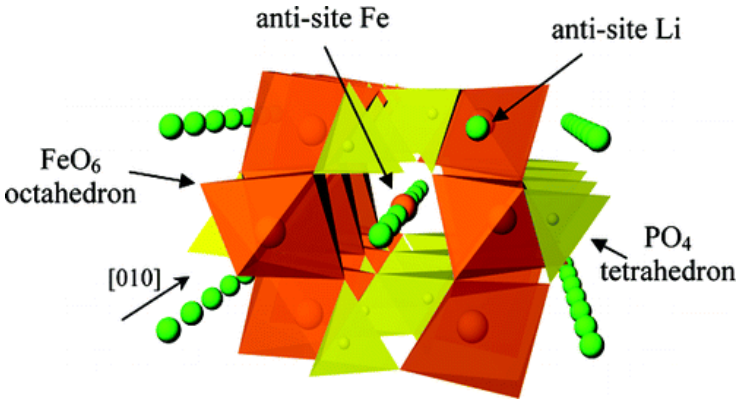

Figure 3.7 Structure of $LiFePO_4$ depicting curved trajectory of Li^+ transport along the [010] axis.[38]

Although the theoretical calculation showed that the intrinsic ionic diffusion coefficient is as high as 10^{-8} ($LiFePO_4$) to 10^{-7} ($FePO_4$) cm^2/s, the one-dimensional channels

are easily blocked by impurities because blockages in one-dimensional paths are different from those in three-dimensional paths where Li ions can move around the blocked sites.[74] The ionic diffusion coefficients in $LiFePO_4$ are therefore lower than the theoretical value. Takeda et al reported that the diffusion coefficients are in a wide range of 10^{-15} to 10^{-12} cm^2/s with electrochemical impedance spectroscopy.[75,76] Apparently, the low electronic and low ionic conductivities dictate the slow kinetics of charge and discharge.

Various models have been proposed to explain the mechanism and kinetics of Li^+ intercalation/de-intercalation during charge and discharge. The two-phase mechanism of shrinking core-shell model (see Figure 3.8) was first brought by Padhi et al.[62-64] They believed that with Li^+ insertion, the interface area will shrink and the reaction will be diffusion-limited after reaching a critical surface area, and vice versa for the de-lithiation process. However, such a shrinking core model cannot describe the mechanism for individual crystallites due to the anisotropic lithium diffusion. Another de-lithiation mechanism is a domino-cascade model at the scale of a particle, which qualitatively explained the asymmetric behavior of the $LiFePO_4$ electrode, and proposed that the Li^+ de-intercalation process proceeds via a transversal elastic wave moving through the entire crystal in the *a*-direction while Li ions migrate along the *b*-direction. This domino-cascade model was further confirmed by high-resolution TEM and EELS spectra technique.[77-79]

Besides the peculiarities of each Li^+ intercalation/deintercalation model, there is a general agreement that Li^+ ions move into the tunnels along the *b*-direction and are extracted /inserted at the interface (phase boundary) where $LiFePO_4$ and $FePO_4$ crystalline structures coexist. It is important to note that the Li^+ insertion/extraction processes appear to depend on the particle size, synthesis method, surface coating, and charging rate.[65] Thus, more controlled studies are needed to understand the intercalation/de-intercalation mechanism under real operation conditions using novel advanced *in situ* characterization tools.

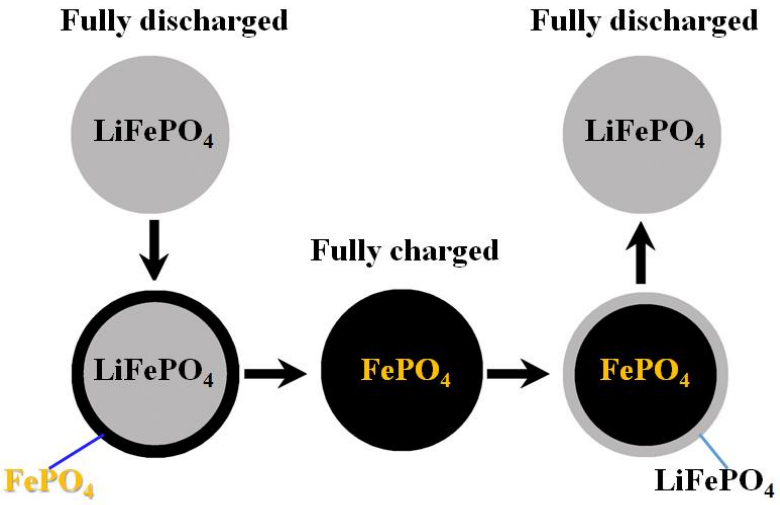

Figure 3.8 Illustration of the shrinking core-shell model with the juxtaposition of the two phases and the movement of the phase boundary.[62]

3.3.2 Various Approaches to Improve the Performance of $LiFePO_4$

a), Particle Size Reduction

Particle size reduction to nanoscale dimension was firstly pointed out by Goodenough's group as one of the effective methods to solve the kinetic problems of $LiFePO_4$.[62] So far particle size reduction has been employed in a number of studies to improve the high-rate capacity and cycling stability of $LiFePO_4$ materials.[80-83] Logically, the high-rate performance is improved by reducing particle size because the transport distance for electrons and Li-ions is thus reduced. Some reports indicated that pristine $LiFePO_4$ with very small particle size (30-50 nm) exhibited the best high-rate performance.[84] Other report stated that the optimum particle size of $LiFePO_4$ cathode for high-power applications seems to be in the range of 200-400 nm.[85]

b), Surface Carbon Coating

Carbon coating is one of the most important techniques to improve the electronic conductivity, the specific capacity, rate capability and cycling life of $LiFePO_4$ materials.[86-89] The main role of carbon coating is to enhance the surface electronic conductivity of $LiFePO_4$ particles so that the active materials can be fully utilized at high current rates. Carbon

coating also reduces the particle size of $LiFePO_4$ by inhibiting particle growth during processing.[90,91] In addition, carbon can act as a reducing agent to prevent the oxidation of Fe^{2+} to Fe^{3+} during high temperature sintering synthesis.[92,93] The beneficial effect of carbon coating has been observed to depend on the structure, uniformity, thickness, loading and precursor of the coating.[86-89,94] The disadvantages of carbon coating include high processing cost and reduced tap density, which may lead to high energy cost and low energy density of the battery cells.[95,96] Therefore, it is important to optimize the carbon coating on $LiFePO_4$ to meet the performance and cost targets for the applications.

Additionally, it reported that graphitic (sp2) carbon coating is much more effective than disordered (sp3) carbon for the Li^+ diffusion throughout the $LiFePO_4$ particle.[92] The ideal carbon coating should preferably be uniform and thin (e.g., < 5 nm) graphitic layers so that the $LiFePO_4$ particles can get electrons from all directions. [87,97-103]

c) Lattice Ion Doping

Doping ions into $LiFePO_4$ can alter the inherent conductivity effectively. On the basis of different sites, it can be classified as doping at Li (M1) sites, Fe sites (M2) and O sites in $LiFePO_4$ lattice unit. The positive effect of doping on the rate capacity and cyclic stability of $LiFePO_4$ has been reported by several groups.[71,104-112] Various ions have been attempted to be doped in $LiFePO_4$, which include anions such as Nb^{5+},[70] Ti^{4+},[104] Mg^{2+},[106] Cr^{3+},[105] Co^{2+},[107] and cation of F^{-1}.[113] The promoting effect was attributed to the improved intrinsic electronic conductivity and the increased Li-ion diffusion coefficient in doped $LiFePO_4$ particles.[109-112] However, the improvement in electronic conductivity was also questioned by others due to the formation of conductive surface films (e.g., carbon, Fe_2P), as confirmed by TEM observation.[114,115] Modeling studies also suggested that doping on either Li or Fe sites is energetically unfavorable and does not result in a large increase of electronic conductivity.[116, 117] Therefore, lattice doping does not appear to be as effective as surface carbon coating for engineering applications, especially when taking into account the impact of doping on the cost of raw materials.

Chapter 4

Anode Materials for Lithium ion battery

In the last decades, anode materials for LIBs have brought significant technological breakthrough. Recent progresses in nanotechnology have led to the application of nano-scale anode for efficient energy storage in high-performance LIBs because of their unique morphologies and structures. As we know, nanomaterials with large surface area and numerous active sites are able to increase the anode capacities and subsequently energy densities of the batteries due to their large active sites for Li intercalation/de-intercalation reactions.

As already stated in Chapter 1 and Chapter 3, the capacity, cyclability and rate capability as the three most important performance factors for LIBs, strongly depended on both the cathode and anode materials. In order to develop LIBs with excellent electrochemical performance, a variety of anode materials have been investigated, and research progress of common anode such as carbonaceous materials, metal alloys, and metal oxides is summarized and reviewed in this Chapter.

4.1 Carbonaceous Materials

Graphite, as the typical carbonaceous material, is the most widely used commercial anode material for LIBs because of its low and flat working potential, long cycle life, and low cost. Basically, lithium ions intercalate into graphite to form Li_6C alloy, delivering a theoretical specific capacity of 372 mAh/g and a potential plateau lower than 0.5 V vs. Li^+/Li.[118] Most carbonaceous materials exhibit both higher specific charges and more negative redox potentials than many metal oxides and chalcogenides. They also show better cycle stability because of a smaller volume change upon lithium intercalation and de-intercalation. As a result, they are still the most popular anode materials for rechargeable

LIBs. Carbonaceous materials suitable for lithium intercalation are commercially available in hundreds of types and qualities.[119,120] However, the low Li-ion transport rate of graphite anodes results in a low power density of a battery since the chemical diffusion coefficient of Li ions is related to the power density of a battery. In recent years, new alternative anode materials such as carbon nanotubes, carbon nanowires and nanofiber,[121,122] mesoporous carbon,[123] and carbon nanocomposites[124] have been extensively studied and developed.

4.2 Metal Alloys

The most Li-enriched intercalation compound of graphite has a stoichiometry of LiC_6,[118] resulting in a less-than-desirable theoretical charge capacity (i.e. 372 mAh/g) and a small practical energy density, and the Li-ion diffusivity of graphite anode is always less than 10^{-6} cm^2 s^{-1}, which results in a low power density of the battery. In order to improve the energy and power densities of LIBs, the use of anode materials with larger capacities and higher Li diffusion rates is required.

Silicon is one of the good candidates. Each silicon atom is known to be able to accommodate 4.4 lithium atoms, leading to the formation of $Li_{4.4}Si$ alloy as Si reacts with Li. This gives rise to an extremely high specific capacity of 4200 mAh/g.[125-127] Because of the extremely high capacity, a lot of study has been conducted on silicon anode material. Unfortunately, bulk Si anode shows rapid capacity fade, accompanying a 400% volume expansion. In order to reduce the volume change for better cycle performance in silicon anodes, two typical silicon anodes, namely nano-based Si anodes and Si-based composite anodes, are most widely studied. Usually, nanostructured Si anodes involve nanoparticles,[128] nanowires,[129] nanotubes.[130] While Si-based composite anodes generally include Si-based alloys,[131] namely Si-M composites (M = metal, oxide).[132]

Sn-based alloys are another promising candidates due to their high specific capacity and stable cycling properties.[133] Sn-based intermetallic alloy Ni_3Sn_4 prepared by electrodeposition has been reported by Hassoun et al,[134] and Ni_3Sn_4 alloy electrode can

retain a stable capacity of 550 mAh/g over 50 charge-discharge cycles at a 0.8C rate. Furthermore, the nanostructured Ni_3Sn_4 electrode delivers a good rate capacity of about 500 mAh/g at 0.8C rate, and no decay of capacity is observed after two hundreds cycles.[135] Sn–M/C composite nanostructured anode materials, such as Sn-Sb nanorods have also been investigated.[136] However, the performance is still not satisfactory to allow the use of the Si- or Sn-based anode in demanding applications.

4.3 Spinel $Li_4Ti_5O_{12}$ as Anode Material

4.3.1 Introduction of Electronic Structure

Twenty years ago, Ohzuku and co-authors[137] reported that the charge/discharge curve for $Li_4Ti_5O_{12}$ (LTO) electrode as anode is characterized by a very flat and extended voltage plateau at around 1.55 V, which is a typical characteristic of phase transition between a Li-rich phase ($Li_7Ti_5O_{12}$, rock-salt LTO) and a Li-poor phase ($Li_4Ti_5O_{12}$, spinel-LTO). Although substantial chemical changes occur during conversion between the two phases, a negligible volume change of 0.2 - 0.3% occurs between two phase changes accompanied by a change of the lattice from 0.8364 nm to 0.8353 nm, and as a result it is called the "zero-strain insertion materials", which indicating that it is an excellent material with exceptional reversibility performance as anode material for LIBs.[137-142] As well investigated and discussed,[137,138,143,144] three Ti^{4+} ions are reduced to Ti^{3+} ions during the two-phase transition from spinel-LTO into rock-salt LTO. The corresponding electrochemical reaction can be briefly described during the lithium insertion and extraction processes as:

$$\text{(Spinel-LTO) } Li_4Ti_5O_{12} + 3Li^+ + 3e^- \leftrightarrow Li_7Ti_5O_{12} \text{ (Rock-salt LTO)} \qquad (4.1)$$

Two types of LTO crystallographic data is summarized in Table 4.1[145]. It is apparent that spinel-LTO and rock-salt LTO has very similar crystallographic parameters, which demonstrate the structural stability during the charge/discharge processing when LTO electrode is applied as anode.

Table 4.1 Crystallographic data for spinel-LTO and rock-salt LTO [145]

Materials (space group)	Atom	Wyckoff Site	Cell parameter			Occupancy
			x	y	z	
Spinel-LTO (Fd3m)	Li1	8a	0.125	0.125	0.125	1.0
	Li2	16d	0.5	0.5	0.5	0.1667
	Ti	16d	0.5	0.5	0.5	0.8333
	O	32e	0.2625(1)	0.2625(1)	0.2625(1)	1.0
Rock-salt LTO (Fd3m)	Li1	8a	0	0	0	1.0
	Li2	16d	0.5	0.5	0.5	0.1667
	Ti	16d	0.5	0.5	0.5	0.8333
	O	32e	0.2576(3)	0.2576(3)	0.2576(3)	1.0

Figure 4.1 shows the structure of spinel $Li_4Ti_5O_{12}$ crystallized in the space group (Fd3m).[137,140] Lithium ions and titanium ions randomly occupy the octahedral (16d) sites, while the tetrahedral (8a) sites are occupied by lithium. As three lithium ions insert into spinel $Li_4Ti_5O_{12}$ and occupy the octahedral (16c) positions, the tetrahedral lithium ions of $Li_4Ti_5O_{12}$ are shifted to the octahedral (16c) sites, and $Li_7Ti_5O_{12}$ crystallizes in the space group with ordered rock-salt structure, as shown in Figure 4.1. In contrast to spinel structure, the octahedral 16d positions are still occupied by lithium ions and titanium ions, whereas the tetrahedral (8a) sites in $Li_7Ti_5O_{12}$ are free. They are described by the cubic space group and have very similar lattice parameters (a = 0.83595 and 0.83538 nm, respectively). [137,140]

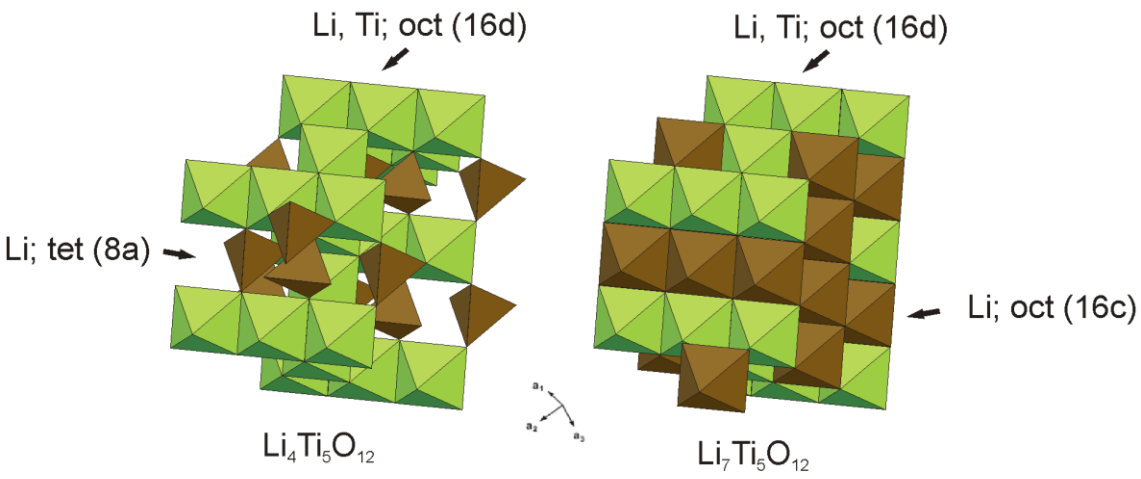

Figure 4.1 Crystal structures of $Li_4Ti_5O_{12}$ and $Li_7Ti_5O_{12}$.[140]

Spinel $Li_4Ti_5O_{12}$ is a good lithium ion conductor (10^{-6} cm^2/s)[146] and very poor electronic conductor (10^{-8} S/cm)[147] because of the existence of available free octahedral (16c) sites in its lattice and the oxidation state of Ti^{4+}. On the other hand, $Li_7Ti_5O_{12}$ is a good electronic conductor (10^{-2} S/cm)[140] and poor lithium ion conductor[148] because Ti^{3+} ions occupy 60% of all the oxidation state of Ti, and the full 16c octahedral sites in the lattice are occupied by Li^+ ions.

The typical core-shell model has described a reasonable two-phase transition process[140,141,147,149,150] as illustrated in Figure 4.2, when the lithium intercalation (discharge) proceeds, the spinel-LTO on the surface of the particle is reduced and transformed to a rock-salt-LTO structure. Then, the shell with rock-salt structure is formed and becomes increasingly thicker with the increasing depth of lithium insertion. Simultaneously, the core with spinel structure shrinks. At the end of discharging process, the entire particle becomes rock-salt LTO. Vice versa, the particle transforms from rock-salt into spinel phase during the charging (lithium extraction) process.

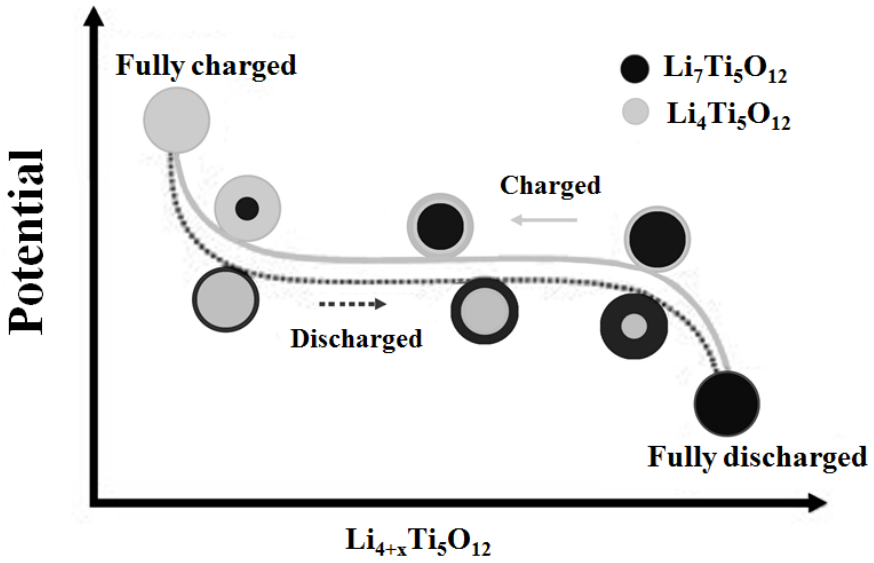

Figure 4.2 Illustration of the charging/discharging process of $Li_4Ti_5O_{12}$ [147]

4.3.2 Approaches to Improve the Electrochemical Performance

a. Doping on $Li_4Ti_5O_{12}$

The performance and electronic conductivity of LTO can be improved by doping of transition metals. Cr and Mo used as dopants can increase electronic conductivity[151-153] and improve the electrochemical properties of the pristine LTO. A small amount (1% doping level) of Ta[154] dopants can increase the electronic conductivity of LTO. V doping is also beneficial to the reversible intercalation and de-intercalation of Li^+ ions, which is responsible for good cycling performance. Li et al[155] have reported that an optimum amount of Zr dopant leads to smaller particle sizes and less particle agglomerations that are favorable for good rate capability in LTO. The effect of Zn doping on the electronic conductivity and electrochemical performance on LTO has also been reported.[156] Although $Li_{4-x}Zn_xTi_5O_{12}$ ($0 < x < 0.5$) compounds show lower capacity, the conductivity is enhanced due to the generation of mixing Ti^{3+}/Ti^{4+}, and hence an improvement in rate capability. Another light metal, Al, used as substitution of Ti, can greatly increase the reversible capacity and cycling stability of LTO.[157,158]

b. Surface Coating

In order to overcome the drawback of poor electrical conductivity of LTO, another typical approach is via surface modification by carbon, metals and oxides, which reduces the electrode polarization and improves its electrochemical performance.

Carbon is frequently added to LTO electrode to utilize the active material more effectively, especially at high charge-discharge rates.[159-161] The effectiveness of carbon addition depends on the amount and type of carbon used. A carbon nano-layer favors the diffusion of lithium ions and redox reaction, hence excellent cycling performance compared with the pristine compound.[162,163] The particle shape and size are also important to enhance electrochemical performance of the coated electrode material. For example, spherical particles[164] with high specific surface area and tap density have been concluded to be effective in improving the electrochemical performance of LTO. Besides providing networks and paths for electrical conduction, nano-tubes[165] can shorten the diffusion path of lithium ions while providing a higher electrode/electrolyte contact surface area, thus overcoming poor Li^+ diffusivity and poor electronic conductivity.

Additionally, metals are often used to improve the poor electrical conductivity of LTO by coating or addition. Ag has been shown to increase the electrical conductivity and decrease the polarization of LTO electrode, and thus improve its high-rate capacity and cycling stability.[166,167] LTO-based composites can be obtained by coating LTO particles with active metal oxides. For example, the $Li_4Ti_5O_{12}$-SnO_2 (5 wt.%) composite delivers a discharge capacity of 189 mAh/g after 42 cycles.[168] SnO_2 additive acts as a bridge between the spinel particles to reduce the inter-particle contact resistance.

Huang and co-workers[169] also reported that the high rate discharge capacity and cycling stability of the pristine LTO was significantly improved by Cu doping. The cycling behavior of the Cu-doped LTO composite was conducted. Table 4.2 compares the discharge capacity and cycling stability of the LTO and Cu-doped-LTO anode materials.[169] The Cu-doped LTO anode showed a remarkably better reversible capacity and cycling stability than the pure and pristine LTO at different charge-discharge rates, which also demonstrated

metal-doping is an effective approach to improve the electrical conductivity and electrochemical performance of LTO. However, such a metal-doping method seemed to show only small-scale production of LTO samples.[169]

Table 4.2 Comparison of discharge capacity and cycling stability of the LTO and Cu-doped-LTO anode materials.[169]

Rate (C)	**Anode materials**	**Discharge capacity cycle (mAh/g)**	
		1^{st}	10^{th}
1	LTO	180.6	164.2
	Cu doped-LTO	209.2	171
2	LTO	162.2	155
	Cu doped-LTO	184.8	166.6
4	LTO	150.7	117.3
	Cu doped-LTO	173.4	153.6
8	LTO	98.9	72.5
	Cu doped-LTO	165.7	144.6
10	LTO	80.3	61.2
	Cu doped-LTO	142.5	141.6

Chapter 5

Synthesis, Structural and Electrochemical Studies of C-$LiFePO_4$ Nanocomposites

5.1 Introduction

As stated previously in Chapter 3, olivine-type $LiFePO_4$ exhibits various unique advantages such as low toxicity, low cost, high thermal and chemical stability, and good electrochemical performance Though it shows a slightly lower voltage than the widely used commercial lithium metal oxides cathode of a layered structure ($LiMO_2$, M = Co, Ni), it has a higher theoretical specific capacity (170 mAh/g) and a flat charge–discharge profile at intermediate voltage (3.45 V vs Li/Li^+).[62,71,170] As well known, olivine structure $LiFePO_4$ crystal is in the P_{nma} space group, and consists of distorted LiO_6, FeO_6, and PO_4 units. The cation arrangement in $LiFePO_4$ differs significantly from that in layered or spinel structures. There is no continuous network of FeO_6 edge-shared octahedra that might contribute to the electronic conductivity. Instead, the strong covalent bonding between the oxygen and P^{5+} to form the $(PO_4)^{3-}$ unit allows for greater stabilization in such structures compared to the layered oxides.[170] Therefore, $LiFePO_4$ has inherently low electronic conductivity (10^{-9} to 10^{-10} S/cm), which results in its poor rate capability due to as well the poor kinetics of the lithium intercalation/de-intercalation process,[71,171] which poses a great challenge for power-demanding applications such as EV and PEV.[172,173]

As introduced briefly in Chapter 3, many nano-engineering approaches have been implemented to overcome its poor conductivity and improve the electrochemical performance of $LiFePO_4$, such as metal cation or anion doping and carbon-coating,[66,86,174-186] off-stoichiometric Fe/P/O compositions,[81] smaller particle sizes that could shorten the diffusion length of Li-ion.[181-184]

It was found that the conductivity can be effectively improved by creating such a conductive carbon coating layer on the $LiFePO_4$ particles at the nano-scale, usually bearing carbon in the amount of less than 2 wt%. The electrons can be spread to the entire surface of

the particles through this carbon layer during charge/discharge and the layer therefore improves the kinetics and reversibility of the lithium intercalation/de-intercalation cycles and gives rise to enhanced rate capability. [66, 86, 187-189]

In this chapter, main study has focused on the structural morphology and electrochemical characterization of carbon-coated $LiFePO_4$ (denote: C-$LiFePO_4$) material prepared by a direct solid phase reaction method using amorphous micro-$FePO_4$ as the iron source. In addition, the synthesis method does not need any additional treatments, such as ball-milling necessary for the traditional solid-state reaction routine.[190]

5.2 Experimental Sections

5.2.1 Starting Materials Precursors

In order to prepare the homogenous carbon-coated $LiFePO_4$ cathode material, selecting the proper synthetic procedure and raw material precursors is very important. Otherwise, undesired impurities such as Fe_2O_3, Fe_2P and Li_3PO_4 can be contained in the final products.[81,174] The starting material precursors were selected as chemical $FeSO_4$ compound, ammonium di-hydrogen phosphate [$NH_4H_2PO_4$], and lithium carbonate [Li_2CO_3] in the appropriate stoichiometry of molar ratio. Acetylene black was the carbon source. All the reagents used in the experiment are of analytical purity.

5.2.2 First-Step Synthesis of Micro-$FePO_4$ Powders

The first step (i.e., pre-calcination) was the solid state synthesis of micro-$FePO_4$ powders, which was typically carried out by heating the mixture of precursors of $FeSO_4$ and $NH_4H_2PO_4$ in the molar ratio of 1:2 of $FeSO_4$ and $NH_4H_2PO_4$ at around 300^oC, which was designed for the decomposition of the precursors and expelling of the gases. After heated and dried for 10-15 h, yellowish-white micro-$FePO_4$ powders were obtained.

5.2.3 Second-Step Synthesis of Carbon-Coated $LiFePO_4$ Nanocomposites

The second step is the final calcination of appropriate stoichiometric amounts of amorphous micro-$FePO_4$ powders and Li_2CO_3, and the conductive carbon source of acetylene black, which occurred at relatively high temperatures (e.g., 800^oC). The calcination temperature has an important effect on the resultant structure and particle size (particle growth).[191] Finally, the powder samples are cooled to room temperature for the resultant products. The resultant carbon-coated $LiFePO_4$ nanocomposites powders with average sizes of 50-100 nm (the aggregates are up to 1 μm), can be obtained by directly adjusting stoichiometric amounts of all the precursors under controlled different temperatures and pressures.

Herein, the C-$LiFePO_4$ nanocomposites powders with different carbon-coating thickness were synthesized using the different stoichiometric amounts of acetylene black as carbon source. Typically, the different coating thickness in these C-$LiFePO_4$ nanocomposite samples are able to be controlled using appropriate stoichiometric amounts of carbon sources (e.g., from 5.5 wt% to 20 wt%) during the second-step calcination process.

5.2.4 Structure Characterizations and Phase Analysis

Firstly, the phase and size of the C-$LiFePO_4$ nanocompsoites particles were analyzed by powder X-ray diffraction (XRD). Secondly, the particles surface morphology was examined by a Hitachi S-4800 field-emission scanning electron microscopy (FE-SEM) equipped with an energy-dispersive X-ray spectroscopy detector. Phase structure and characteristics of the carbon coating were evaluated by TEM imaging, HR-TEM imaging, and selected area electron diffraction (SAED) techniques using a JEOL 3010 microscope at 300 kV. Thirdly, energy filtered TEM (EF-TEM) imaging, STEM -HAADF imaging and elemental mapping, and EELS analysis were carried out by the JEOL 2010F AEM microscope. Fourthly, the surface chemical element measurements were determined by the XPS using a Kratos ULTRA DLD XPS with a mono-chromated Al source that gives an energy resolution better than 0.5 eV.

5.2.5 Electrochemical Testing

Electrochemical properties were measured on electrodes prepared using the mixtures comprised of 80 wt% active material, 10 wt% acetylene black, and 10 wt% polyvinylidene fluoride (PVDF) binder. The $LiFePO_4$ electrode films were fabricated by the doctor blade technique on aluminum foil and dried in a vacuum oven at 100^oC for 10 h. The cells consisted of the electrode, a lithium metal counter electrode and the electrolyte of a 1 M solution of $LiPF_6$ in ethylene carbonate/dimethyl carbonate (EC/DMC, 1:1). The cells were assembled and handled in an Ar-filled glove box and were evaluated using CR 2032 coin-type cells. Galvanostatic charge-discharge cycling tests for the cells were performed within a range of 2.0-4.2 V versus the Lithium counter electrode using in an Arbin BT2000 test system. The cyclic voltammetry (CV) was performed by the scan rate of 0.1 mV/s between 2.0 and 4.5 V, and electrochemical impedance spectroscopy (EIS) was carried out on the coin cells in the fully charge state in the frequency range between 100 kHz and 10 mHz.

5.3 Results and Discussion

5.3.1 Morphology and Structure Characterizations

First of all, five C-$LiFePO_4$ nanocomposite samples were synthesized under appropriate stoichiometric amounts of carbon sources (e.g. from 5.5 wt% to 20 wt%) during the second-step calcination process. The comparison of main crystal phase, carbon-coating thickness, and average size are summarized in Table 5.1.

It is clear that the carbon-coating thickness of ~ 3 nm of C-$LiFePO_4$ nanocomposite was obtained by the stoichiometric amounts of 10 wt% acetylene black as carbon source during the second-step calcination process. Meanwhile, it was found that the carbon sources have the influence on the average size for the final C-$LiFePO_4$ nanocomposite samples, which indicated that the surface carbon adherence suppressed particle growth during the high-temperature calcination process. More amounts of carbon contents will give smaller size of C-$LiFePO_4$ nanocomposite. [94,186]

Table 5.1 The comparison of carbon sources ratio, carbon-coating thickness, main crystal phase and average size of five different C-$LiFePO_4$ nanocomposites

Sample	Carbon sources (wt %) (SEM, EDX)	Carbon thickness (nm) (HR-TEM)	Main crystal Phase (HRTEM)	Average size (nm) (XRD, TEM)
01	5.5 %	No-coating	Olivine	~ 100-300
02	8.5 %	No-coating	Olivine	~ 80-300
03	10 %	~ 3	Olivine	~ 50-100
04	15 %	~ 5	Olivine	~ 50-100
05	20 %	~ 10	Olivine	~ 50-80

Table 5.2 The comparison of C-$LiFePO_4$ nanocomposites prepared under different methods using various precursors and different carbon sources

	Mechanical activation	Soft chemistry	Hydrothermal method	Microwave process	Solid-state reaction
Precursors (wt % ratio)	Li_2CO_3 $FeC_2O_4 \cdot 2H_2O$ $NH_4H_2PO_4$ (1:2:1)	$LiNO_3$ $Fe(NO_3)_3$ $NH_4H_2PO_4$ (1:1:1)	LiOH $FeSO_4$ Li_3PO_4 (3:1:1)	LiOH $FeSO_4$ Li_3PO_4 (3:1:1)	Li_2CO_3 $FeSO_4$ $NH_4H_2PO_4$ (1:2:1)
Carbon source (wt%)	acetylene black (7.8%)	sucrose (11.7%)	glucose (5%)	glucose (10%)	acetylene black (10%)
Crystal Phase	Olivine	Olivine	Olivine	Olivine	Olivine
Size (nm)	100-150	50-500	50-800	80-500	50-100
Coating (nm)	~ 5-14	>10	>10	~ 5-12	~ 3
Capacity (mAh/g)	166	163	154	144	168
References	Ref. 87	Ref. 88	Ref. 99	Ref. 103	This study

Five different C-$LiFePO_4$ nanocomposite samples under five different methods with various precursors and different carbon sources was summarized in Table 5.2. It indicated that the current solid-state reaction has shown the advantageous synthesis of C-$LiFePO_4$ nanocomposite samples with thin carbon-coating thickness and small size range. In particular, the discharge capacity has shown the best value at 0.1C rate, which revealed that the C-$LiFePO_4$ nanocomposites with the thickness of 4.5 nm has exhibited the best electrochemical performance, as compared with the other C-$LiFePO_4$ samples prepared under different methods.

The comprehensive structure analysis and performance evaluations are elaborated in more details as the following.

Firstly, the structure and size distribution of the C-$LiFePO_4$ nanocomposites particles were analyzed by powder XRD. The XRD pattern was shown in Figure 5.1, it is revealed that all diffraction peaks were indexed and matched well with the standard diffraction data for orthorhombic phase $LiFePO_4$ with a phospho-olivine structure (P_{nma}, JCPDS No. 83-2092), which indicates that the particles crystallized in a single phase structure. No crystalline carbon phase can be identified from the XRD pattern, indicating that the existed carbon is amorphous and very low; and its presence does not influence the olivine structure of $LiFePO_4$.

It was noted that very small amount of impurity phase is also present, which can be identified as Li_3PO_4 in the XRD pattern. Such minor impurities could have been induced during the calcinations process in the highly reducing environment. Yet such an impurity phase was reported to have somewhat benefits for fast charging and discharging by providing a guest ion-conductive surface. [81,192]

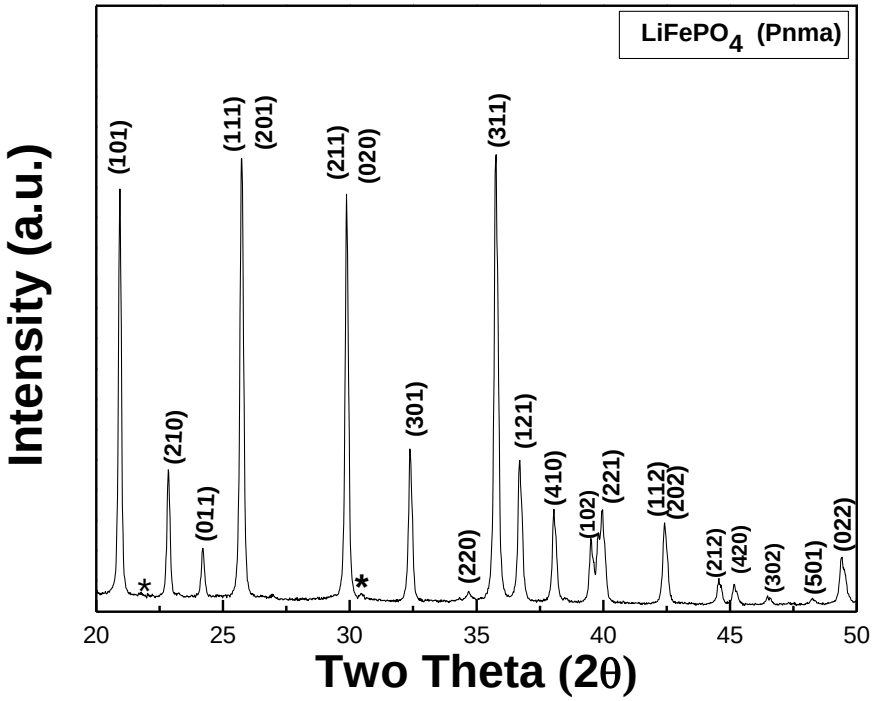

Figure 5.1 Powder XRD pattern indexed with Olivine structure for the C-$LiFePO_4$ nanocomposites. The reflections marked with * refer to the impurity phase, Li_3PO4.

The peaks of (101), (111)/(201), (211)/(020), and (311) in the XRD pattern were selected to calculate average particle sizes using the Scherrer's formula ($D = 0.9\lambda/\beta\cos\theta$, where λ = 0.1542 nm (Cu Kα) and β = full width half maximum at the diffraction angle of θ), the estimated average size was calculated between 50 nm and 85 nm. The least squares fit of the XRD data also yielded lattice parameter values of a=1.033 nm, b=0.603 nm, and c=0.469 nm, which is comparable to the reported unit-cell parameters of olivine $LiFePO_4$ structure (P_{nma}).[62,71,171] The particle size can be controlled by heat treating at different temperatures.

Surface morphologies of the C-$LiFePO_4$ nanocomposites particles were subsequently characterized by FE-SEM imaging. Two representative SEM images are illustrated in Figure 5.2 (a, b). It can be seen that most C-LiFePO4 exhibited non-uniform fine particles

agglomerated assemblies, and the highly irregular aggregates have a size distribution approximately between 500 nm and 1 μm. It is worth mentioning that the C-$LiFePO_4$ exhibited small adherence to the surface, which appeared to be conductive carbon. It was considered that the surface carbon adherence suppressed particle growth during calcination preparation. Those particles are adequately stable; consequently, they cannot be disrupted into fragments easily. In addition, average carbon content of particle aggregates is measured around as 4.2% (mass fraction) from the quantitative energy-dispersive X-ray micro-analysis (SEM/EDX).

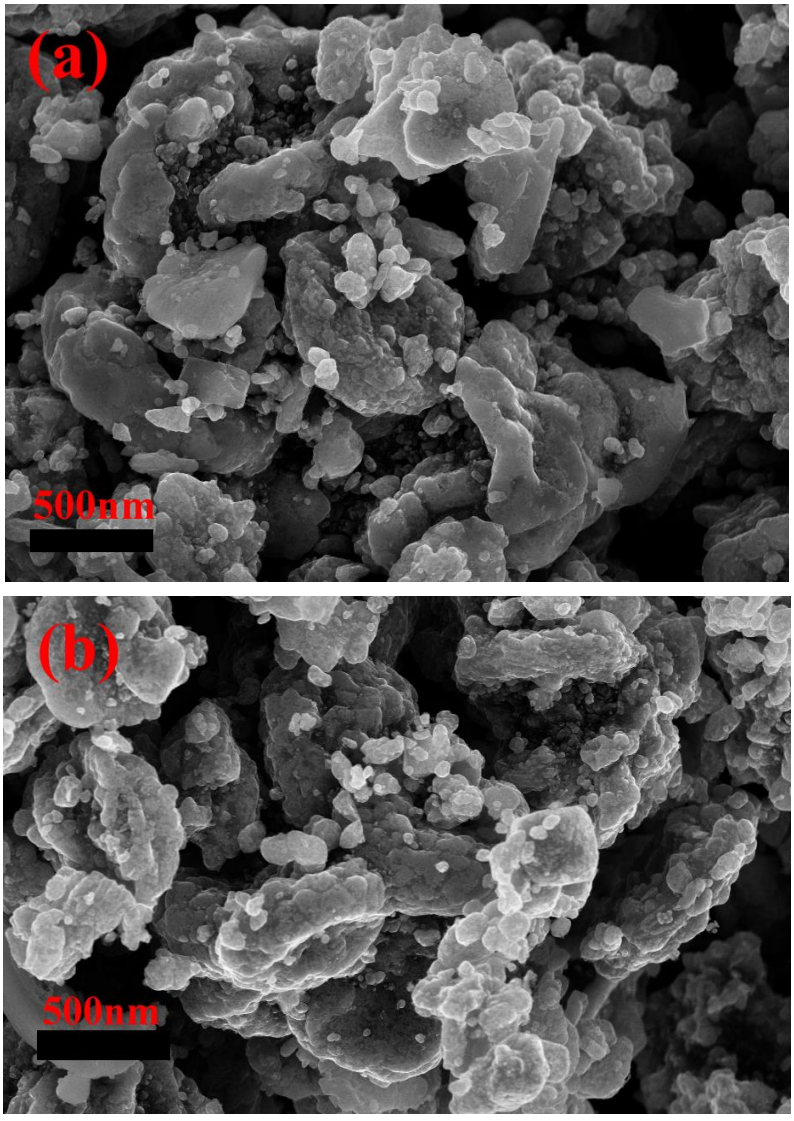

Figure 5.2 (a, b). Two representative FE-SEM images of C-$LiFePO_4$ nanocomposites.

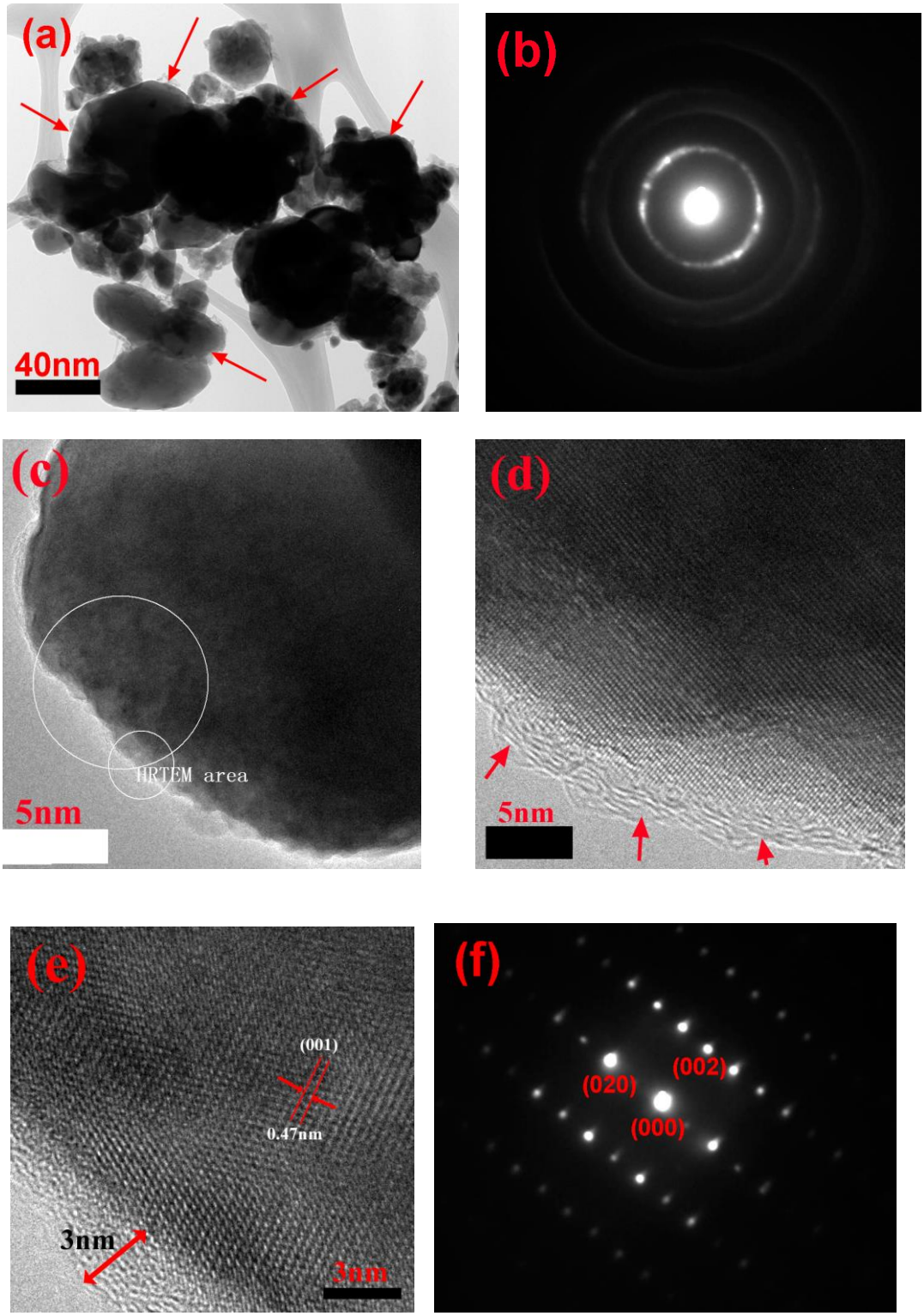

Figure 5.3 Typical BF-TEM images and HR-TEM images and SAED patterns of C-$LiFePO_4$ nanocomposites, carbon-coating layer are clearly observed.

Figure 5.3(a) displays a typical bright-field TEM image (BF-TEM) of the C-$LiFePO_4$ nanocomposites particles. It is apparent that the particles show a rough spherical shape with the sizes of 50-100 nm, which is consistent with the XRD calculation. The appearance of distinct and diffuse SAED rings at Figure 5.3(b) obtained from the particles shown in Figure 5.3(a) revealed the co-existence of an amorphous and the crystal phase in the C-$LiFePO_4$ particles. The HR-TEM images of Figure 5.3(d) and Figure 5.3(e) give more insights into the morphologies of C-$LiFePO_4$ particles. It is clearly visible that an amorphous carbon layer covered the surface of $LiFePO_4$, which is in the interstitial particle/boundary region as marked by red arrows. It has been found that formation of an amorphous carbon in the surface of the particles is attributed to the nature of carbon sources during solid-reaction, and was generated by carbonization of the conductive carbon precursors.[94,186,190,193] Meanwhile, it is observed that the coating seems to be continuous and uniform with a thickness of 3 nm, suggesting that the carbon precursors also played an important role in reducing the $LiFePO_4$ particle size during high-temperature calcinations. The similar results of the amorphous carbon coating that inhibits grain growth were reported.[94,186,193] The well-resolved lattice fringes shown in Figure 5.3(d) and Figure 5.3(e) simultaneously demonstrate the highly single-crystal crystalline of the $LiFePO_4$ structures. The typical d-spacing of 0.47 nm as marked in Figure 5.3(e) is consistent with the (001) plane of the orthorhombic structure of $LiFePO_4$. The corresponding SEAD pattern in Fig. 5.3(f) taken from the individual particle of HR-TEM image of Figure 5.3(e) also demonstrates the single-crystal nature of the $LiFePO_4$. The indexing of electron diffraction spots correspond to the (020) and (002) planes of $LiFePO_4$ crystals, which further reveals the single-crystalline olivine-phase has been formed. Similarly, average carbon mass content was measured as 4.15% by EDX chemical probing analysis along with the HR-TEM images, which matched well with the above SEM/EDX data.

Energy filtered TEM (EF-TEM) imaging was performed to further investigate carbon coating framework and local surface state of the C-$LiFePO_4$ particles. The BF-TEM image of representative particle is selected and shown in Figure 5.4(a). The elemental

compositional imaging analysis was carried out throughout the particle; the resulting elemental distribution mapping was shown in Figure 5.4(b). Apparently, this is a typical core-shell particle structure, demonstrating the well-defined evidence of a thinner carbon coating layer completely covering the exposed $LiFePO_4$ nanocomposites particle surfaces as observed from the unique carbon (C) and ion (Fe) elemental mappings distributed with different colors in the Figure 5.4(b), which is in well accordance with the above HR-TEM images observations and SAED analysis.

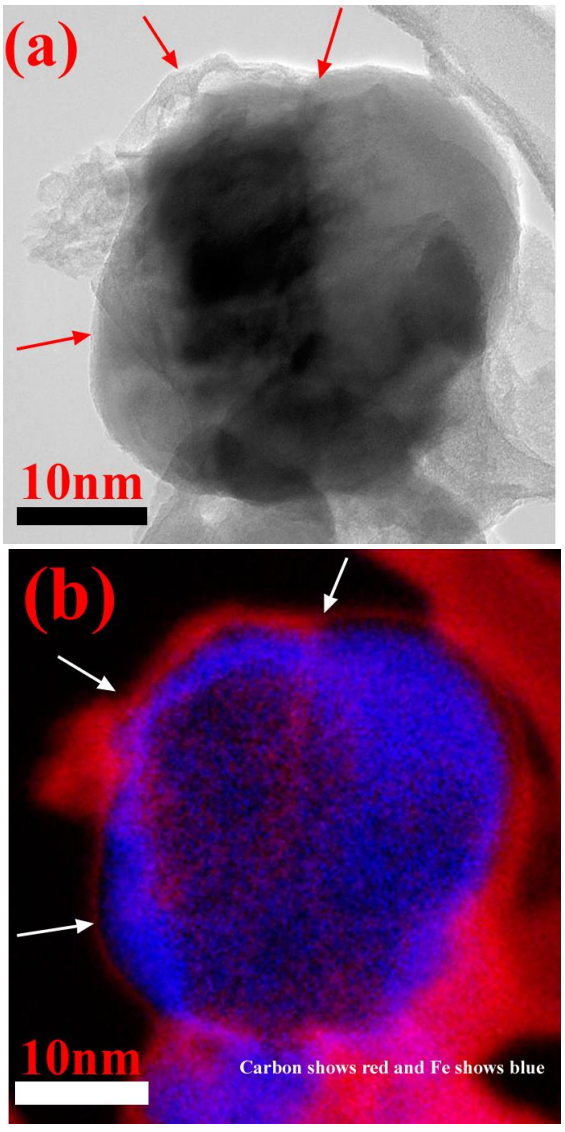

Figure 5.4 (a) Typical BF-TEM image of individual C-$LiFePO_4$ nanocomposites particle. (b) The energy-filtered TEM (EF-TEM) image and elemental map.

It can be concluded that, structural analyses of HR-TEM imaging and EF-TEM imaging convincingly reveal that the formation of a stable olivine C-$LiFePO_4$ nano-composites particle, each particle has a single-crystal $LiFePO_4$ core and a thinner carbon coating layer. [94,193-196]

5.3.2 STEM-HAADF Imaging and EELS Analysis

Scanning transmission electron microscopy high-angle annular dark field (STEM-HAADF) imaging and EELS spectra was employed to further visualize the C-$LiFePO_4$ nanocomposites particles, since the combinational technique is able to probe the chemical and valence states along the particles at the nano-scale.[197-199] It is well known that elemental valence band excitations and phase compositions of the transition-metal can be feasibly detected and determined at nanometer resolution from the analysis of energy loss near edge structures (ELNES) in a typical EELS spectra.[197-199] Particularly, the EELS edge spectra is proven to be a very powerful tool for studying nano-structured $LiFePO_4$ because the valence state of the transition Fe metal can be analyzed by measuring the relative intensity of the Fe L_3 and Fe L_2 lines.[197-200]

A typical STEM-HAADF image of individual C-$LiFePO_4$ nanocomposites particle was shown in Figure 5.5(a), and the corresponding EELS spectra was recorded and shown in Figure 5.5(b) and Figure 5.5(c), respectively. First of all, the characteristics of the coating framework layer of C-$LiFePO_4$ particle surface were clearly identified in the EELS spectrum shown in Figure 5.5(b). Obviously, the coating layer was sp2-bonded amorphous carbon by a C–K edge with maximum peak at 285.0 eV due to the C 1s$\rightarrow \pi^*$ transition for disordered carbon-carbon sp2-hybridized bonds. Meanwhile, Figure 5.5(b) shows Fe $L_{2,3}$ white lines recorded at high-loss energy range. The ELNES spectrum of the Fe-$L_{2,3}$ edge analyses in Figure 5.5(b) was ascribed to the characteristics of Fe^{2+} in olivine $LiFePO_4$ structure. On the other hand, the Fe^{2+} valence state appeared in the hybridization of P 3p states with the Fe 3d states due to the FeO_6 octahedral site in olivine-$LiFePO_4$ structure, which is demonstrated by

an L_3 edge peak maximum at 710 eV. It is also evident in Figure 5.5(b) that O is determined by a O–K edge with a maximum peak at 532 eV, and that P is present in Figure 5.5(c) by a P–$L_{2,3}$ edge with a double peak and a first maximum at 140 eV. Consequently, the O-K edge and P–$L_{2,3}$ edge is inferred from the oxo-anions $(PO4)^{3-}$ unit, which is ascribed from the phospho-olivine structure of lithium transition-metal phosphates in the orthorhombic P_{nma} space group system.[62,197,199] The Li–K near edge structure is also clearly visible and identified in Figure 5.5(c). Indeed, the ELNES of Li with a K-edge at a maximum peak of 58 eV in the low energy core loss spectrum can be used as a fingerprint for phase identification of LiO_6 octahedral sites located in olivine-structure $LiFePO_4$. [170,172]

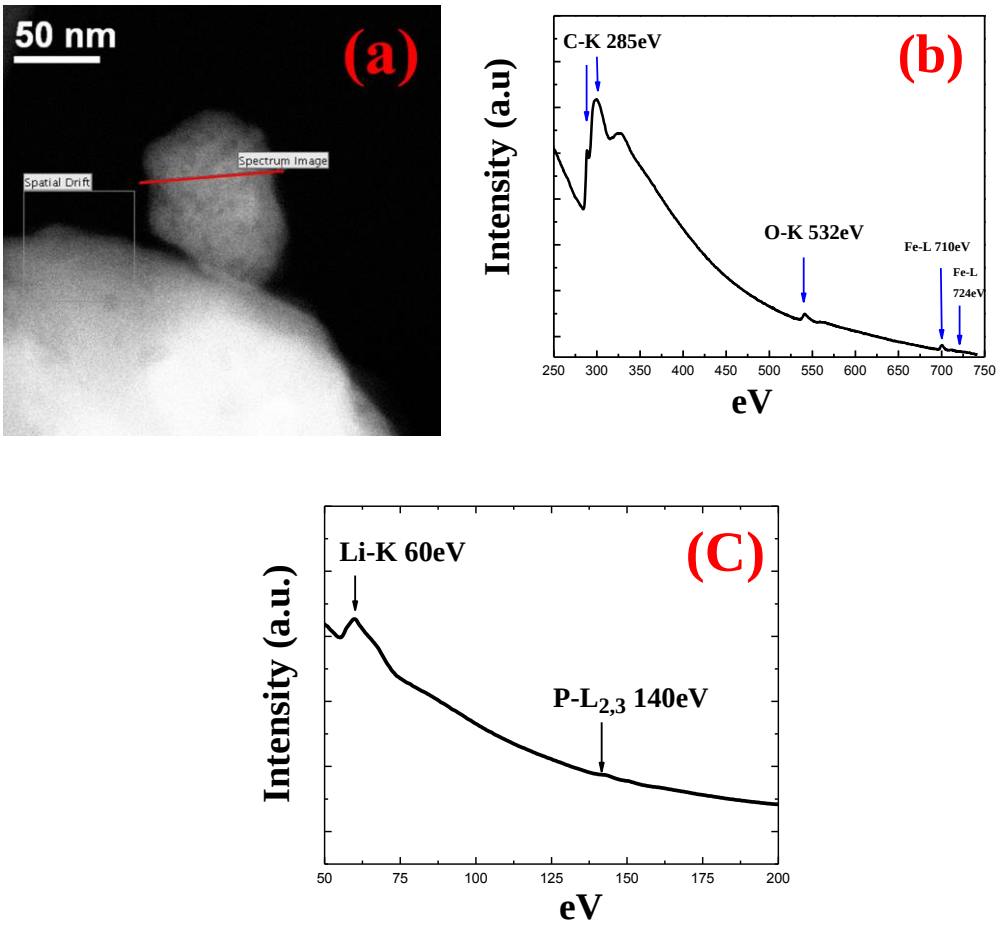

Figure 5.5 Typical STEM-HAADF image (a) and the EELS Spectra (b,c).

5.3.3 XPS Analysis

As a powerful surface analysis technique, XPS technique is well-suited for the evaluation of valence and electronic states of metal/non-metal ions, and extensively used in the characterizations of the olivine $LiFePO_4$ cathode materials.[201-206]

The XPS spectrum survey profile and core-scan XPS spectra of Li 1s, Fe 2p, P 2p, O 1s, and C 1s profiles are shown in Figure 5.6 (a) and Figure 5.6 (b, c, d, e, f), respectively. It is clear that the survey profile in Figure 5.6(a) shows that the main binding energy (BEs) of Li 1s, Fe 2p, P 2p and O 1s, C 1s peaks are 55 eV, 710 eV, 133 eV, 531 eV, and 285 eV, respectively. Here the Ti and N peaks were from the sample holder.

It is seen from Figure 5.6 (b) that the Fe 2p spectrum split into $2p_{1/2}$ and $2p_{3/2}$ due to the spin-orbit coupling. Each part consists of a main peak and a corresponding satellite peak at BEs of 710.9 and 724.4 eV for Fe $2p_{3/2}$ and Fe $2p_{1/2}$, respectively. In fact, the appearance of satellite peaks or shoulder peaks is a typical characteristic feature of transition metal ions with partially filled d-orbits.[201-203] Herein, the two distinct BEs peaks are attributed to the characteristic of the valence of the Fe^{2+} state in the $LiFePO_4$ olivine-structure as reported previously. [201-207]

Meanwhile, the P 2p spectrum in Figure 5.6 (c) can be de-convoluted into two components of $2p_{3/2}$ and $2p_{1/2}$ at BEs of 134.1 eV and 133.6 eV due to spin–orbit coupling. The presence of only one doublet reveals the P chemical state should be the PO_4^{3-} tetrahedral group characteristic in the lithium transition-metal phosphates, which indicates the absence of iron phosphides, thereby excluding the formation of impurity phases such as Fe_2P or Fe_2O_3 that would appear at a BE value of 129.5 eV. The O 1s spectrum in Figure 5.6 (d) has the main binding energy of 530 eV, which represents the oxide ions of PO_4^{3-} group existed in $LiFePO_4$. The O 1s spectrum and P 2p spectrum exhibited the BE peaks at 530 eV and 133.6 eV are eventually originated from the phosphate units structure.[201-207]

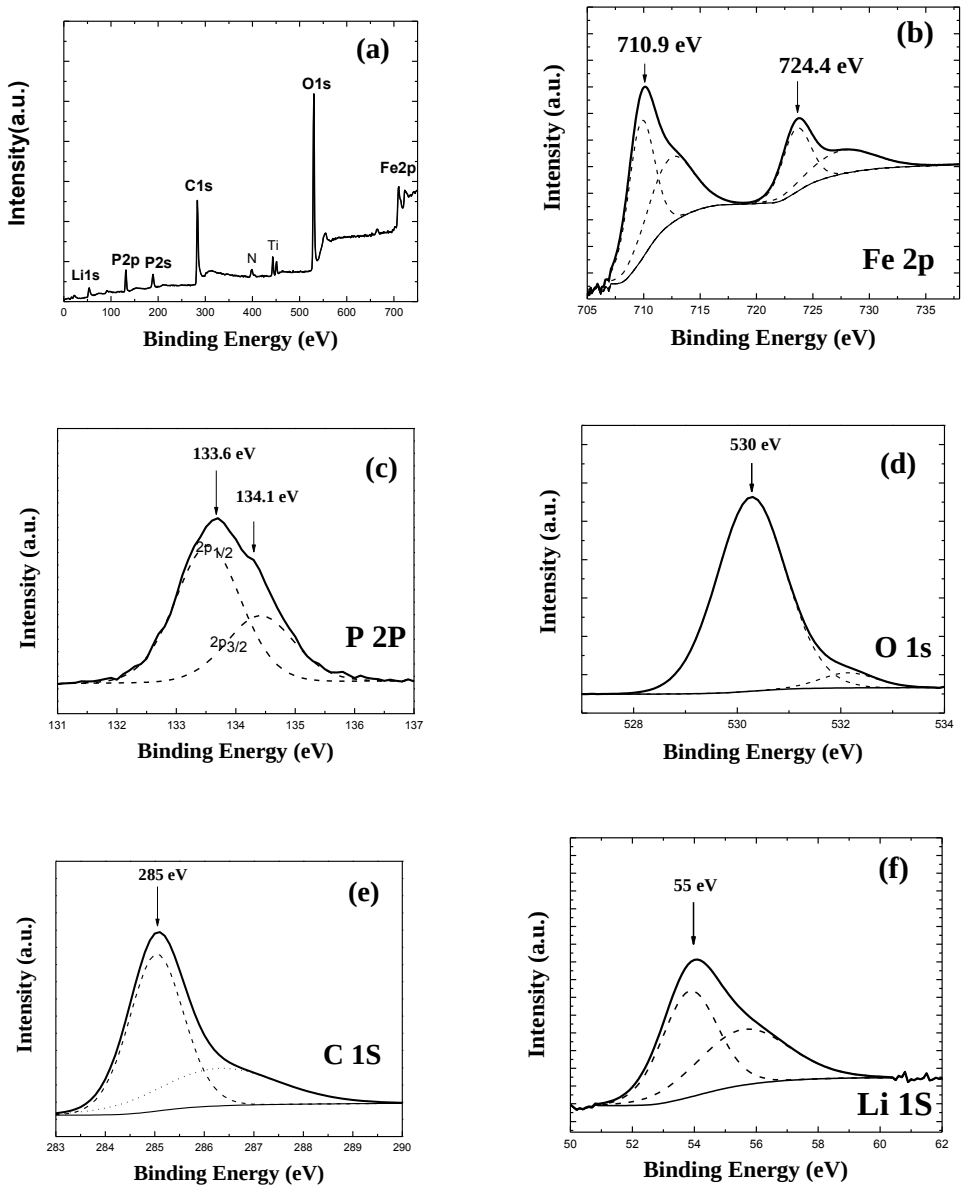

Figure 5.6 (a) is XPS spectrum survey profile of the C-$LiFePO_4$ nanocomposites. (b-f) is the core-scan XPS spectra of Fe2p, P2p, O1s, C1s, and Li1s profiles, respectively.

The main BE peak of 285 eV of C1s spectrum in Fig. 5.6(e) is assigned to amorphous (284.7 eV) carbon with sp^2 C−C bonds, and such a BE value of C1s is consistent with the one reported from the literature.[205-207] The smaller difference for the reported binding energy (284.7 eV) is probably due to oxygen-containing surface functional groups formed at the surface because of air exposure. Thus, the presence of an amorphous sp2-bonded carbon

coating on the sample surface was revealed. Furthermore, it was shown that the centered BE peak of 55 eV in the Li 1s spectrum of Figure 5.6 (f) is consistent with the BE value of Li^+ ions in the reported $LiFePO_4$-Olivine cathode.[201-203]

Therefore, XPS analysis convincingly confirms the existence of olivine phase purity and amorphous carbon phase in the C-$LiFePO_4$, which is in well agreement with the above XRD data, HR-TEM images, EF-TEM images, and EELS analysis. In a word, the synthesis of stable amorphous carbon coated $LiFePO_4$ nanocomposite particles is clearly demonstrated.

5.3.4 Electrochemical Performance

The cyclic voltammogram (CV) at 0.1 mV/s using a charged coin cell within a potential window of 2.0-4.5 V (vs. Li/Li^+) is shown in Figure 5.7 (a). It is clear that C-$LiFePO_4$ nanocomposites showed one distinct anodic peak (charge) and cathodic peak (discharge). The well-defined sharp redox peaks in the range of 3.3-3.6 V is attributed to the Fe^{2+}/Fe^{3+} redox couple reaction. The anodic peak at 3.52 V corresponded to the oxidation of Fe^{2+} to Fe^{3+}, and the reduction of Fe^{3+} to Fe^{2+} appeared at 3.3 V, which also corresponds to Li ions extraction and insertion in $LiFePO_4$ crystal structure. These are consistent with a two-phase redox reaction at about 3.5 V vs. Li/Li^+. [62,71] This also implies that a two-phase Fe^{3+}/Fe^{2+} redox reaction proceeds via a first-order transition between $FePO_4$ and $LiFePO_4$.[62,71] The CV profiles almost overlap after three cycles, revealing very good reversible kinetic reaction. In addition, sharp redox peaks and smaller potential interval peaks shown in the Figure 5.7(a) demonstrated that lithium ions and electrons were quite active during kinetic redox reactions, which could be attributed to the smaller particles that reduced the diffusion length of the Li^+ ions, and the amorphous carbon-coating layer that facilitated the electrons transfer in C-$LiFePO_4$. It is also worth mentioning that the intensity and shape of the peak current in the CV profiles can be affected by carbon coating.[157-169] The C-$LiFePO_4$ electrode showed a higher peak current than the no-coated $LiFePO_4$,

demonstrating that both Li^+ ions and electrons considerably contributed to kinetic redox reactions as a result of the carbon coating on $LiFePO_4$.

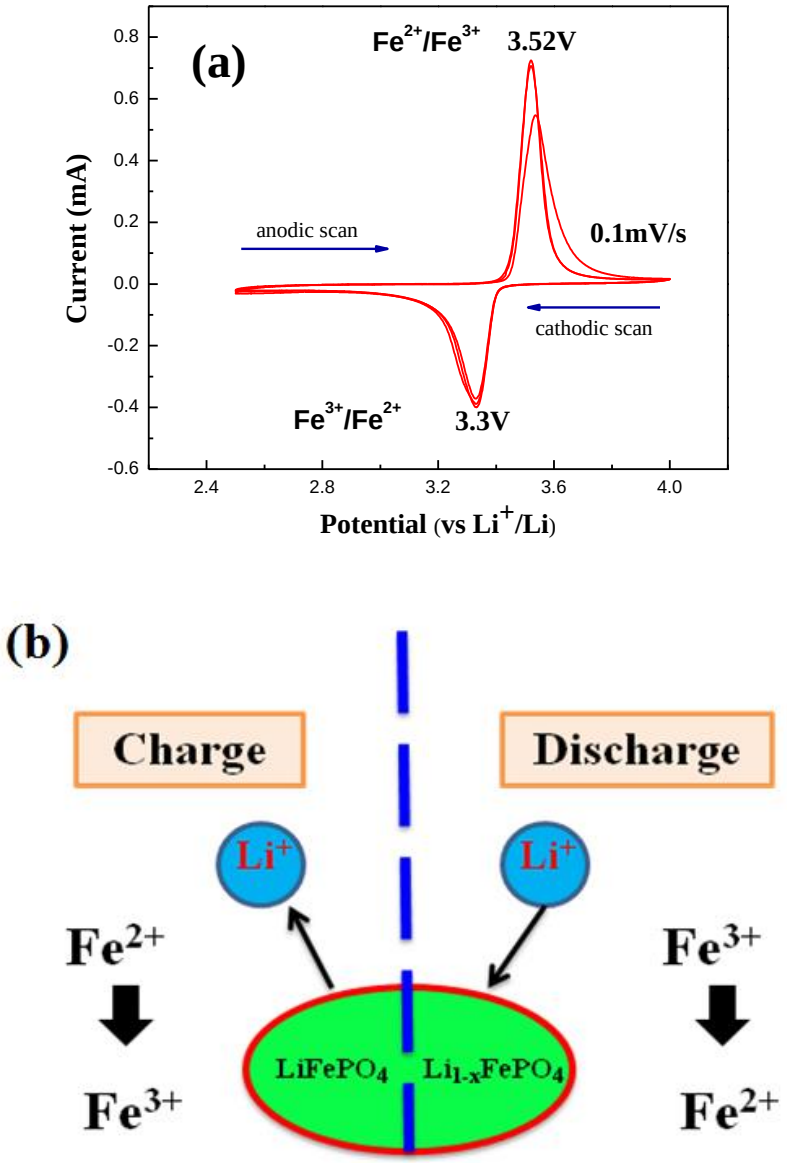

Figure 5.7 (a). The cyclic voltammetry (CV) profile of C-$LiFePO_4$ nanocomposites at the scan rate of 0.1 mV/s. **(b).** Schematic diagram of Li ion intercalation/de-intercalation during charge-discharge.

Figure 5.7 (b) shows the brief schematic diagram of Li^+ ions intercalation/de-intercalation processing during charge-discharge of the $LiFePO_4$. One of the fascinating characteristics of $LiFePO_4$ is its ability to be used at very high cycling rates, although it does exhibit lower electronic conductivities. So far, based on many research efforts focused on neutron diffraction data, electron microscopy/electron energy loss spectroscopy observations, and theoretical simulations, several reasonable models have been proposed to establish the relation between the structure and both ionic and electronic transport properties of $LiFePO_4$ cathode materials.[77,78,208-210]

An mentioned in Chapter 3, the model proposed the reversible charge/discharge (de-lithiation/lithiation) of olivine $LiFePO_4$ is a two-phase reaction mechanism of shrinking core-shell model by $FePO_4 + xLi^+ + xe^- = xLiFePO_4 + (1-x)FePO_4$.[78] Such a two-phase model was proposed to explain the behavior of $LiFePO_4$ electrodes with an isotropic core-shell mechanism.[76,208] However this model didn't consider the microscopic process involved during the reaction.

As stated previously at Chapter 3, the proposed domino-cascade model at the scale of a particle[77 209] well explained how Li^+ ions and electrons can move as solid-solution reactions inside the olivine $LiFePO_4$ particles.

To understand the whole lithium de-intercalation /intercalation mechanism, the ionic and the electronic conductivities need to be considered simultaneously, as both processes are coupled at the microscopic scale; the effect of strong local distortions must also be account for. As reported,[209] the major drawback of the shrinking core-shell models to describe the evolution of the reaction mechanisms observed experimentally is the necessity for the majority of particles to be at similar degrees of lithiation. However most $LiFePO_4$ particles have a distribution of sizes, so it is unlikely that the majority of particles meet this requirement.

In fact, $LiFePO_4$ functions as a cathode where de-lithiation (charge) occurs via either a solid-solution or a two-phase mechanism, which is influenced by sample preparation and electrochemical conditions. The reaction mechanism is found to be also affected by particle

size, which determines whether two-phase reactions can be stabilized within a particle. It is interesting to note that the core-shell models and domino-cascade models have been verified to describe different experimental observations, which indicated the domino-cascade model explains the mechanism at the particle scale, but the core-shell models are valid at an agglomerate (meso) scale.[209]

The direct experimental evidence for competitive solid-solution (domino-cascade) and two-phase reactions occurring within a $LiFePO_4$ cathode under non-equilibrium conditions was also revealed,[210] as theoretically predicted.[211] The simultaneous occurrence of solid-solution and two-phase reactions can be confirmed by in situ neutron powder diffraction after deep discharge at non-equilibrium conditions. As mentioned earlier,[62,66,71] the $LiFePO_4$ lattice is an assembly of FeO_6 octahedra sharing corners and forming Fe-O atomic *ac* planes. The tetrahedral PO_4 units link these planes together, which forms the skeleton of the lattice. The presence of one common edge between each PO_4 tetrahedron and each FeO_6 octahedron in the $LiFePO_4$ lattice is very particular. The mobile Li^+ form one dimensional chains in the structure that run parallel to planes of corner-shared FeO_6 octahedra, and along the [010] direction in the orthorhombic P_{nma} lattice. This generates preferential rapid one-dimensional Li^+ ion conductivity along that direction. But the strong covalency of the P-O bond is found in phosphates. Therefore, in the olivine structure, this edge-sharing induces strong distortions at the local scale that spread in a cooperative way through all of the crystallite.

In particular, during lithium de-intercalation, Fe^{2+} ions are oxidized to Fe^{3+} with strong changes in the Fe-O bond lengths and O-O distances in FeO_6 octahedra, leading to a cooperative structure distortion. Overall, these structural distortions have a significant impact on the electronic conductivity. The very high concentration of Li^+ vacancies and Fe^{2+}/Fe^{3+} polarons localized in this interfacial zone enables a very fast reaction. This interfacial zone is unstable and can move very rapidly inside the crystallite, like a wave going through the particle in the *a* direction on de-intercalation /intercalation processing.[77] Recently, the first-principle calculation result demonstrated the critical effects of the local crystal structure changes on the electronic structure and the kinetic properties of olivine

cathodes since both Li^+ ion mobility and electron conductivity are significantly enhanced by the local structure change.[212]

In order to evaluate the electrochemical cycle capability performance for the C-$LiFePO_4$ nanocomposite, galvanostatic discharge-charge cycling testing, at various current densities of C/10, C/5, C/2, 1C, was performed at different cycles and shown in Figure 5.8. The cell exhibited a typical plateau at 3.42 V (versus Li^+/Li) associated with the Fe^{3+} to Fe^{2+} redox process for the $LiFePO_4$ electrodes. It is clear from Figure 5.8 that the C-$LiFePO_4$ particles delivered almost 99% of their theoretical discharge capacity of 168 mAh/g at 0.1 C rates. The exceptionally high capacity is due to full usage of the active material at 0.1 C rate.

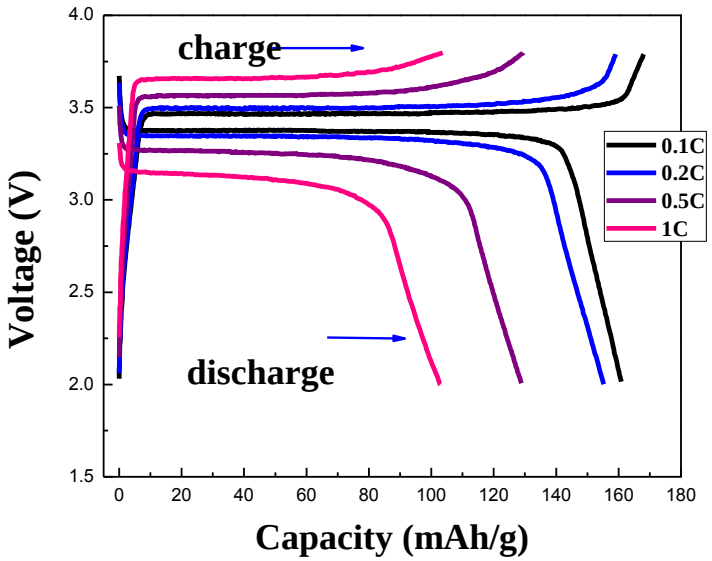

Figure 5.8 The discharge and charge profiles of C-$LiFePO_4$ nanocomposites at different C-rates.

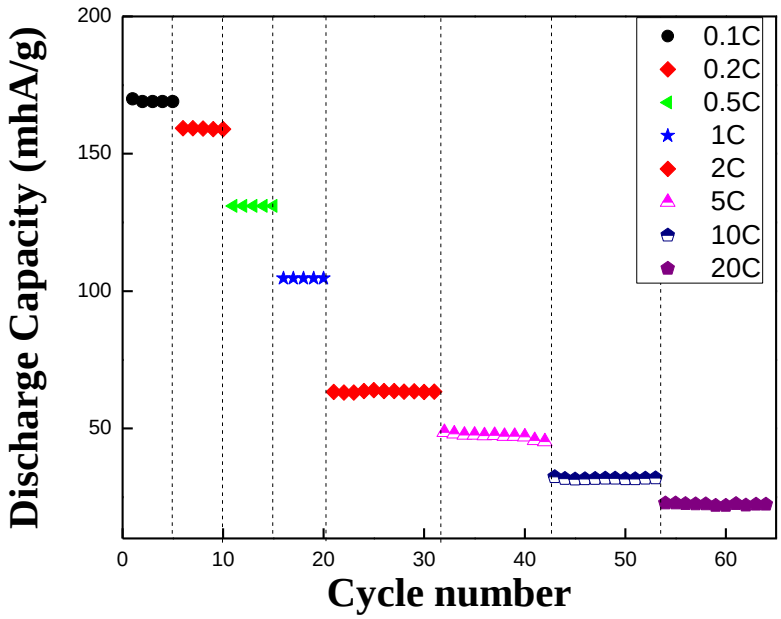

Figure 5.9 The rate capabilities for C-$LiFePO_4$ nanocomposites at different C-rates (from 0.1C to 20C)

Also the good discharge capacity retention of approximately 165 mAh/g at 0.2C, 140 mAh/g at 0.5C and 115 mAh/g at 1C were achieved after charging/discharging cycle, respectively. Very good reversible charge–discharge symmetry from 0.1C to 2C was observed, which also demonstrates less polarization during the galvanostatic discharge-charge cycling. That is attributed to the nanometer particles and carbon-coating network that enables both Li^+ ions and electrons to migrate and reach each of the nanocomposite particles, hence facilitating the more potential usage of the active materials. This is in good agreement with the results in Figure 5.7 (a).

Figure 5.9 is the rate capabilities performance for C-$LiFePO_4$ nanocomposite electrode cycled at different current rates from 0.1C to 20C**.** No obvious decline was observed in the discharge capacity that remained stable during every cycling, and the good rate performance is revealed, and a better lithium intercalation/de-intercalation property is demonstrated.

However, it should be noted that the discharge capacity becomes low at a high current density (e.g., 5C, 10C, 20C), which can be ascribed to the slowing diffusion of Li^+ ions inside particles at high current rates.

This indicated that the C-$LiFePO_4$ nanocomposites sample demonstrated the superior discharge capacity and good rate capability, and cycling performance with initial discharge capacities 168 mAh/g at C/10. As we already discussed, these improved properties were strongly correlated to the improved electronic conductivity of the $LiFePO_4$ coated with amorphous carbon and smaller charge transfer resistance as shown in the following electrochemical impedance spectroscopy data. As mentioned earlier, the active materials with better electronic conductivity should have better discharge capacity and cycling capabilities. It is believed that the crucial role played by the surface carbon-coating on the C-$LiFePO_4$ nanocomposites is responsible for the better electrochemical high power performance due to the effective increase of both electronic and ionic transport.

Much effort has been made to improve the power performance of $LiFePO_4$ by carbon coating to increase the conductivity of $LiFePO_4$ cathode.[13,44,213-218] Surface carbon coating has been well recognized as an alternative to enhance electronic conductivity in the design of a cell battery electrode. The significant role of the carbon layer is believed to be creating a better electric contact between the intra-particles inside the Li-ion cell. Once an electron has arrived at the surface of the particle it can migrate to the collector of the electrode rapidly through the connected network of conductive carbon. Moreover, the non-coated $LiFePO_4$ cathode particles have a disordered surface layer,[213] which results in an increased electric resistance of battery cells. The full carbon coating is also expected to cure the structural disorder on each particle surface, thus reducing the electric resistance in the surface of particles. Another significant influence, reported from several research groups [13,44,215-217] is that the carbon layer permits the pass of Li^+ while preventing the pass of solvent molecules of the electrolyte during the Li-intercalation process; the carbon layer plays the role of a buffer layer on Li-intercalation, which may improve the adsorption of Li^+ and mobility of Li^+ on the outer surface of $LiFePO_4$ used in the battery cell.[66,215]

It is still unclear whether the carbon coating improves interfacial charge transfer in the $LiFePO_4$ cathode, which may be another specific reason for the high power performance. It should be further investigated with more advanced surface analysis technology.[66,215] Meanwhile, the synergetic effects of carbon coating of the creation of the Fe^{2+}/Fe^{3+} polarons and improved interfacial charge transfer also need to be further confirmed.

Electrochemical impedance spectroscopy (EIS) was measured on the CR-2032 coin cells in the fully charge state. Figure.5.10 shows the typical Nyquist plots for the charged cell measured at 1C rate. The plot has an intercept at high frequency, followed by a semicircular plot in the medium-to-high frequency region and a sloping line in the low frequency region.

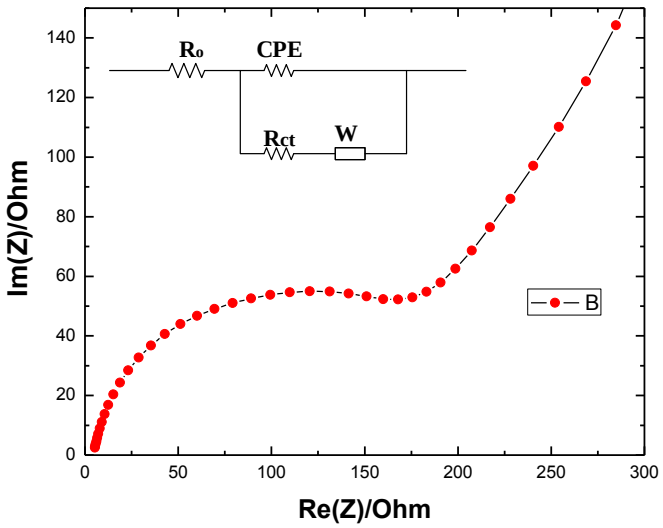

Figure 5.10 Electrochemical impedance spectroscopy (EIS) on the $LiFePO_4$ coin cells in the fully charge state in the frequency range between 100 kHz and 10 mHz. The equivalent circuit is shown in the inset

As known, the intercept at the *Im* (Z) axis in the high frequency region was attributed to the ohmic resistance (R_o), representing the resistance of the electrolyte. The semicircular plot in the medium frequency range is associated with the charge transfer resistance (R_{ct}) of the electrochemical reaction, and the sloping line in the low frequency region represents the

diffusion of lithium ions into the bulk of the cathode material, namely the Warburg impedance.[219,220] This is because the Warburg impedance at low frequency is directly related to the lithium-ion diffusion process in an electrode material.

The R_{ct} value for the C-$LiFePO_4$ samples is calculated to be around 110 Ω. It is clear that the R_{ct} values are lower than several literature values.[221-224] Generally, the value of R_{ct} is small enough to force Li^+ ions and electrons react immediately, accelerating the transport of the polarons of Li^+ ions and electrons at the electrode, which is beneficial to the kinetic reactions during charge-discharge process. As a result, the electrochemical performance is improved. This also demonstrates that the EIS is completely consistent with the results from the CV and the cycling testing.

5.4 Fabrication and Evaluation of the $LiFePO_4$ Battery Cell

5.4.1 Fabrication of the 18650-$LiFePO_4$ Prototype Battery Cell

The present synthetic technique is promising for mass production of the C-$LiFePO_4$ materials, since it is able to scale up. The 18650 $LiFePO_4$ prototype battery cells (i.e., 18 mm width x 65 mm length) have been manufactured by an industrial partner using those C-$LiFePO_4$ cathode materials, as shown in Figure 5.11.

Basic electrochemical characteristics of such an 18650 $LiFePO_4$ prototype battery is summarized in Table 5.3. Electrolyte was used with organic electrolyte of 1M $LiPF_6$ in EC and DMC (1:1), and commercial graphite was used as anode in this prototype battery.

Figure 5.11 The 18650-$LiFePO_4$ prototype battery cells

Table 5.3 The electrochemical characteristics of 18650-$LiFePO_4$ prototype battery cell

$LiFePO_4 \Leftrightarrow FePO_4 + Li^+ + e^-$		$Li^+ + e^- + C \Leftrightarrow LiC_6$
Positive Electrode: (Cathode) $LiFePO_4$ on Al terminal	Electrolyte: 1 M $LiPF_6$ in ethylene carbonate (EC)/dimethyl carbonate (DMC)	Negative Electrode: (Anode) Graphite on Cu terminal
Loading as: 28.5 mg/cm^3		Loading as: 11.5 mg/cm^3
Left to Right = Charging		Right to left = Discharging

5.4.2 Industrial Evaluation of the 18650-$LiFePO_4$ Prototype Battery Cell

The rate capability of the $LiFePO_4$ prototype battery cell is demonstrated in Figure 5.12. It is very clear that the discharge capacity slowly decays along with the increase of the current rate. When the discharge current is as high as 3C, this prototype battery cell still reaches a discharge capacity of ~3300 mAh, approximately 80% of its capacity at 0.2C, which indicated such a $LiFePO_4$ battery offers very high-rate performance.

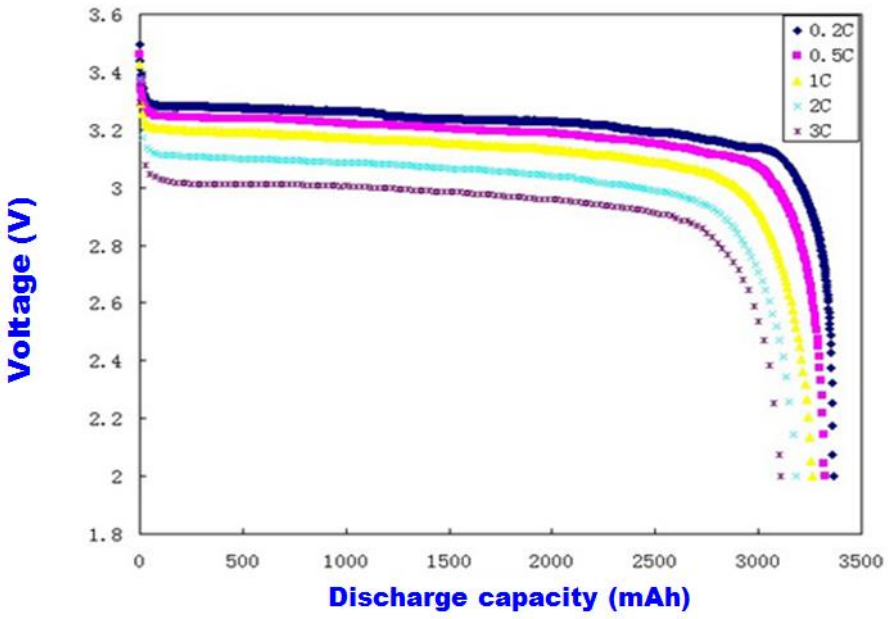

Figure 5.12 The rate capability curve of the 18650-$LiFePO_4$ prototype battery cell at different rates

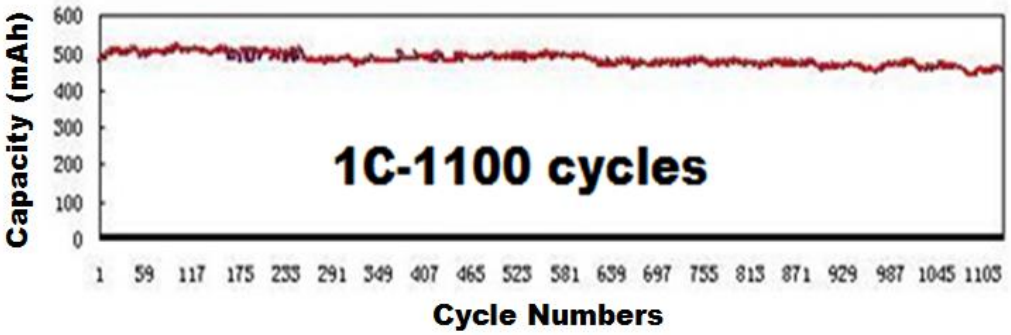

Figure 5.13 Cycle life performance of the 18650-$LiFePO_4$ prototype battery cell

The electrochemical investigation was carried out using an 18650 cell with the standard organic electrolyte of 1M $LiPF_6$ in EC and DMC (1:1). The battery cell demonstrated a remarkable cycle life performance as shown in Figure 5.13. An extremely stable discharge capacity was obtained at a 1C discharge rate. The discharge capacity remained almost constant at 520 mAh for approximately 1100 cycles at 100% deep of discharge (DOD).

Both cycling lifetime and remaining discharge capacity is increased by 15-20% as compared with commercial $LiFePO_4$ batteries using graphite anode. In brief, our C-$LiFePO_4$ cathode powder samples have of the potential for long-life lithium-ion batteries with improved cycling performance and high discharge capacity.

On the other hand, it has demonstrated that uniform carbon coating on the surface of $LiFePO_4$ cathode enhanced the efficiency of the battery charge and discharge with increasing electronic conductivity and Li-ion diffusion.

5.5 Chapter Conclusions

Amorphous carbon-coated C-$LiFePO_4$ nanocomposite have been synthesized by an economic solid-state reaction process. All the structural analyses of the C-$LiFePO_4$ nanocomposites at nanoscale such as TEM, HR-TEM, EF-TEM and STEM-HAADF imaging as well as both EELS and XPS spectra provide a comprehensive view of the

correlation of structure-performance of, and also clearly reveal the well-ordered olivine $LiFePO_4$ crystal covered with uniform and thin carbon layers (~3 nm). Both XPS and EELS spectra analysis clearly confirmed the amorphous sp2 carbon-coating. It is evident that the uniform carbon coating on the surface of each $LiFePO_4$ particle creates effective pathway networks for both electronic transport and ionic diffusion during the electrochemical testing, and thereby enhances the electronic conductivity and its electrochemical performance. The good rate capability, cycling performance, and high discharge capacity for these C-$LiFePO_4$ nanocomposites would enable the development of long-life lithium-ion batteries with both high energy and high power density. The remarkable rate capability and cycling performance are clearly demonstrated in the $LiFePO_4$ prototype battery cell that designed using the commercial graphite as the anode. The full structural observations and performance evaluations are also helpful to the general understanding of how to produce high-quality C-$LiFePO_4$ cathode in relevance to low-cost appropriate precursors.

Chapter 6

Synthesis and Characterizations of Nano-sized Carbon-Coated $Li_4Ti_5O_{12}$ Nanomaterials

6.1 Introduction

High-rate LIBs with high safety and long cycle lifetime have become very important as one of the promising power sources for a larger scale demanding applications such as EVs and HEVs; and fast charging electric devices.[13,16] When the advanced LIBs are used in the current EVs and HEVs as power sources, they delivers less power than an internal combustion engine. One of the effective approaches to solve such a challenge is to improve the rate and cycle performance of anode electrode applied in the current LIBs.[3,225] So far, spinel lithium titanium oxide $Li_4Ti_5O_{12}$ (LTO) has attracted great interest as a novel anode material for high-rate LIBs instead of the commercial graphite.[137,138,143,226]

As discussed in the previous Chapter 4, pure LTO has a spinel crystal structure with $Fd\bar{3}m$ space group. Lithium ions occupy tetrahedral 8a sites and 1/6 of octahedral 16d sites, while the rest of octahedral 16d sites are occupied by tetra valence Ti ions. The ratio of lithium ions and titanium ions is 1:5. Oxygen ions are located at 32e sites. Thus, the LTO could be expressed as $Li_{(8a)}[Li_{1/3}Ti_{5/3}]_{(16d)}O_{4(32e)}$.[227-229] Interestingly, at the initial stage of discharge, Li^+ ions occupy 8a sites in a spinel structure. As new Li^+ ions insertion takes place during charging process, the inserted Li^+ ions are located at 16c sites. Simultaneously, the Li^+ ions initially located at 8a sites are transported to 16c sites. Such an insertion leads to the electrochemical two-phase transition from spinel-LTO ($Li_4Ti_5O_{12}$) phase to rock-salt LTO phase ($Li_7Ti_5O_{12}$), which is topotactic two-structure transition from $Li_{(8a)}[Li_{1/3}Ti_{5/3}]_{(16d)}O_{4(32e)}$ to $Li_{2(16c)}[Li_{1/3}Ti_{5/3}]_{(16d)}O_{4(32e)}$.[229-231] These two distinct LTO crystal unit cells are shown in Figure 6.1 (a, b), respectively.

There is an extremely flat discharge-charge plateau between the spinel-LTO and the rock-salt LTO crystal during the electrochemical two-phase reaction (Ti^{4+}/Ti^{3+} redox couple) at 1.55 V vs. Li/Li^+ ,[137,143,226]. It is also effective in avoiding the formation of the solid

electrolyte interface (SEI) passive layer on the surface of LTO materials within the operating voltage range. Hence all of these unique merits make the LTO materials competitive as a safe anode material in terms of long cycle life and high cycling safety. [145,227,229-231]

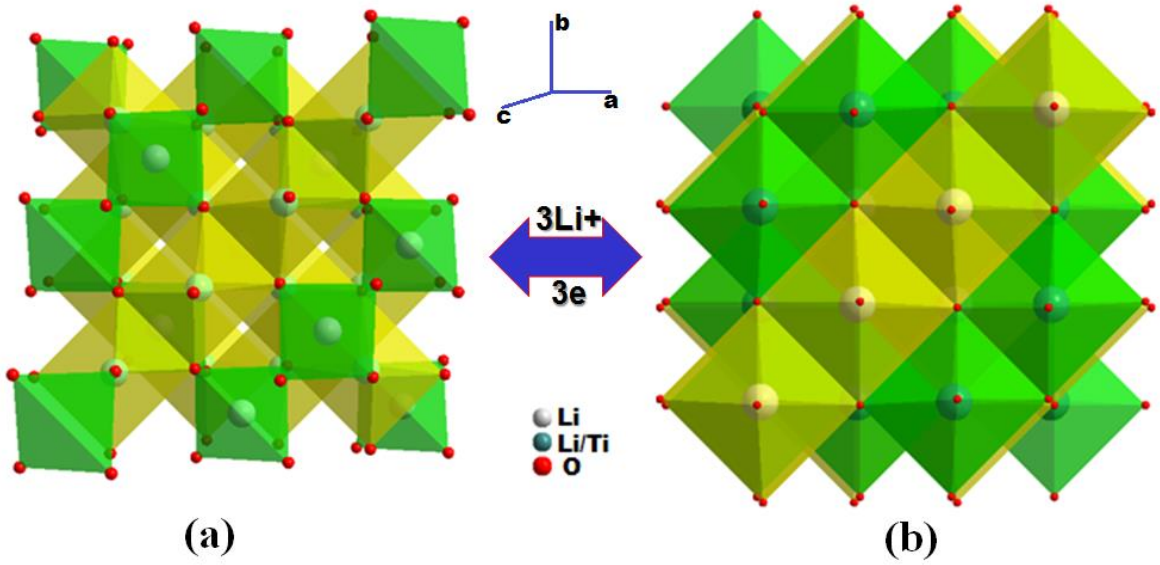

Figure 6.1 Schematic unit cell of (a) spinel $Li_4Ti_5O_{12}$ $[Li_{(8a)}[Li_{1/3}Ti_{5/3}]_{(16d)}O_{4(32e)}]$ and (b) rock-salt-$Li_7Ti_5O_{12}$ $[Li_{2(16c)}[Li_{1/3}Ti_{5/3}]_{(16d)}O_{4(32e)}]$. White spheres denote lithium ions, blue spheres denote disordered titanium ions and lithium ions (Ti: Li = 5:1), red spheres denote oxygen ions

As discussed in the previous Chapter 4, the high-rate performance of pure LTO anode is seriously hindered by its low Li^+ diffusion coefficient (10^{-9}–10^{-13} cm^2/s)[143,232] and inherent low electrical conductivity (<10^{-13} S/cm). A great deal of efforts have been devoted to solve this problem and improve the rate performance of LTO. The popular way is the doping with metal or non-metal ions on Li, Ti or O sites[159,233-241] or surface modification *via* surface coating with conductive species to enhance surface electrical conductivity.[162,242-246] There is a strategy of the effective combination of "conductive surface modification" and "nano-size",[160,247-254] which simultaneously attains high electronic conductivity and a short lithium ion diffusion path to significantly enhance the general electrochemical performance. In

particular, carbon-coated LTO nanostructures have been investigated using various synthetic methods including *ex-situ* and *in-situ* coating methods.[162-164,244,245,255-260] When the source of appropriate carbons is optimized, carbon-coated LTO (C-LTO) nanostructures with uniform coating thickness can be produced effectively.[248,257,261-263] In general, the optimum carbon coating can lead to a reduction of the cell impedance and decrease of the charge transfer resistance. Therefore, it is essential to optimize the coating thickness for carbon-coated anode materials. As a result, the rate capacity can be greatly enhanced. It has been proposed that an ideal structure for high-performance LTO should contain nano-sized particles completely coated with conductive carbon.[162,248,255,257] In addition, high carbon content can contribute to high surface conductivity but thick carbon-coating might restrict transport of lithium ions, and thus is unfavorable for attaining high rate capacities.[257,264-266] Less carbon means thin carbon coating, which is normally linked to non-uniform coatings, which usually leads to poor surface conductivity. Only optimized and uniform carbon-coating can provide good conductivity and fast Li-ion transport in the C-LTO materials.[47, 52, 60, 64] It is critically important to understand in depth the influence of the carbon-coating effects on the electrochemical performance of the LTO anode materials.

In this Chapter, the C-LTO nanoparticles with optimized thin coating layers were successfully synthesized using the combination of solvothermal method and *in-situ* calcination method. Structural characterizations and electrochemical tests of these C-LTO nanoparticles reveal that the synergistic role of optimal amorphous carbon-coating and nano-size particle gives rise to high electrical and ionic conductivity, resulting in enhanced electrochemical performance as applied in LIBs.

6.2 Experimental Details

6.2.1 Solvothermal Synthesis and Solid-State *In-situ* Reaction

Solid-state *in-situ*/*ex-situ* synthesis, which includes several successive steps of pre-treatment and calcination of the stoichiometric mixture of starting materials, is a

conventional and cost-effective method for preparing the C-LTO anode materials.[163,164,245,255-258]

Firstly, the $Li_x(TiO_2)_{1-x}$@C powders with different carbon contents were solvothermally synthesized using commercial anatase TiO_2 powder as raw material and the different stoichiometric amounts of glucose (0.5 g-1.0 g, Fisher, Canada) as carbon source. Typically, a stoichiometric amount (Ti:Li=5:4) of anatase TiO_2 powder (2.75 g, Sigma–Aldrich, USA) was dispersed in ethanol (50 ml) solution of dissolved lithium hydroxide (LiOH, 2.48 g, Fisher, Canada). After stirring the mixture for 30 min at ambient temperature, the suspension was transferred into a 50 mL Teflon-lined autoclave and heated up to 180^{o}C for 10-24 hrs. Subsequently, the solvothermal precursor (e.g., white solid-solution precipitate) was filtered from the solution, and washed several times with deionized water to remove the excess hydroxide before drying at 80^{o}C for 5-10 hrs. The solvothermal $Li_x(TiO_2)_{1-x}$@C precursor was then heated to achieve *in-situ* calcination and carbonization reaction to prepare the carbon-coated C-LTO nanoparticles. Usually, the white solid-solution $Li_x(TiO_2)_{1-x}$@C precursor was calcinated at 850^{o}C for 5 hr in argon atmosphere, followed by natural cooling in the furnace. Finally the grey-black C-LTO nanoparticles were obtained and collected under ambient conditions. Two schematic illustrations of solvothermal reaction and *in-situ* calcination process for the C-LTO particles is shown in Figure 6.2 (a, b). The distinguished color difference between solvothermal $Li_x(TiO_2)_{1-x}$@C precursor and black C-LTO nanoparticles is clearly observed.

Herein, the optimized coating thickness in the C-LTO nanoparticles can be controlled using different stoichiometric amounts of glucose (e.g., 0.5g - 1.0g) during the initial solvothermal synthesis, which is compared with the *ex-situ* calcination process using the stoichiometric amounts of glucose as the mixed carbon source.[266]

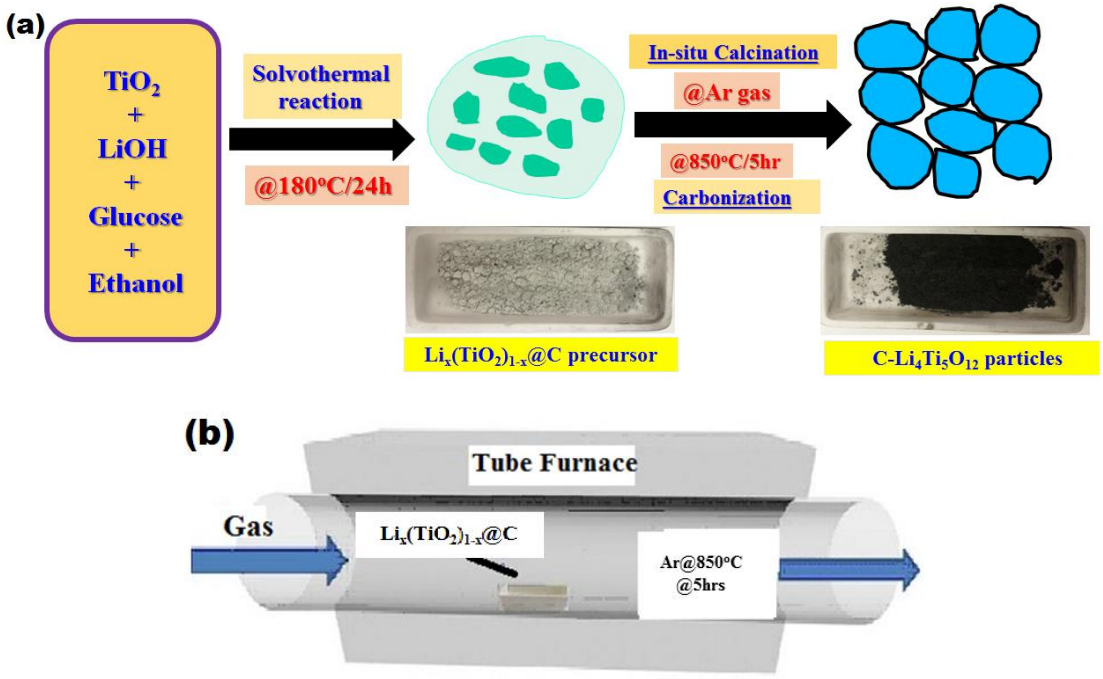

Figure 6.2 (a) Schematic illustration of in-situ synthesis of C-LTO particles by solvothermal reaction and calcination process. **(b)** Schematic illustration of *in-situ* calcination process from solvothermal $Li_x(TiO_2)_{1-x}$@C precursors.

6.2.2 Structure and Carbon-Coating Characterizations

Crystal structures of these C-LTO nanoparticles were examined by powder X-ray diffraction (XRD). Crystalline phases and carbon-coating structure were characterized by TEM imaging, HR-TEM imaging and selected area electron diffraction (SAED) using a JEOL 2010F FEG transmission electron microscope. Atomic resolution structure of STEM-HAADF images were obtained with collection semi-angles from 50 to 180 mrad in spherical aberration-corrected scanning transmission electron microscopy of JEOL 2100F STEM/TEM operated at 200 kV.

For STXM measurements, C-LTO powders were dispersed in methanol by brief sonication, and then deposited on Si_3N_4 windows for measurement. In STXM, the monochromatic X-ray beam is focused by a Fresnel zone plate to a ~30 nm spot on the sample, and the sample is raster-scanned with synchronized detection of transmitted X-rays

to form images. Chemical/elemental mapping for a selected sample region of isolated particles was performed at the C, O K-edges, and Ti L-edge via two-energy image subtraction to generate optical density (OD) image of each element distribution, e.g., 280/292 eV at C 1s, 454/458.5 eV at Ti 2p, and 525/540 eV at O 1s. Image sequences (stacks) over a range of photon energies at these elemental edges were also acquired. The X-ray-Absorption-Near-Edge-Structure spectra (XANES) were extracted from the combined image stack at the regions of submicron sized nanoparticles. STXM data were analyzed by aXis2000 database.[267]

6.2.3 Battery Cell Fabrication and Electrochemical Testing

The coin-type cell was based on the configuration of Li metal (−) |electrolyte| LTO (+). Pure lithium foil was used as the counter electrode. The synthesized C-LTO powders, carbon black and polyvinylidene fluoride (PVDF) binder were mixed in a weight ratio of 80:10:10, respectively, and then were mixed in *N*-Methyl pyrrolidone (NMP) solvent to form homogeneous slurry. The slurry was coated on an Al foil current collector, and dried at 90 °C for 12 h to remove the solvent. The electrodes were punched to form a disk for the half-cell test. The electrolyte solution was 1 M $LiPF_6$ dissolved in a mixture of EC, DMC and EMC (volume ratio is 1:1:1). The cell assembly was carried out in a pure argon-filled glove box (M. Braun Co, Germany).

Galvanostatic charge-discharge cycling tests for the assembled coin cells were performed within a range of 1.0-3.0 V vs the lithium counter electrode using a LAND-CT2001A battery-testing system instrument. The cyclic voltammetry (CV) and rate cycle measurements for the assembled coin cells were performed using the Arbin 2000 testing system at the scan rate of 0.1 mV/s between 1.0-3.0V vs Li^+/Li. Electrochemical impedance spectroscopy (EIS) measurements were carried out over a frequency range of 10^{-2} –10^5 Hz at 5 mV as the applied sinusoidal perturbation.

6.3 Results and Discussions

6.3.1 Structures and Phase Identifications

Five different C-LTO samples were synthesized under different stoichiometric amounts of glucose (e.g., 0.5g - 1.0g). The comparison of crystal phase, carbon-coating thickness and average size is summarized with details in Table 6.1.

It is very clear that the LTO particles sample with carbon-coating thickness of ~ 4.5 nm was eventually achieved by the initial stoichiometric amount of glucose (0.7g, 18.9 wt%) during the in-situ calcination process.

Table 6.1 The comparison of initial carbon contents, carbon-coating thickness, average size, and crystal phase of five different C-LTO samples

	Initial carbon	After calcination	After calcination	After calcination	After calcination	After calcination
Sample No	Carbon content (wt%) (EDX)	Carbon content (wt%) (EDX)	Carbon thickness (nm) (HRTEM)	Lattice parameters (nm) (XRD)	Average size (nm) (XRD, TEM)	Cubic Spinel (XRD, SAED)
C-LTO-01	14% (0.5 g)	2.1	< 1	0.8360	25.2	yes
C-LTO-02	17% (0.6 g)	3.4	< 1	0.8364	25.4	yes
C-LTO-03	18.9%(0.7g)	8.6	~ 4.5	0.8363	26.5	yes
C-LTO-04	21 % (0.8 g)	11.5	~ 8	0.8365	26.2	yes
C-LTO-05	25% (1.0 g)	14.8	≥ 10	0.8362	25.8	yes

Figure 6.3 showed the three HR-TEM images of different carbon-coating thicknesses for three C-LTO samples with different initial stoichiometric amounts of glucose.

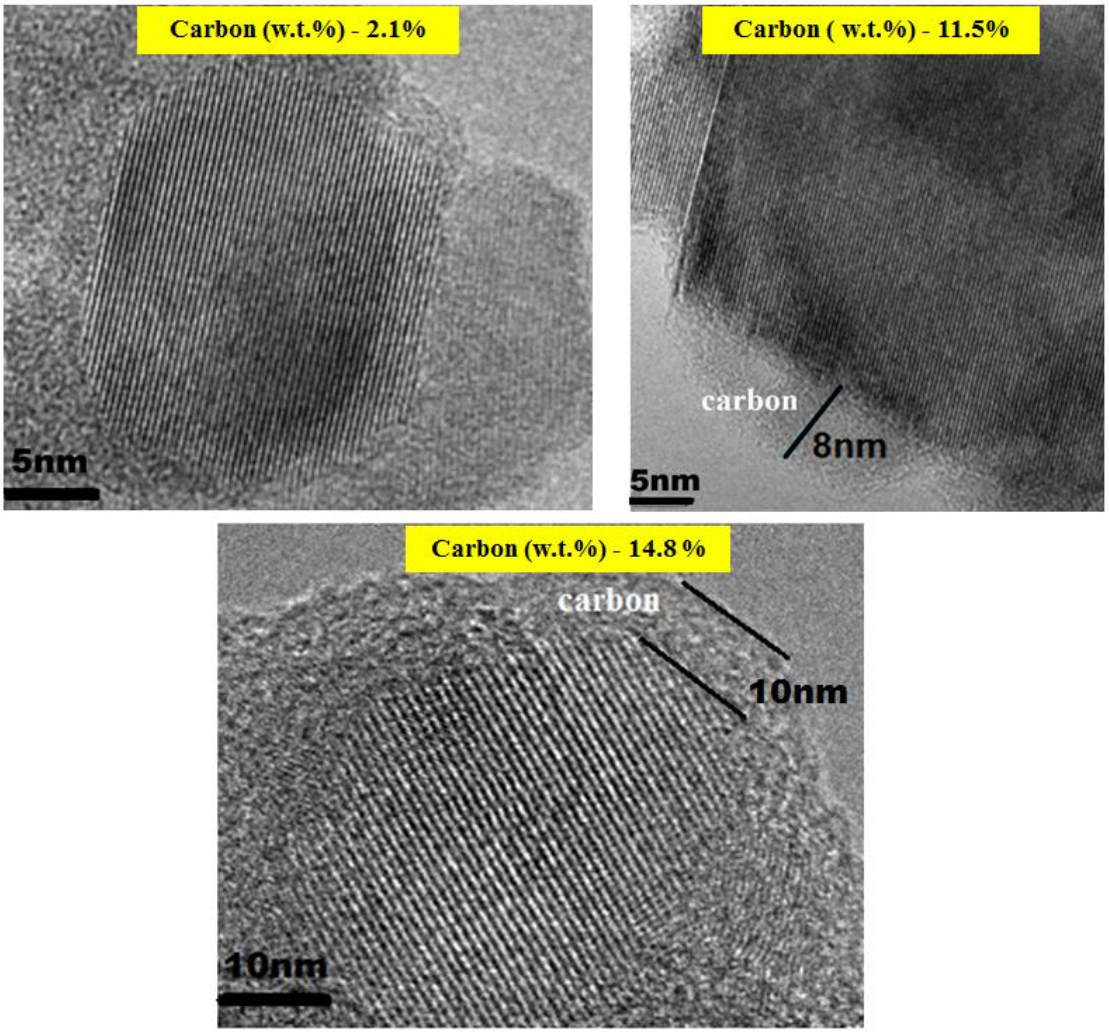

Figure 6.3 HR-TEM images comparing carbon-coating thickness for three different C-LTO samples with different carbon contents.

It is apparent from Figure 6.3 that there is distinct difference of coating-thickness for three C-LTO samples with different initial stoichiometric amounts of glucose. In brief, the carbon-coating is almost negligible when the initial amounts of glucose is 2.1wt%, and the carbon-coating thickness is more than 8 nm when the initial amounts of glucose are 11.5wt% and 14.8wt%.

It concluded that the C-LTO sample with initial stoichiometric amounts of glucose (0.7g, 18.9wt%) gave rise to the optimized carbon-coating of ~ 4.5 nm and the optimized carbon content of 8.6 wt% during the *in-situ* calcination process.

Detailed structure analysis of XRD patterns of the solvothermal $Li_x(TiO_2)_{1-x}$@C precursor (glucose, 0.7g, 18.9 wt%) and the C-LTO nanoparticles (carbon, 8.6 wt%) are shown in Figure 6.4. All the XRD diffraction peaks of C-LTO particles (carbon, 8.6 wt%) exhibit the characteristic diffraction lines of well-crystallized phase without presence of any crystalline carbon. It is in good agreement with JCPDS file (card No. 49-0207),[49] which can be identified as $Li_{(8a)}[Li_{1/3}Ti_{5/3}]_{(16d)}O_{4(32e)}$ and indexed to the cubic system with *Fd*3*m* space group, demonstrating a spinel-LTO structure was successfully obtained. However, XRD pattern of the solvothermal $Li_x(TiO_2)_{1-x}$@C precursor was found to be the mixed solid-solution. The average crystallite size of C-LTO particles is calculated to be around 32 nm from the (111), (311), and (400) diffraction peaks using the Scherrer equation ($D = 0.9\lambda/\beta\cos\theta$, where λ = 0.154 nm (Cu Kα) and β = full width half maximum at the diffraction angle of θ). Because spinel LTO is face-centered cubic, Bragg equation was used to determine the lattice parameter, *a*, by $\lambda = 2d_{hkl}\times\sin\theta$, where (*h k l*) are the Miller indices, λ is the wavelength of the incident X-ray beam (0.154 nm), θ is the incident angle, and *d* is the distance between the atomic layers of the cubic structure. The lattice parameter was calculated to be $a \sim 0.8363$ nm, which is in good agreement with the lattice constant reported for pure spinel LTO,[1] and reveals that carbon is not incorporated in the spinel LTO lattice structure, instead, it is on the surface of each C-LTO nanoparticle. Therefore it can be inferred that the existed carbon content (glucose, 0.7g, 18.9 wt%) inside the solid-solution phase in the solvothermal $Li_x(TiO_2)_{1-x}$@C precursor has contributed to the carbon-coating on surface of the C-LTO particles during the in-situ calcination process, and did not influence the formation of cubic-LTO crystal with high spinel purity.

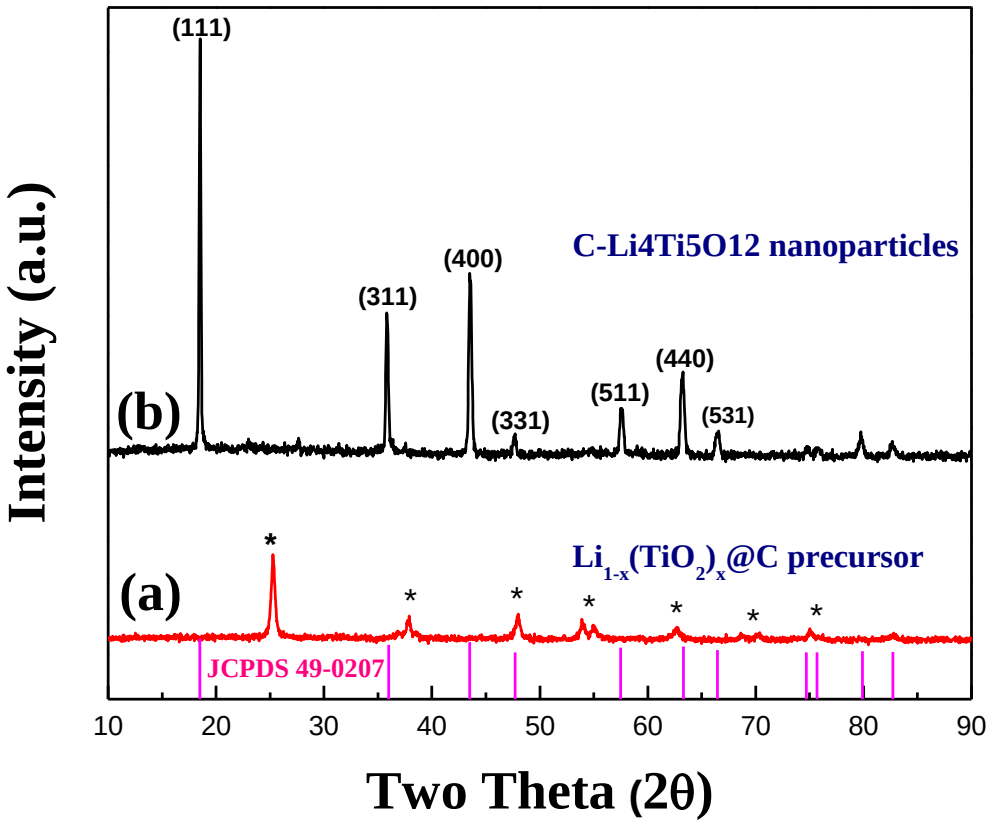

Figure 6.4 X-ray diffraction patterns of (a) the solvothermal solid-solution $Li_x(TiO_2)_{1-x}$@C precursor (glucose, 0.7g, 18.9 wt%) and (b) C-LTO nanoparticles (carbon, 8.6 wt%).

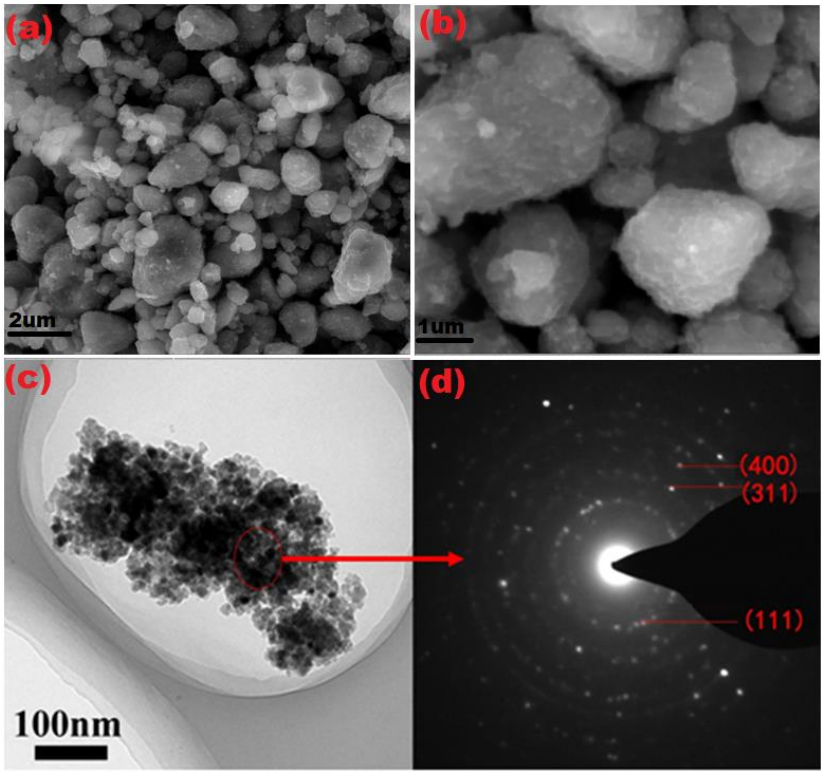

Figure 6.5 Representative SEM images (a, b), low-magnification bright-field TEM image (c) and corresponding SAED pattern (d) for the C-LTO nanoparticles (carbon, 8.6 wt%)

Figure 6.5 shows the representative SEM images, bright-field TEM image and SAED pattern of as-prepared C-LTO nanoparticles using initial stoichiometric amounts of glucose (0.7g, 18.9 wt%). SEM images showed that the C-LTO nanoparticles form relatively few agglomerates and have the diameter of 500 nm - 1 μm. They have smooth surface, which is associated with the good conductivity resulting from conductive surface-coating. TEM image indicates that the as-grown LTO particles have quasi-spherical shape and the estimated diameters are about 20 nm-50 nm, which is in good agreement with the crystallite sizes calculated using XRD pattern. The SAED pattern also confirms the formation of cubic spinel LTO crystal phase with no evidence of crystalline carbon.

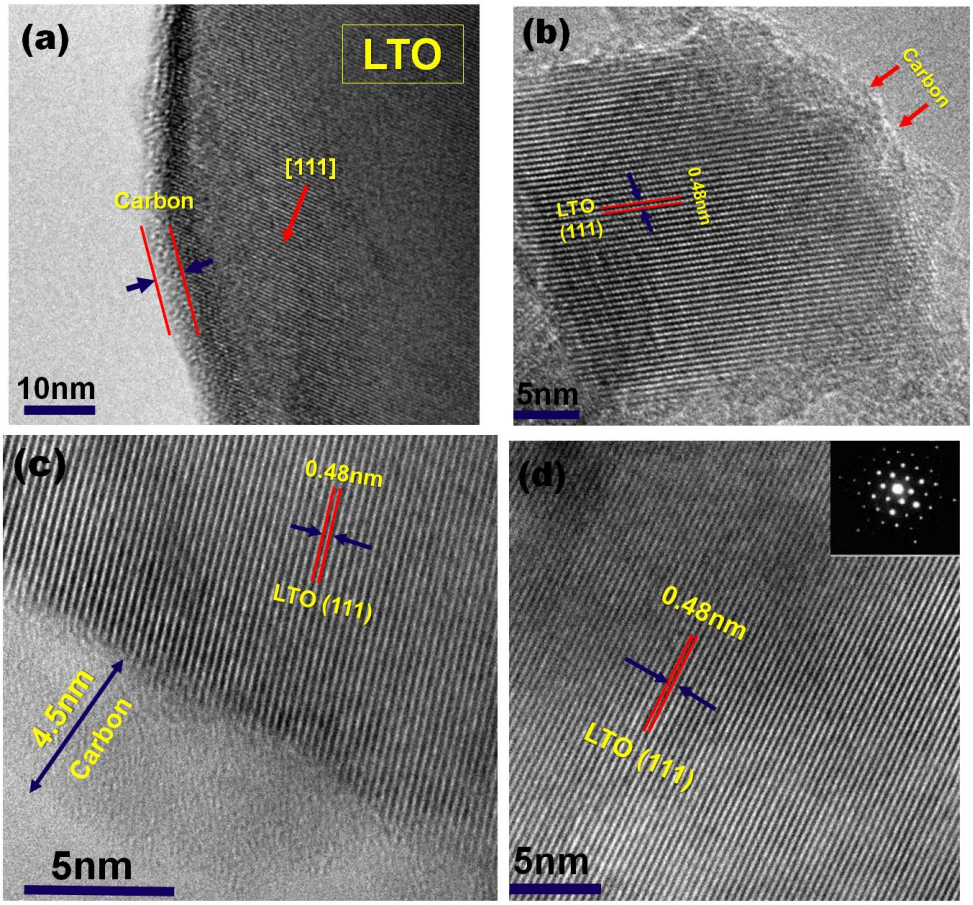

Figure 6.6 HR-TEM images (a-d) and SAED pattern (inset) of C-LTO nanoparticles. The well-crystallized structure and an amorphous carbon layer covering (~4.5 nm) of the surface of LTO particle is clearly observed (a-c)

A series of HR-TEM images of individual C-LTO particle (stoichiometric amounts of glucose, 0.7g, 18.9 wt%) were shown and analyzed in Figure 6.6. The particle has well-crystallized structure with an amorphous carbon layer covering the surface of LTO particle. Meanwhile, it appears that the coating is continuous and uniform with a thickness of ca.4.5 nm, suggesting that the carbon phase (18.9 wt%) in solvothermal $Li_x(TiO_2)_{1-x}$@C precursor played an important role in controlling the coating-thickness during *in-situ* calcination. It has been reported that the amorphous carbon layers can be formed *in-situ/ex-situ* during the calcination process, and heating temperature and time are important factors to control the

final coating thickness.[163,164,248,255-257,264-266,268] Our in-situ calcination time is only 5 hours in the inert environment, and carbon-coating thickness can be adjusted by the calcination temperature. Moreover, HR-TEM images reveal that the well-resolved lattice fringes have an interplanar distance of 0.48 nm, corresponding to the d-spacing of the facets of the spinel LTO structure, which again confirms that the high-purity spinel LTO crystal was synthesized during *in-situ* calcination processing. Similarly, the corresponding SEAD pattern taken from the same particle again confirms the formation of well-crystallized spinel LTO structure.

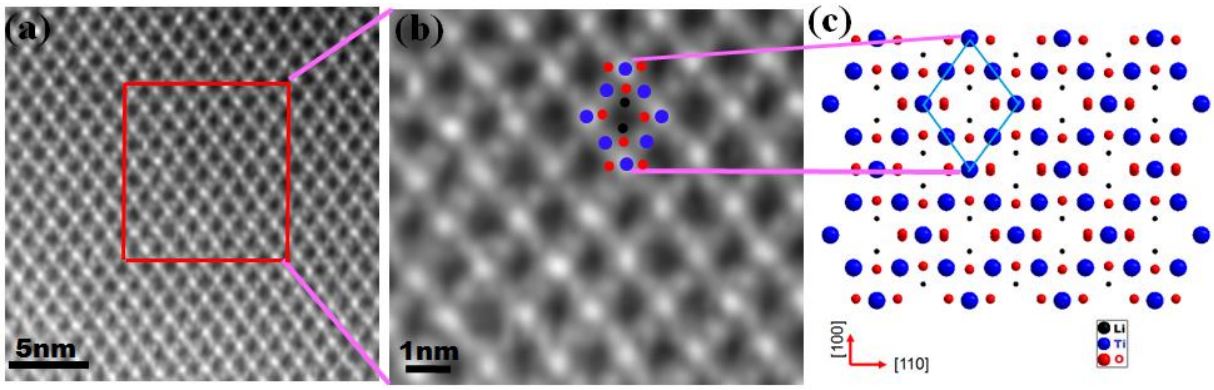

Figure 6.7 (a) High-resolution STEM-HAADF images at atomic scale. (b) The enlarged HAADF panel showed atomic structure of LTO crystal plane, (c) Schematic lattice view of spinel LTO along the [110] direction, corresponding to the 16d, 32e, and 8a sites in the LTO atomic lattice.

Scanning-TEM (STEM) equipped with an annular dark-field detector is a very powerful tool for obtaining useful structural and chemical information with atomic resolution.[269-271] The resultant high-angle-annular-dark-field (HAADF) STEM images (>50 mrad) exhibit a strong dependence of scattering electron intensity on atomic number (Z), which is also called the Z-contrast image, and could be used for the quantitative differentiation between atoms of different elements. High-spatial resolution in STEM had

been limited by the spherical aberration (Cs) in the condenser lens, which is now compensated by the implementation of aberration correctors (Cs-corrected) for this spherical aberration, allowing for the generation of sub-angstrom images (i.e., < 0.1 nm).[272-274] Currently, Cs-corrected STEM technique allows us to obtain atomic-resolution HAADF images and count the number of atoms in an atomic column of a crystal. The typical high-resolution STEM-HAADF images at the atomic scale are shown in Figure 6.7a. The titanium atom sites (16d), lithium atom sites (16d) and oxygen atom site (32e) can be clearly visualized in the enlarge atomic resolution HAADF image (Figure 6.7b), which is consistent with the atomic occupancies in schematic lattice view of spinel LTO along the [110] direction, as shown in LTO [110] projection model in Figure 6.7c,[78-79] Bascially, such a [110] projection of spinel LTO is most suitable for observing Li, O, and Ti atoms directly, because separate columns of these atoms are aligned in this [110] direction.[272,275] As such, the pure spinel LTO phase was synthesized and further confirmed.

Synchrotron-based STXM imaging and XANES spectroscopy have been effectively used for studying the electronic and chemical structures of electrode materials for lithium ion batteries.[276-278] XANES is an element specific technique, in which core electron is excited from the ground state to probe the partially filled or empty excited states, hence giving useful information about geometry and oxidation state of the element interested.[279] Spectro-microscopy studies were done using STXM, allowing for the generation of the spectra with high spectral and spatial resolution.

Figure 6.8a displays STXM chemical/elemental imaging of submicron sized C-LTO particle assemblies. It is evident that Ti and O are majority elements in the sample, while carbon intensity is much lower, yet still somehow uniformly distributed on the particle surface, which confirmed that the very low thickness regions were dominated by amorphous carbon. This is consistent with the above HR-TEM and STEM characterization revealing thin amorphous carbon coating on the LTO particles.

Furthermore, quantitative XANES spectroscopy was recorded on the selected submicron sized C-LTO particles in the same sample region via STXM image stacks as a function of photon energy.[278]

Figure 6.8b shows the C K-edge XANES spectrum extracted from the STXM stacks. The relatively weak C 1s spectrum confirmed lower carbon content. In addition, primarily amorphous sp^2 structure with C=C bonding (i.e. 285.3 eV) was presented in the carbon content of the C-LTO particles. Strong oxygen functional groups was also revealed and presumably due to the bonding interaction between the carbon coating and the nanoparticles. Ti L-edge XANES of Figure 6.8c demonstrated Ti^{4+} valence state and a significant crystal field splitting pertaining to the octahedral geometry for the core Ti^{4+} ion (3d orbital) coordinated with six O^{2-} ions (2p orbital).[241,277,280] O K-edge XANES in Figure 6.8d is found to be consistent with the octahedral Ti-O bonding and TiO_6 geometry in the spinel LTO structure. [241,281]

Figure 6.9 showed spatially-resolved XANES spectra of C-LTO nanoparticle assemblies extracted from the STXM image stacks. Figure 6.9**a** shows STXM optical density image of the measured sample region, which was averaged from all stack images at the C K-edge, Ti L-edge and O K-edge. The enclosed color lines indicate the regions of interest on C-LTO for extracting XANES spectra, (red corresponds to the thick region; between red and green is the middle thickness region; between green and blue is the thin region). The C K-edge in Figure 6.9c reveals that the total carbon thickness in the thin region is 9 nm, inferred from the C K-edge jump. The average thickness of carbon-coating can be accordingly calculated to be 4.5 nm, taking into account this is the least aggregated region and STXM is a transmission technique. Herein a specific model is shown in Figure 6.10, which indicate that each C-LTO particle surface coating will be passed twice by the X-ray beam, so the measured thickness is doubled. On the other hand, another proposed model of C-LTO particles aggregate is shown in Figure 6.11, which assuming middle and thick regions consist of aggregated particles of much larger sizes. In other words, the thicker the region, the larger the particle agglomerates.

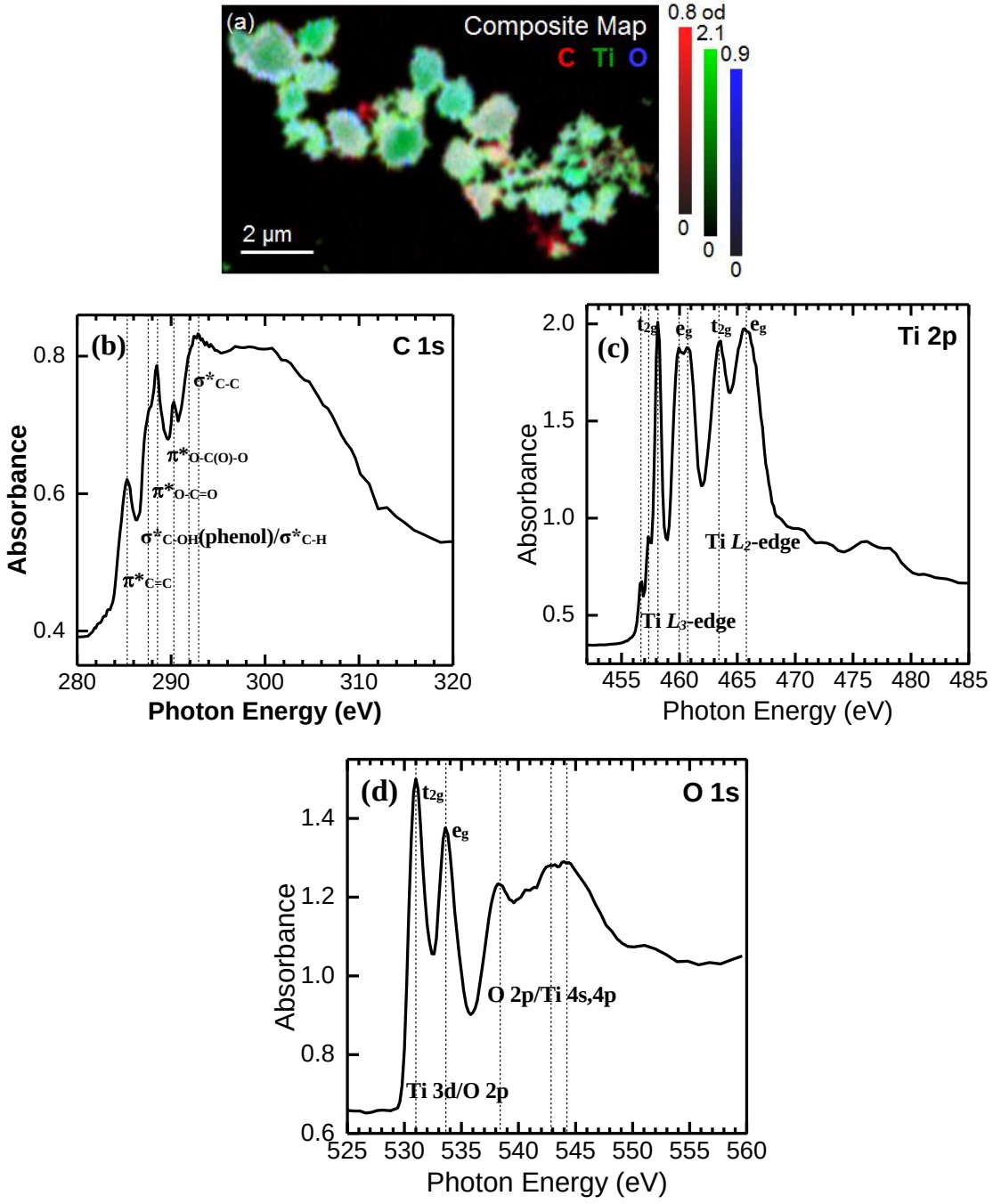

Figure 6.8 (a-d) STXM chemical imaging and XANES spectra of C-LTO nanoparticles assemblies, (a) colour composite chemical map, red: carbon, green: titanium, blue: oxygen, all vertical color grey scales on the right represent sample optical density in each element; (b-d) C 1s, Ti 2p and O 1s XANES spectra of the selected submicron sized C-LTO particles aggregates.

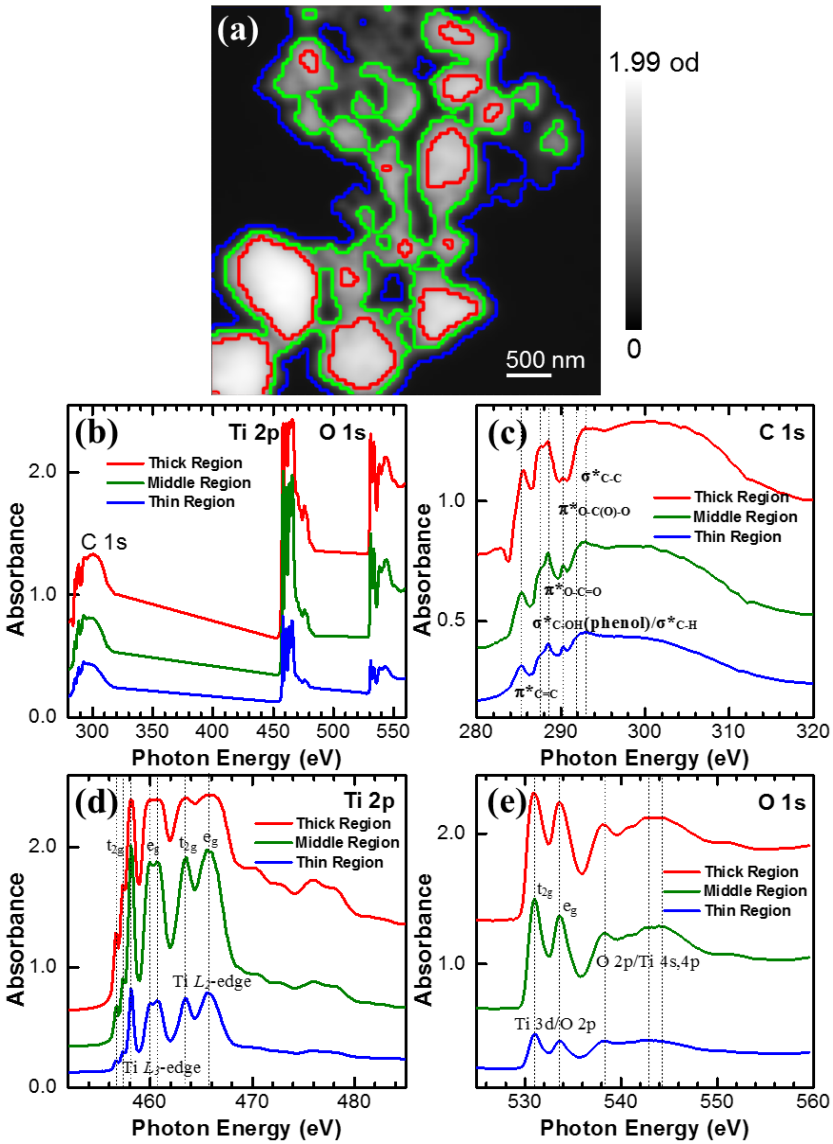

Figure 6.9 (a-d) STXM spatially-resolved XANES spectra of C-LTO nanoparticle assemblies, (a) STXM optical density image of the measured sample region (the image was averaged from all stack images at the C K-edge, Ti L-edge and O K-edge), the enclosed color lines indicate the regions of interest on C-LTO for extracting XANES spectra, red: thick region, between red and green: middle thickness region, between green and blue: thin region, the vertical scale on the right represents the averaged optical density; (b) all edges, (c) C 1s, (d) Ti 2p, and (e) O 1s XANES spectra from the selected regions of interest in (a).

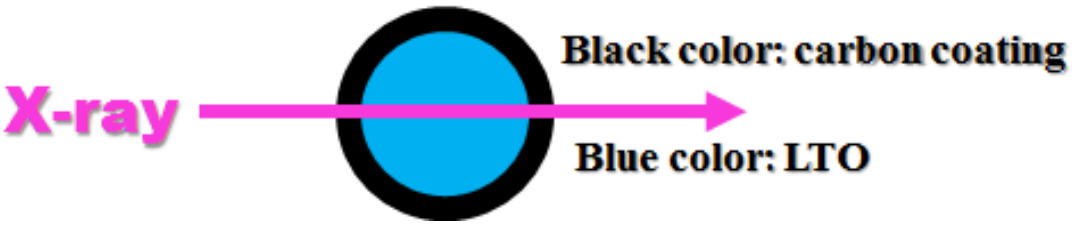

Figure 6.10 Schematic illustration of synchrotron-based X-ray transmission technique on C-LTO nanoparticle. Synchrotron-based STXM is a transmission technique, each C-LTO nanoparticle surface coating will be passed twice by the X-ray beam, so the measured thickness is doubled.

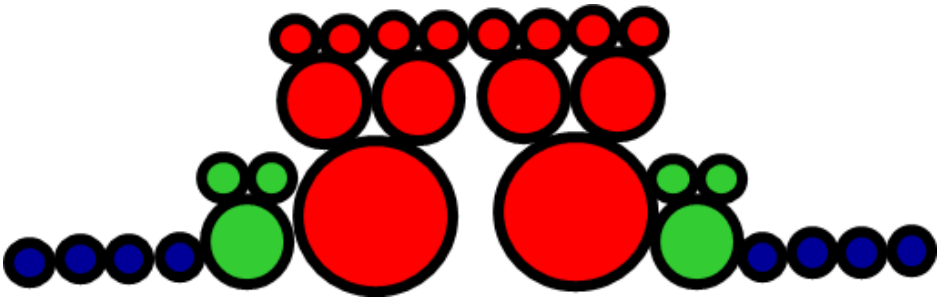

Figure 6.11 The proposed C-LTO nanoparticles assembly's model, assuming middle and thick regions have C-LTO nanoparticles aggregates with much larger sizes

From the above studies, it is evident that the STXM characterization of carbon structure and coating thickness is in a good agreement with the HR-TEM images and HAADF analysis.

6.3.2 Electrochemical Analysis

To demonstrate their potential application as anode materials for the LIBs, electrochemical performance of C-LTO particles has been evaluated and shown in Figure 6.12. The lithium storage properties were firstly examined using cyclic voltammetry (CV). Figure 6.12a shows the CV profile of C-LTO electrode assembled in a coin-type half-cell using lithium as the reference electrode. At a scan rate of 0.1 mV s^{-1} between 2.5 and 1.0 V, a pair of well-defined sharp redox peaks was observed at 1.60/1.50 V, which could be

attributed to the redox reaction of Ti^{4+}/Ti^{3+}. Such a reversible pair of redox peaks within each CV curve indicates that a well-defined electrochemical cathodic and anodic process has occurred from the spinel LTO structure. The cathodic peak located around 1.50 V corresponds to the voltage plateau of the discharge process in which Li-ion inserts into the spinel LTO, the anodic peak located at 1.60V corresponds to the voltage plateau of the charge process in which Li-ion extracts from the rock-salt LTO.

This is a typical character of the two-phase reaction mechanism for spinel-LTO/rock-salt-LTO, as shown by the following equation.[137,138,143,226,227,229,232,261]

$$Li_4Ti_5O_{12}\ (\text{spinel-LTO}) + 3Li^+ + 3e \rightleftharpoons Li_7Ti_5O_{12}\ (\text{rock-salt-LTO}) \quad E = 1.5\ V$$

In addition, the strong and sharp redox peaks indicate well-behaved electrode kinetics of the C-LTO electrod. It is apparent that the initial three cycles almost overlap between 1.0 and 2.5 V at a scan rate of 0.1 mV/s, confirming Li-ions insertion into and extraction from the C-LTO electrode is reversible and fast, which is consistent with that of pure spinel-LTO structure, where the ions at titanium tetrahedral sites are involved in the charge/discharge process. The CV features also reveal that the C-LTO nanoparticles have high-purity spinel phase. Figure 6.12b shows the first and second galvanostatic discharge–charge cycles of the C-LTO cell in a voltage range of 1.0–3.0 V at a current rate of C/2. It is evident that the discharge process (Li insertion) consists of three stages: an initial stage of quick voltage drop, a second stage with a distinct voltage plateau, and the third stage exhibiting a gradual decay in potential. The discharge-charge potential plateau was observed at ~1.55 V due to the redox reaction of Ti^{4+}/Ti^{3+} couple. Furthermore, two galvanostatic discharge–charge cycling plateaus seemed to be overlapped, and the excellent reversibility was observed from this two galvanostatic discharge–charge cycles, indicating no irreversible lithium insertion process and battery cell polarization was involved. In fact, the electrochemical behaviour under a galvanostatic cycling agrees well with the CV studies, further confirming that the C-LTO nanoparticles have highly crystalline spinel-structure. The first-discharge reversible

capacity value is equal to 166 mAh/g, which corresponds to the intercalation of ~1 mol of lithium ion per formula unit and also corresponds to 94% of its theoretical capacity of 175 mAh/g, while the Coulombic efficiency steadily kept values of ~ 99%. After the first discharge–charge process, the second discharge-charge cycle of the C-LTO electrode delivers a stable discharge capacity of about 162 mA h/g, demonstrating that the C-LTO particles exhibit a high-rate capability as anode materials for LIBs. The rate capabilities of the C-LTO electrodes were employed to evaluate the rate performance and cycling stability from low to high rates.

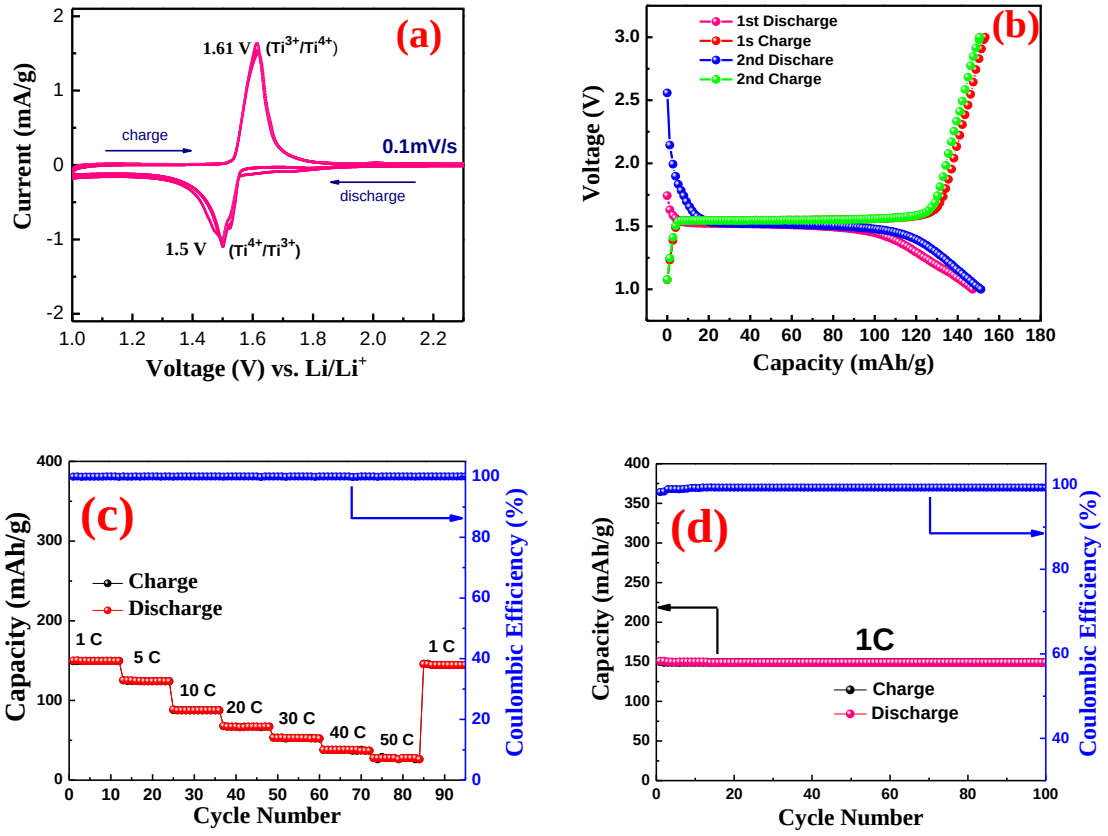

Figure 6.12 Electrochemical characterizations of the C-LTO particles, (a) cyclic voltammetry (CV) at a scan rate of 0.1 mV/s, (b) the first and second galvanostatic charge-discharge cycles at a rate of C/2, (c) the rate capabilities at different rates from 1C to 50C, (d) cycle performance and Coulombic efficiency at 1C rate.

Figure 6.12c showed the rate capabilities and discharge capacity retention during cycling at various C-rates over the voltage cut-off range of 1.0–2.5 V. The electrode was progressively charged and discharged in a series of stages with rates from 1C to 50 C over the voltage cut-off range of 1.0–2.5 V. It is seen that the reversible capacity of C-LTO electrode at 1C rate (here the charge and discharge rates are the same) is 155 mAh/g and retained reversible capacity after over 80 cycles is 150 mAh/g. Such a reversible capacity retention indicated the rate capability of the C-LTO particles has improved to a certain extent and is sufficiently stable for high-rate cycling. It is well-known that the rate capability relies on both electronic conductivity and ionic transport. As-synthesized C-LTO nanoparticles could effectively shorten the lithium ion diffusion channel, and improve the diffusion rate of lithium ion and then increase the rate capacities of the LTO electrode. Here it was found that the Coulombic efficiency during cycling is being ~ 100%, which could be attributed to thin carbon-coating that effectively improve the electronic conductivity and greatly reduces the polarization of the LTO electrode. Indeed, both high reversible capacity and Coulombic efficiency are beneficial for the high rate performance of LIBs. The cycling performance at a high current density is an important parameter for EV battery. Figure 6.12d showed the cycle performance and Coulombic efficiency at constant current density of 1C. It is obvious that C-LTO anode demonstrated enhanced cycling performances and high Coulombic efficiency at 1 C rate, which also confirms better kinetics and better lithium storage performance for these C-LTO nanoparticles materials.

Apparently, this enhancement of the rate and cycle performance could be associated with smaller particle size and the presence of electrically conductive carbon coating, which may be attributed to four aspects: (1) high-purity spinel-LTO phase provides high capacity; (2) the nanosize effect significantly reduce the distance for the electron and lithium ion diffusion inside LTO particles; (3) uniform thin carbon-coating provides an improved surface electron conductivity; and (4) high surface area of nanoparticle size provides a high electrode/electrolyte contact area, which results in a low electrochemical reaction resistance during the rapid charge/discharge process.

As mentioned earlier, it was reported that low carbon content could barely improve the electrical conductivity while high amount of carbon would rather hinder the ionic conductivity.[248,264-266,268] Generally, the charge-transfer reaction takes place at the LTO electrode upon accepting both Li^+ and electrons. For pure bare LTO, the particle surface is easily accessible to Li^+, but suffers from the lack of electrical conductivity. Electron conduction is facilitated by the carbon coating. For Li^+ transport, there is a facile way to reach the LTO particle surface by coating a thin carbon layer. In the presence of a thick carbon layer, the Li^+ diffusion path may be blocked due to graphitic stacking. This hampers ionic diffusion and accounts for the limited rate capability of the C-LTO particle. Thus a critical balance between the electronic and the ionic transport is necessary to attain remarkable performance by optimizing the carbon content and coating-thickness.[245,246,283,284]

It can be concluded that the enhanced charge–discharge capability, rate capability and cycle performance of the C-LTO nanoparticles could be ascribed to the synergistic effect of increased electrical conductivity and facile Li^+ ion diffusion from the combination of the optimized thin carbon-coating and high-purity spinel-LTO nanocrystal.[251,257,263,265,266,268,285,286]

To clarify the effect of carbon-coating on the electrochemical kinetics and further understand the relationship between the electrochemical performance and electrode kinetics of these C-LTO particles as anode in LIBs, electrochemical impedance spectroscopy (EIS) was measured at the frequency range between 100 kHz and 10 mHz. The EIS method has been considered as an effective method to identify diffusion phenomena in the electronic and ionic mixed conductors.[259,260] As mentioned previously, Li-ion electrochemical insertion/extraction process is shown as:

$$(\text{Charge, } Ti^{3+} \rightarrow Ti^{4+})\ Li_{4/3}Ti_{5/3}O_4 \ \rightleftharpoons\ Li_{7/3}Ti_{5/3}O_4\ (\text{Discharge, } Ti^{4+} \rightarrow Ti^{3+})$$

EIS was measured on the C-LTO coin cell in the fully charge state (activated cell), the Nyquist plot (Z_{re} *vs* Z_{im}) of the EIS spectra was presented in Figure 6.13a. Such a Nyquist plot data can be fitted by an equivalent circuit model as shown in the inset of Figure 6.13a.

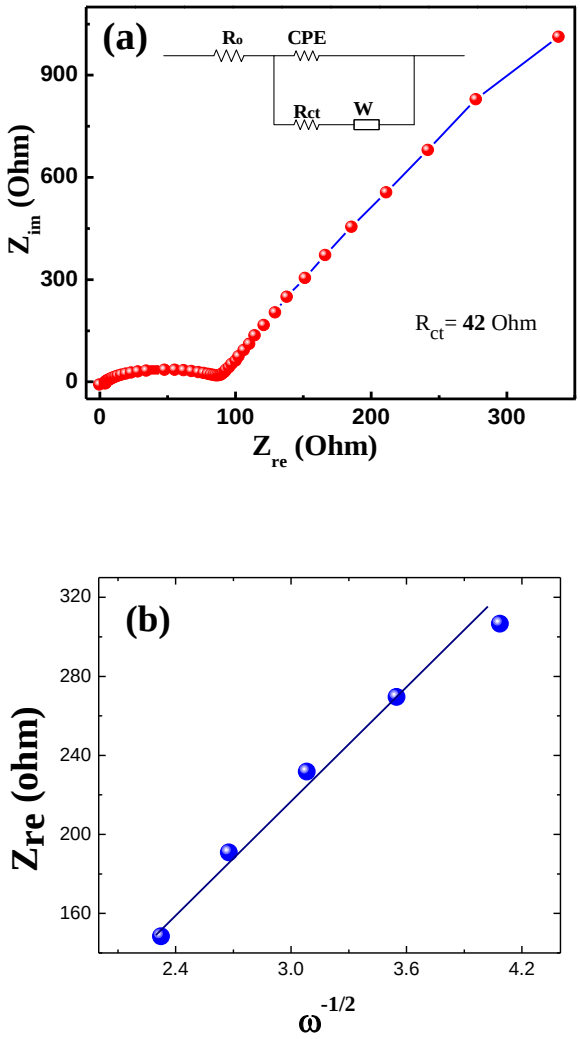

Figure 6.13 Electrochemical impedance spectroscopy (EIS) for C-LTO electrode at the frequency range between 100 kHz and 10 mHz. (a) The Nyquist plot (Z_{re} vs Z_{im}) from EIS measurement at the frequency range between 100 kHz and 10 mHz. The equivalent circuit model is shown in the inset, (b) the plot of Z_{re} against $\omega^{-1/2}$ at low frequency region obtained from EIS measurements.

Apparently, the Nyquist plot has an intercept at high frequency, followed by a depressed semicircular in the medium-to-high frequency region and a ~45° sloping line in the low frequency region. The intercept at the Z_{re} axis in the high frequency region was attributed to the Ohmic resistance, representing the resistance of the electrolyte. The semicircular plot in the medium frequency range is associated with the charge transfer resistance (R_{ct}) of the electrochemical reaction, and the ~45° sloping line in the low frequency region represents the Li-ions diffusion within electrode, namely the Warburg impedance.[287,288]

In general, smaller charge transfer resistance is beneficial for the kinetic behaviors during charge/discharge process. The R_{ct} value is calculated to be around 42 Ohm. It is obvious that this R_{ct} value of the C-LTO nanoparticles is lower than the reported values in the literature.[160,250,251,253,256,289]

Usually, small R_{ct} forces both Li^+ ions and electrons to react immediately, thus accelerating the transport of the polarons of both Li^+ ions and electrons within the electrodes. This is favorable for the kinetic reactions during electrochemical charge/discharge process.

On the other hand, EIS is also an important tool for evaluating the diffusion coefficient of the Li-ion within the particles. The diffusion coefficient of the Li-ion (D_{Li}) is calculated according to the following equation: [257, 290,291]

$$D_{Li} = R^2T^2/2A^2n^4F^4C^2_{Li}\,\sigma^2$$

Where D is the diffusion coefficient, R is the gas constant, T is the absolute temperature, A is the surface area of the cathode (1 cm^2), n is the number of electrons

transferred in the half-reaction for the redox couple (Ti^{3+}/Ti^{4+}), which is equal to 1, F is the Faraday's constant, C_{Li} is the concentration of lithium ion in solid (4.37×10^{-3} mol/cm^3),[291] ω is the angular frequency ($\omega = 2\pi f$), σ is the Warburg factor and has a relationship with Z_{re} as the equation of $Z_{re} = R_{ct} + R_s + \sigma\omega^{-1/2}$. The plot of

Z_{re} *vs* $\omega^{-1/2}$ is presented in Figure 6.13b. The σ value can be obtained from the slope of the plot of Figure 6.13b. [291]

Warburg factor (σ) and the lithium diffusion coefficient (D_{Li}) are calculated to be 95 ± 0.5 and 2.1 - 3.1 × 10^{-12} cm^2/s, respectively. Such a value of the D_{Li} is one or two orders of magnitude higher than the values for the LTO anode materials in previous reports.[18,149,160,256,257]

The larger D_{Li} for the C-LTO particles suggests that the transport of the Li-ions can satisfy the reaction requirement at large charge and discharge current with a low charge transfer resistance. In fact, the R_{ct} of the electrode depends on the electronic and ionic conductivity. During the Li-ions electrochemical insertion and extraction reaction, both electrons and Li-ions must reach or leave the reaction point in the electrode materials simultaneously. Thus, the electrode material with an improved rate performance must have both high electronic and ionic conductivity.

As a result, the electrochemical performance of these C-LTO particles has been significantly improved by low charge transfer resistance (R_{ct}) and high lithium diffusion coefficient (D_{Li}). As well, the EIS measurement is consistent with the CV profiles and the cycling study.

Figure 6.14 showed the comparison of electrochemical rate capabilities for three C-LTO particles samples with different carbon-coating thickness as indicated in Figure 6.3 and 6.4, it is very clear that the optimized uniform and thin carbon-coating (e.g., 4.5 nm) on the surface of LTO anode has been proven to enhance its electrochemical performance effectively at different rates from 1C to 50 C.

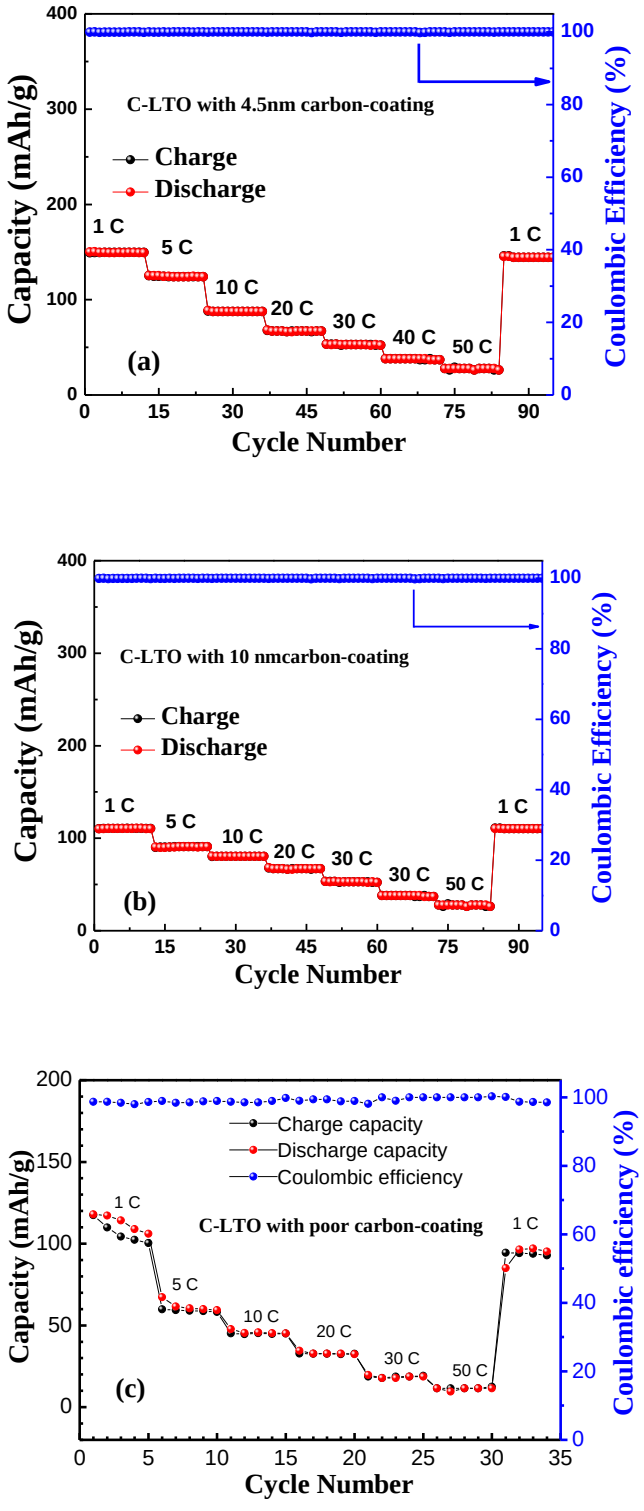

Figure 6.14 The comparison of electrochemical rate capabilities for three C-LTO particles samples with different carbon-coating thickness at different rates from 1C to 50C.

6.4 Comparison of Cycling Testing of the $Li_4Ti_5O_{12}$ Battery Cell

The comparison of two C-LTO samples materials and one commercial LTO sample was evaluated in coin half cells with lithium as the negative electrode at IMRA America, Inc, MI, USA.

Brief summary of three LTO electrode preparations was shown in Table 6.2. Herein, the current collector used was aluminum foil (Al), the electrolyte was used as the commercial solvents of 1 M $LiPF_6$/PC. Testing condition was a constant current charge/discharge at 1A/g, continuously for 1000 cycles. Two samples of C-LTO anode materials were denoted as **A** and **B**, as the commercial LTO sample was denoted as **C,** and was purchased from https://www.electrodesandmore.com.

Table 6.2 Brief summary of three types of LTO electrodes

A(C-LTO: 850ºC/5hrs)	Composition: 70wt% active material/20wt% PVDF/10 wt% Acetylene Black	Loading 1.8 mg/cm^2
B(C-LTO: 850ºC/5hrs)	Composition: 70wt% active material/20wt% PVDF/10 wt% Acetylene Black	Loading 1.6 mg/ cm^2
C (Commercial LTO)	Composition: 70 wt% active material/20wt% PVDF/10 wt% Acetylene Black	Loading 1.8 mg/cm^2

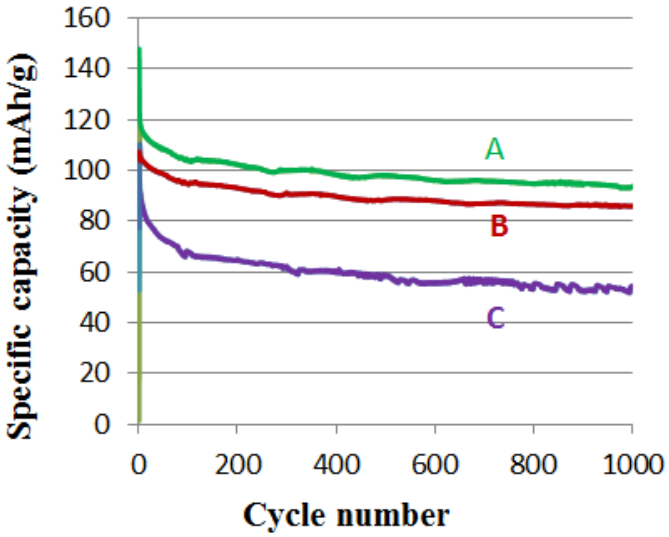

Figure 6.15 The comparison of cycling performance for C-LTO coin cells with lithium as the negative electrode

As shown in Figure 6.15, excellent cycling performance has been clearly demonstrated for these two C-LTO samples, as compared with the commercial one. Both cycling lifetime and remaining discharge capacity is 20% - 40% higher than the commercial LTO samples. Those C-LTO anode samples have the potential for lithium-ion batteries with improved cycling performance and high-rate capacity. On the other hand, uniform carbon coating on the surface of LTO anode has been proven to enhance its electrochemical performance effectively.

6.5 Chapter Conclusions

Amorphous thin carbon-coated LTO nanoparticles have been directly synthesized by a facile solvothermal method followed by a calcination treatment. Comprehensive structural characterizations including advanced imaging techniques such as TEM, HRTEM, HAADF, and STXM confirmed that the C-LTO nanoparticles have a well-defined spinel nanocrystal structure with average size between 20-70 nm, and exhibited the spherical particle shape with amorphous carbon-coating of uniform thickness of ca. 4.5 nm. Systematic electrochemical studies on C-LTO nanoparticles as the LIB anode, have demonstrated an enhanced performance in terms of rate capability, cycling life, capacity retention, and Coulombic efficiency. The improved electrochemical performance can be ascribed to high phase purity as well as the enhanced intrinsic electronic conductivity and Li-ions diffusion resulting from the synergistic effect of nano-structure, optimal carbon-coating and uniform thin thickness that is beneficial for improving the kinetic process and electron transport. This improved cycling performance has been confirmed by the comparison with the commercial samples, which makes these C-LTO nanoparticles a highly promising material for use in the development of high-rate rechargeable lithium-ion batteries, as well as provides the guidance to explore the facile approach for synthesizing LTO anode with improved performance.

Chapter 7

Conclusions, Concluding Remarks and Future Outlook

7.1 Overall Conclusions

The objective of this PhD thesis work is dedicated to the study of nanostructured cathode and anode material for the development of next generation of green and sustainable lithium-ion battery system with high capacity density and long cyclic life, as well as their demanding applications on high-power stationary backup systems and/or advanced electric vehicles (EVs). To meet the stringent technical requirement for stationary and EVs application, my research efforts are focused on increasing the energy/power density and reducing the energy cost of these electrodes. Controllable synthesis, structure characterizations and performance evaluation of the good electrodes candidates of $LiFePO_4$ cathode and $Li_4Ti_5O_{12}$ anode nano-materials have been investigated systemically. Based on the comprehensive experimental studies, the overall conclusions can be drawn as the following:

I. Morphology–controlled Synthesis of Carbon-coated $LiFePO_4$ Cathode Nanocomposites and Related Electrochemical Performance

Carbon-coated $LiFePO_4$ (C-$LiFePO_4$) nanocomposites have been directly synthesized by an economic solid-state reaction process. A variety of analytical techniques such as X-ray diffraction (XRD), TEM imaging, HRTEM imaging and STEM-HAADF imaging are applied to investigate particles morphologies and phase structures. Single phase and olivine structure of the spherical $LiFePO_4$ nanocrystals are confirmed by XRD pattern, HRTEM images and SAED patterns. The details of the coating including carbon content, thickness, and structure are studied by energy filtered-TEM imaging, EELS analysis, and XPS analysis. The size distribution is estimated at 50-100 nm from XRD analysis and TEM images. A homogenous ~ 3 nm carbon layer on the particles surface is clearly revealed by

HRTEM and EF-TEM imaging. The characteristics of these nanostructures and the amorphous carbon-coating has been demonstrated to improve the electronic conductivity and cell performance by reducing the path of both electron transfer and lithium ions diffusion while the C-$LiFePO_4$ cathode is used in the battery cell. Electrochemical performance of the C-$LiFePO_4$ particles exhibited improved electric conductivity, good rate capability, capacity retention, and cycling performance and superior discharge capacity with delivery of almost 99% of its theoretical discharge capacity of 168 mAh/g at a C/10 rate with a high Coulomb efficiency. The CV profiles show that lithium ions and electrons are quite active during two-phase kinetic reaction, which could be attributed to the small particles and carbon-coating layer that facilitated extraction and insertion of lithium ions and electron transfer.

The practical performance of these C-$LiFePO_4$ nanomaterials as cathode was performed with a prototype of 18650-type battery cell manufactured by using the commercial graphite as the anode active materials. The remarkable rate capability and cycling performance are clearly demonstrated in the 18650-$LiFePO_4$ prototype battery. This investigation showed that the low cost and direct solid-state preparation can produce the active $LiFePO_4$ cathode for the development of high-power Li-ion batteries.

II. Facile Synthesis and Characterizations of Carbon-Coated $Li_4Ti_5O_{12}$ Anode and Related Electrochemical Performance

Carbon-coated $Li_4Ti_5O_{12}$ nanoparticles have been synthesized by a facile solvothermal method and an *in-situ* calcination process. Carbon-coating and crystal phases were characterized in details using X-ray diffraction, transmission electron microscopy, and x-ray microscopy techniques. Amorphous carbon-coating with optimal thickness of 4.5 nm on the surface of $Li_4Ti_5O_{12}$ is obtained using the optimized amounts of carbon source and *in-situ* calcination temperature. The carbon-coated $Li_4Ti_5O_{12}$ material has cubic spinel-type crystal structure with the varying size between 20 and 50 nm. The electrochemical kinetic performance has been evaluated as an anode in a half-cell battery configuration using

galvanostatic charge/discharge tests, cyclic voltammetry (CV) and electrochemical impedance spectroscopy (EIS). This $Li_4Ti_5O_{12}$ battery has demonstrated greatly improved cycling performance, high reversible capacity, high Coulombic efficiency of 95%, large lithium diffusion coefficient ($D_{Li} \sim 10^{-12}$ cm^2/s) and high-rate capabilities with the capacity retention of 155 mAh/g at 1C. These improved lithium storage properties can be attributed to the combination of uniform thin carbon-coating and high-purity spinel $Li_4Ti_5O_{12}$ nanocrystal, which increases electron transport and facilitates lithium-ion insertion/extraction simultaneously throughout the electrode, making these carbon-coated $Li_4Ti_5O_{12}$ nanoparticles an excellent anode material for high-rate lithium ion battery applications.

The practical performance of the $Li_4Ti_5O_{12}$ nanomaterial as anode was conducted with a half-cell battery prototype, using the commercial $Li_4Ti_5O_{12}$ nanomaterial as the comparative active materials. The improved cycling performance is clearly demonstrated in the half-cell $Li_4Ti_5O_{12}$ battery.

7.2 Concluding Remarks

Lithium-ion batteries based on spinel-$Li_4Ti_5O_{12}$ anode and olivine-$LiFePO_4$ cathode have showed the attributes of high safety and excellent rate capability.

However, a number of challenges still remain in the development for a new-generation of lithium-ion batteries to meet the emerging applications. Some of the major remaining challenges associated with the existing $Li_4Ti_5O_{12}$ anode materials and olivine $LiFePO_4$ cathode are briefly described below.

(1) Since the improved safety of $Li_4Ti_5O_{12}$ anode is obtained at the expense of energy density due to its high operating voltage vs Li/Li+ (~1.5 V), the lithium-ion battery cells with $Li_4Ti_5O_{12}$ anode offer a low theoretical specific energy due to its low cell voltage. Therefore, lithium-ion batteries with $Li_4Ti_5O_{12}$ anode are more likely to be used in the long term for stationary energy storage and powering HEVs in transportation sector.

(2) Major technical breakthroughs of controllable routes are demanded to create nano-enabled high-quality $Li_4Ti_5O_{12}$ anodes and $LiFePO_4$ cathode materials with improved

electronic and ionic conductivity. The highly effective synthetic combination is always desirable with the optimized approaches such as *in-situ* or *ex-situ* adopted coating or doping methods without compromising safety and cost. A reliable, low-cost, and easily controllable routes to produce high-quality cathode and anode material should be continuously developed.

(3) Nanostructured $Li_4Ti_5O_{12}$ anodes and $LiFePO_4$ cathode, in the form of nanorods, nanowires, and porous clusters, with carbon-coatings have shown very promising performance. However, little is known about the mechanism of elementary steps associated with charge and mass transport in the confined dimensions of $Li_4Ti_5O_{12}$ anode and $LiFePO_4$ cathode (1D, 2D). More sophisticated *in-situ* characterization techniques for probing and mapping these confined $Li_4Ti_5O_{12}$ anode surfaces and $LiFePO_4$ cathode surfaces are needed to gain critical insights into nanoscale phenomena in nano-electrode surfaces during the cycling. The interfacial behavior between electrode and electrolyte strongly influences the cyclability of the nano-LiFePO4 cathode and $Li_4Ti_5O_{12}$ anode, and both modeling and experimental works are needed to investigate this behavior.

(4) The Li-ion cells of $Li_4Ti_5O_{12}/LiFePO_4$ are safe and can support fast charge/discharge rates without degrading the cycling life. Effective combination of $Li_4Ti_5O_{12}$ anode and $LiFePO_4$ cathode is specifically suitable for stationary energy storage in terms of performance and safety. Cost comparison of the combination $Li_4Ti_5O_{12}/LiFePO_4$ electrode materials is also favorable. High rate and long cycling tests based on half-cell or full-cell is expected to attain more effective combination of electrodes of $Li_4Ti_5O_{12}/LiFePO_4$.

(5) It is important to mention that safety considerations are as important as the performance, since a car accident due to the electric vehicle battery safety failure may cause significant damage. On the other hand, high energy density also means high safety risks, and it is the responsibility of the researchers dedicated to this field to ensure that the new lithium-ion batteries meet the safety requirements before they are commercialized in current and future battery markets.

7.3 Future Outlook

As has been demonstrated in the previous Chapters, important future directions and key research efforts of spinel-$Li_4Ti_5O_{12}$ anode and olivine-$LiFePO_4$ cathode behind the developments of high-performance lithium-ion batteries are:

(1) From a scientific point of view, more fundamental studies are needed to fully understand and improve electrochemical performance (i.e. rate-capability, power capacity etc) of $Li_4Ti_5O_{12}$ anode and $LiFePO_4$ cathode using various parameters such as surface area, crystallinity, and the crystalline orientation. In particular, more extensive studies of novel $Li_4Ti_5O_{12}$ and $LiFePO_4$ nano-architectured anode materials are required. One of the strategies is to create 3D $Li_4Ti_5O_{12}$ and $LiFePO_4$ structures combining microscale template and nanostructures to maximize the advantages and minimize the disadvantages of materials at the two scales. Rational design of $Li_4Ti_5O_{12}$ nano-architectured anode and $LiFePO_4$ nano-architectured cathode may lead to higher energy and power densities, significantly enhancing Li-ion battery performance. Eventually, fundamental electrochemical kinetic behaviour (ionic or electronic) needs to be evaluated, and the critical factors of lithium intercalation and extraction (e.g. nanostructure size, phase coating, cation order, doping derivatives, specific morphology, coating composition, and mixed valence conduction) need to be investigated systematically. There remain plenty of opportunities for tailoring the architecture and morphology to obtain more desirable properties.

(2) From a practical point of view, precursor materials availability and cost, cost-effective synthesis, improved service life and safety, and minimal environmental impact are equally important as performance. These features must be in the right balance to achieve the desired battery energy/power density and enhanced charge/discharge rate capability. From the previous discussion mentioned on the above Chapters, one of the best methods to improve the power performance of both $Li_4Ti_5O_{12}$ anode and $LiFePO_4$ cathode is to increase its electronic conductivity by an effective hybrid-surface-coating. Such a nano-hybrid-coating of $Li_4Ti_5O_{12}$ anode and $LiFePO_4$ cathode has played an important role in improving its electrochemical performance. Further work is needed to ensure that the batteries can

withstand operation at the high and low temperatures required by EVs or HEVs. Systematic studies on the mechanism of lithium insertion/extraction of different operating temperatures are helpful for a better fundamental understanding of the relationship between the structure and electrochemical characteristics.

The development of large-scale and low-cost fabrication strategies for $Li_4Ti_5O_{12}$ anode and $LiFePO_4$ cathode materials with desirable performance is a major challenge in the fabrication of battery materials for wide-spread commercial applications. Considering its promise in the design of the new generation of lithium-ion batteries, without doubt, graphene-$Li_4Ti_5O_{12}$ hybrid and graphene-$LiFePO_4$ cathode nanocomposite has potentially shown a very promising and competitive candidate material. It can be anticipated to be used for the next generation of green and sustainable lithium-ion battery system due to its super electrochemical performance.

Publications of Research Outcomes

Journals Publications and Book Chapter

- Xiangcheng Sun, Pavle V. Radovanovic and Bo Cui, "Advances in Spinel $Li_4Ti_5O_{12}$ Anode Materials for Lithium-ion Batteries", New Journal of Chemistry, 2015, Vol. 39 (1), pp.38-63, (Inside Front Cover).
- Xiangcheng Sun, Yuefei. Zhang, Lin Gu, Lilei Hu, Kun Feng, Zongwei Chen, and Bo Cui, "Nanocomposite of TiO_2 Nanoparticles-Reduce Graphene Oxide with High-Rate Performance for Li-Ion Battery", ECS Transactions , 2014, Vol. 64(9), in press.
- Xiangcheng Sun and Bo Cui, "Nano-sized Carbon-coated $Li_4Ti_5O_{12}$ Anode with Enhanced High-Rate Performance for Lithium-ion Battery", Advances in Chemistry Research, Nova Science Publishers, Inc, 2015, Vol. 24, in press (Book Chapter).
- Xiangcheng Sun, M. Hegde, Yuefei Zhang, Min He, Lin Gu, Yongqing Wang, Jie Shu, P. V. Radovanovic, and Bo Cui "Structures and Electrochemical Studies of Spinel $Li_4Ti_5O_{12}$ Nanocomposite Anode for Advanced Lithium Ion Battery". International Journal of Electrochemical Science, 2014, Vol. 9, pp.1583-1596.
- Xiangcheng Sun, M. Hegde, Jian Wang, Yuefei Zhang, Jinyun Liao, P. V. Radovanovic, and Bo Cui "Structural Analysis and Electrochemical Studies of Carbon-Coated $Li_4Ti_5O_{12}$ Particles Used as Anode for Lithium Ion Battery". ECS Transactions, 2014, Vol. 58 (14), pp.79-88
- Xiangcheng Sun, Kai Sun, Yongqing Wang, Xuedong Bai and Bo Cui "Scale-up synthesis, Structure Characterization and Electrochemical Characteristics of C-$LiFePO_4$ Nanocomposites for Lithium Ion Rechargeable Batteries". International Journal of Electrochemical Science, 2013, Vol. 8, pp.12816-12836.
- Xiangcheng Sun, Kai Sun, Caiyun Chen, Haiping Sun and Bo Cui "Controlled Preparation and Surface Structure Characterization of Carbon-$LiFePO_4$ cathode and Electrochemical Studies as Cathode Materials for Li-Ion Battery". International Journal of Materials and Chemistry, 2012, Vol. 2(5), pp.218-224.

Conference Proceedings

- Xiangcheng Sun, Kai Sun, and Bo Cui (2012), "Surface Structure Characterization and Electrochemical Characteristics of Carbon-Coated Lithium Iron Phosphate (C-$LiFePO_4$) Particles". MRS Online Proceedings Library, 1388, mrsf11-1388-f04-09 doi:10.1557/opl.2012.719.
- Xiangcheng Sun, A. Iqbal, I. D. Hosein, M. J. Yacaman, Z. Y. Tang, P. V. Radovanovic and Bo Cui (2012), "Structure Characterization and Electrochemical Characteristics of Carbon Nanotube-Spinel $Li_4Ti_5O_{12}$ Nanoparticles". MRS Online Proceedings Library, 1440, mrss12-1440-o09-34 doi:10.1557/opl.2012.1411.
- Xiangcheng Sun, Xuedong Bai, Yongqing Wang, M. Hegde, I. D. Hosein, P. V. Radovanovic, Yuguo Guo and Bo Cui (2013), "Comparison of Structural Analysis and

Electrochemical Studies of C-$Li_4Ti_5O_{12}$ and CNT-$Li_4Ti_5O_{12}$ Nanocomposites particles used as Anode for Lithium Ion Battery". MRS Online Proceedings Library, 1541, mrss13-1541-f09-01 doi:10.1557/opl.2013.757.

- Xiangcheng Sun and Bo Cui (2014), "Carbon-coated Spinel $Li_4Ti_5O_{12}$ Nanoparticles as an effect Anode for Lithium Ion Battery", Proceedings of 2014 IEEE 14th International Conference on Nanotechnology (IEEE-Nano 14'), 2014.

Papers Under Preparations

- Xiangcheng Sun, Jian Wang, Hegde Manu, Kai Sun, Lin Gu, Jinyun Liao, Yuefei Zhang, P. V. Radovanovic, and Bo Cui, "Facile In-Situ Synthesis of Nano-sized Carbon-Coated $Li_4Ti_5O_{12}$ Particles with Enhanced High-Rate Performance as Anode for Lithium-ion Battery", will submit to ACS Sustainable Chemistry and Engineering.
- Xiangcheng Sun, Yuefei Zhang, Kai Sun, Jun He, Si Xiao and Bo Cui, "Graphene-modified $LiFePO_4$ nanocomposite cathode with hierarchical nano-architectures for high-performance lithium-ion batteries", will submit to ACS Applied Materials & Interface.

Conference Presentations

- Xiangcheng Sun, and Bo Cui, Structure characterizations and electrochemical studies of carbon-coated $LiFePO_4$ cathode materials", Nano-Ontario Conference and Workshop, October 14-15, McMaster University, Hamilton, Ontario, 2011.
- Xiangcheng Sun and Bo Cui, "Scale-up synthesis, Structure characterizations and Electrochemical characteristics of carbon-coated $LiFePO_4$ cathode materials", KAUST-U of T Symposium: Nanomaterials for Energy, University of Toronto, September 28-30, Ontario, 2011
- Xiangcheng Sun, Kai Sun, and Bo Cui, "Surface Structure Characterization and Electrochemical Characteristics of Carbon-Coated Lithium Iron Phosphate (C-$LiFePO_4$) Particles", 2011 Spring MRS meetings, April 25-29, San Francisco, CA, USA 2011.
- Xiangcheng Sun, A. Iqbal, I. D. Hosein, M. J. Yacaman, P. V. Radovanovic, and Bo Cui, "Structure Characterization and Electrochemical Characteristics of Carbon Nanotube-Spinel $Li_4Ti_5O_{12}$ Nanoparticles", 2012 Spring MRS meetings, April 4-13, San Francisco, USA 2012.
- Xiangcheng Sun and Bo Cui, "Structure Characterization and Electrochemical Characteristics of Carbon Nanotube-Spinel $Li_4Ti_5O_{12}$ Nanoparticles", Nano-Ontario Conference and Workshop, October 11-12, University of Waterloo, Waterloo, Ontario, 2012.
- Xiangcheng Sun and Bo Cui, "Structural Analysis and Electrochemical Studies of Carbon-$Li_4Ti_5O_{12}$ Nanocomposites Particles used as Anode for Lithium Ion Battery", 224th ECS Meeting, October 27 – November 1, San Francisco, USA 2013.
- Xiangcheng Sun, Min He, Lin Gu, and Bo Cui, "Preparation, Structural and Electrochemical Studies of Carbon Coated Spinel $Li_4Ti_5O_{12}$ Nanocomposites Used As

Anode for Lithium Ion Battery", 2014 MRS Spring Meeting, April 21-25, San Francisco, California, USA 2014.

- Xiangcheng Sun and Bo Cui, "Carbon-coated Spinel $Li_4Ti_5O_{12}$ Nanoparticles as an effect Anode for Lithium Ion Battery", 2014th IEEE International Conference on Nanotechnology. August 18-21, 2014, Toronto, Canada 2014.
- Xiangcheng Sun and Bo Cui, "Nanocomposites of TiO_2 Nanoparticles-Graphene with High-Rate Performance for Li-Ion Battery", 226th International Electrochemical Society's Meeting, October 5-10, Cancun, Mexico 2014.
- Xiangcheng Sun and Bo Cui, "Carbon-coated $Li_4Ti_5O_{12}$ Nanoparticles Anode for Lithium Ion Battery", 2014-64th Canadian Chemical Engineering Conference, October 19-22, Niagara Falls, Ontario 2014.

References

1. Cheng, F.; Liang, J.; Tao, Z.; Chen, J., Functional materials for rechargeable batteries. *Advanced Materials* **2011,** *23* (15), 1695-1715.
2. Linden, D.; Reddy, T., Handbook of Batteries, **2002**, McGraw-Hill.
3. Tarascon, J.-M.; Armand, M., Issues and challenges facing rechargeable lithium batteries. *Nature* **2001,** *414* (6861), 359-367.
4. Bruce, P. G.; Scrosati, B.; Tarascon, J. M., Nanomaterialien für wiederaufladbare Lithiumbatterien. *Angewandte Chemie* **2008,** *120* (16), 2972-2989.
5. Song, J. Y.; Wang, Y. Y.; Wan, C. C., Review of gel-type polymer electrolytes for lithium-ion batteries. *Journal of Power Sources* **1999,** *77* (2), 183-197.
6. Patil, A.; Patil, V.; Wook Shin, D.; Choi, J. W.; Paik, D. S.; Yoon, S. J., Issue and challenges facing rechargeable thin film lithium batteries. *Materials Research Bulletin* **2008,** *43* (8-9), 1913-1942.
7. Whittingham, M. S., Materials challenges facing electrical energy storage. *MRS Bulletin* **2008,** *33* (04), 411-419.
8. Goodenough, J. B.; Kim, Y., Challenges for rechargeable Li batteries. *Chemistry of Materials* **2009,** *22* (3), 587-603.
9. Winter, M.; Brodd, R. J., What are batteries, fuel cells, and supercapacitors? *Chemical Reviews* **2004,** *104* (10), 4245-4270.
10. Wakihara, M., Recent developments in lithium ion batteries. *Materials Science and Engineering: R: Reports* **2001,** *33* (4), 109-134.
11. Xu, B.; Qian, D.; Wang, Z.; Meng, Y. S., Recent progress in cathode materials research for advanced lithium ion batteries. *Materials Science and Engineering: R: Reports* **2012,** *73* (5–6), 51-65.
12. Dunn, B.; Kamath, H.; Tarascon, J.-M., Electrical Energy Storage for the Grid: A Battery of Choices. *Science* **2011,** *334* (6058), 928-935.
13. Scrosati, B.; Garche, J., Lithium batteries: Status, prospects and future. *Journal of Power Sources* **2010,** *195* (9), 2419-2430.
14. Whittingham, M. S., Lithium batteries and cathode materials. *Chemical Reviews* **2004,** *104* (10), 4271-4302.
15. Ohzuku, T.; Brodd, R. J., An overview of positive-electrode materials for advanced lithium-ion batteries. *Journal of Power Sources* **2007,** *174* (2), 449-456.
16. Ji, L.; Lin, Z.; Alcoutlabi, M.; Zhang, X., Recent developments in nanostructured anode materials for rechargeable lithium-ion batteries. *Energy & Environmental Science* **2011,** *4* (8), 2682.
17. Wang, Y.; Li, H.; He, P.; Hosono, E.; Zhou, H., Nano active materials for lithium-ion batteries. *Nanoscale* **2010,** *2* (8), 1294-1305.
18. Bragg, W. L. In *The diffraction of short electromagnetic waves by a crystal*, Proceedings of the Cambridge Philosophical Society, **1913**; p 4.
19. West, A., Basic Solid State Chemistry, **1999**. Wiley: New York.
20. Williams, D.B., and Carter, C.B., Transmission electron microscopy: a textbook for

materials science. New York, Spinger, **2009**.
21. Rayleigh, L., On the theory of optical images, with special reference to the microscope. *Philosophical Magazine Series 5*, **1896,** *42*, 167-195.
22. http://www.microscopy.ethz.ch. Electron Microsocopy ETH Zürich, Switzerland.
23. Muller, D. A., Structure and bonding at the atomic scale by scanning transmission electron microscopy. *Nature Materials*, **2009**, *8*, 263-270.
24. Egerton, R. F., *Electron energy-loss spectroscopy in the electron microscope*. Springer: **1996**; Vol. 233.
25. Siegbahn, K.; Nordling, C., ESCA, atomic, molecular and solid state structure studied by means of electron spectroscopy. *Nov. Act. Uppsaliensis* **1967**.
26. D. Briggs, and M. P. Seah, *Practical surface analysis by Auger and X-ray photoelectron spectroscopy*. John Wiley & Sons, Chichester: **1983**, 533.
27. Sham, T.-K., *Chemical Applications of Synchrotron Radiation, Part I: Dynamics and Vuv Spectroscopy; Part Ii: X-Ray Applications*. World Scientific: **2002**.
28. Stöhr, J., *NEXAFS spectroscopy*. Springer: **1992**; Vol. 25.
29. Zhang, H.; Wang, J.; Pan, X.; Hu, Y.; Bao, X., Local structure of titania decorated double-walled carbon nanotube characterized by scanning transmission X-ray microscopy. *The Journal of Chemical Physics* **2012,** *136* (17), 174701.
30. Farges, F.; Brown, G. E.; Rehr, J., Ti K-edge XANES studies of Ti coordination and disorder in oxide compounds: Comparison between theory and experiment. *Physical Review B* **1997,** *56* (4), 1809.
31. Wang, J., *Analytical Electrochemistry*. John Wiley & Sons: **2006**.
32. Churikov, A.; Pridatko, K.; Ivanishchev, A.; Ivanishcheva, I.; Gamayunova, I.; Zapsis, K.; Sycheva, V., Impedance spectroscopy of lithium-tin film electrodes. *Russian Journal of Electrochemistry* **2008,** *44* (5), 550-557.
33. Liu, H.; Li, C.; Zhang, H. P.; Fu, L. J.; Wu, Y. P.; Wu, H. Q., Kinetic study on $LiFePO_4$/C nanocomposites synthesized by solid state technique. *Journal of Power Sources* **2006,** *159* (1), 717-720.
34. Xia, H.; Lu, L.; Ceder, G., Li diffusion in $LiCoO_2$ thin films prepared by pulsed laser deposition. *Journal of Power Sources* **2006,** *159* (2), 1422-1427.
35. Barsoukov, E.; Macdonald, J. R., *Impedance spectroscopy: theory, experiment, and applications*. John Wiley & Sons: **2005**.
36. Mizushima, K.; Jones, P.; Wiseman, P.; Goodenough, J., Li_xCoO_2 (0< x<-1): A new cathode material for batteries of high energy density. *Materials Research Bulletin* **1980,** *15* (6), 783-789.
37. Cheng, F.; Tao, Z.; Liang, J.; Chen, J., template-directed materials for rechargeable lithium-ion batteries. *Chemistry of Materials* **2007,** *20* (3), 667-681.
38. Ellis, B. L.; Lee, K. T.; Nazar, L. F., Positive Electrode Materials for Li-Ion and Li-Batteries. *Chemistry of Materials* **2010,** *22* (3), 691-714.
39. Shao-Horn, Y.; Croguennec, L.; Delmas, C.; Nelson, E. C.; O'Keefe, M. A., Atomic resolution of lithium ions in $LiCoO_2$. *Nature Materials* **2003,** *2* (7), 464-467.

40. Reimers, J. N.; Dahn, J., Electrochemical and In Situ X-Ray Diffraction Studies of Lithium Intercalation in Li_xCoO_2. *Journal of The Electrochemical Society* **1992,** *139* (8), 2091-2097.
41. Zou, M.; Yoshio, M.; Gopukumar, S.; Yamaki, J.-i., Synthesis and Electrochemical Performance of High Voltage Cycling $LiM_{0.05}Co_{0.95}O_2$ as Cathode Material for Lithium Rechargeable Cells. *Electrochemical and solid-state letters* **2004,** *7* (7), A176-A179.
42. Ohzuku, T.; Ueda, A., Solid-State Redox Reactions of $LiCoO_2$ ($R\bar{3}m$) for 4 Volt Secondary Lithium Cells. *Journal of The Electrochemical Society* **1994,** *141* (11), 2972-2977.
43. Takahashi, Y.; Tode, S.; Kinoshita, A.; Fujimoto, H.; Nakane, I.; Fujitani, S., Development of lithium-ion batteries with a $LiCoO_2$ cathode toward high capacity by elevating charging potential. *Journal of the Electrochemical Society* **2008,** *155* (7), A537-A541.
44. Fergus, J. W., Recent developments in cathode materials for lithium ion batteries. *Journal of Power Sources* **2010,** *195* (4), 939-954.
45. Amatucci, G.; Tarascon, J.; Klein, L., Cobalt dissolution in $LiCoO_2$-based non-aqueous rechargeable batteries. *Solid State Ionics* **1996,** *83* (1), 167-173.
46. Tukamoto, H.; West, A., Electronic conductivity of $LiCoO_2$ and its enhancement by magnesium doping. *Journal of The Electrochemical Society* **1997,** *144* (9), 3164-3168.
47. Levasseur, S.; Ménétrier, M.; Delmas, C., On the $Li_xCo_{1-y}Mg_yO_2$ system upon deintercalation: electrochemical, electronic properties and Li MAS NMR studies. *Journal of Power Sources* **2002,** *112* (2), 419-427.
48. Delmas, C.; Saadoune, I., Electrochemical and physical properties of the $Li_xNi_{1-y}Co_yO_2$ phases. *Solid State Ionics* **1992,** *53*, 370-375.
49. Saadoune, I.; Delmas, C., $LiNi_{1-x}CoO_2$ positive electrode materials: relationships between the structure, physical properties and electrochemical behaviour. *Journal of Materials Chemistry* **1996,** *6* (2), 193-199.
50. Ohzuku, T.; Ueda, A., Phenomenological Expression of Solid-State Redox Potentials of $LiCoO_2$, $LiCo_{1/2}Ni_{1/2}O_2$, and $LiNiO_2$ Insertion Electrodes. *Journal of The Electrochemical Society* **1997,** *144* (8), 2780-2785.
51. Cho, J.; Kim, G.; Lim, H. S., Effect of Preparation Methods of $LiNi_{1-x}C_xO_2$ Cathode Materials on Their Chemical Structure and Electrode Performance. *Journal of The Electrochemical Society* **1999,** *146* (10), 3571-3576.
52. Stoyanova, R.; Zhecheva, E.; Zarkova, L., Effect of Mn-substitution for Co on the crystal structure and acid delithiation of $LiMn_yCo_{1-y}O_2$ solid solutions. *Solid State Ionics* **1994,** *73* (3), 233-240.
53. Armstrong, A. R.; Robertson, A. D.; Gitzendanner, R.; Bruce, P. G., The Layered Intercalation Compounds Li ($Mn_{1-y}Co_yO_2$): Positive Electrode Materials for Lithium–Ion Batteries. *Journal of Solid State Chemistry* **1999,** *145* (2), 549-556.

54. Zou, M.; Yoshio, M.; Gopukumar, S.; Yamaki, J.I., Synthesis of high-voltage (4.5 V) cycling doped $LiCoO_2$ for use in lithium rechargeable cells. *Chemistry of Materials* **2003,** *15* (25), 4699-4702.
55. Zou, M.; Yoshio, M.; Gopukumar, S.; Yamaki, J. I., Performance of $LiM_{0.05}Co_{0.95}O_2$ Cathode Materials in Lithium Rechargeable Cells When Cycled up to 4.5 V. *Chemistry of Materials* **2005,** *17* (6), 1284-1286.
56. Cho, J.; Kim, Y. J.; Park, B., $LiCoO_2$ cathode material that does not show a phase transition from hexagonal to monoclinic phase. *Journal of The Electrochemical Society* **2001,** *148* (10), A1110-A1115.
57. Cho, J.; Kim, Y. J.; Park, B., Novel $LiCoO_2$ cathode material with Al_2O_3 coating for a Li ion cell. *Chemistry of Materials* **2000,** *12* (12), 3788-3791.
58. Manthiram, A., Materials challenges and opportunities of lithium ion batteries. *The Journal of Physical Chemistry Letters* **2011,** *2* (3), 176-184.
59. Wang, J.; Sun, X., Understanding and recent development of carbon coating on $LiFePO_4$ cathode materials for lithium-ion batteries. *Energy & Environmental Science* **2012,** *5* (1), 5163-5185.
60. Park, O. K.; Cho, Y.; Lee, S.; Yoo, H.-C.; Song, H.-K.; Cho, J., Who will drive electric vehicles, olivine or spinel? *Energy & Environmental Science* **2011,** *4* (5), 1621-1633.
61. Jeong, G.; Kim, Y.-U.; Kim, H.; Kim, Y.-J.; Sohn, H.-J., Prospective materials and applications for Li secondary batteries. *Energy & Environmental Science* **2011,** *4* (6), 1986-2002.
62. Padhi, A. K.; Nanjundaswamy, K.; Goodenough, J. B. d., Phospho-olivines as positive-electrode materials for rechargeable lithium batteries. *Journal of the Electrochemical Society* **1997,** *144* (4), 1188-1194.
63. Goodenough, J. B.; Masquelier, C.; Nanjundaswamy, K.; Padhi, A. K., Cathode materials for secondary (rechargeable) lithium batteries. Google Patents: **1999**.
64. Armand, M.; Goodenough, J. B.; Padhi, A. K.; Nanjundaswamy, K. S.; Masquelier, C., Cathode materials for secondary (rechargeable) lithium batteries. Google Patents: **2003**.
65. Yuan, L.-X.; Wang, Z.-H.; Zhang, W.-X.; Hu, X.-L.; Chen, J.-T.; Huang, Y.-H.; Goodenough, J. B., Development and challenges of $LiFePO_4$ cathode material for lithium-ion batteries. *Energy & Environmental Science* **2011,** *4* (2), 269-284.
66. Wang, Y.; He, P.; Zhou, H., Olivine $LiFePO_4$: development and future. *Energy & Environmental Science* **2011,** *4* (3), 805-817.
67. Cho, Y.-D.; Fey, G. T.-K.; Kao, H.-M., The effect of carbon coating thickness on the capacity of $LiFePO_4$/C composite cathodes. *Journal of Power Sources* **2009,** *189* (1), 256-262.
68. Goodenough, J. B.; Kim, Y., Challenges for Rechargeable Li Batteries. *Chemistry of Materials* **2010,** *22* (3), 587-603.

69. Yi, T.-F.; Li, X.-Y.; Liu, H.; Shu, J.; Zhu, Y.-R.; Zhu, R.-S., Recent developments in the doping and surface modification of $LiFePO_4$ as cathode material for power lithium ion battery. *Ionics* **2012,** *18* (6), 529-539.
70. Okada, S.; Sawa, S.; Egashira, M.; Yamaki, J. I.; Tabuchi, M.; Kageyama, H.; Konishi, T.; Yoshino, A., Cathode properties of phospho-olivine $LiMPO_4$ for lithium secondary batteries. *Journal of Power Sources* **2001,** *97–98* (0), 430-432.
71. Chung, S.-Y.; Bloking, J. T.; Chiang, Y.-M., Electronically conductive phospho-olivines as lithium storage electrodes. *Nature Materials* **2002,** *1* (2), 123-128.
72. Molenda, J.; Stokłosa, A.; Bąk, T., Modification in the electronic structure of cobalt bronze Li_xCoO_2 and the resulting electrochemical properties. *Solid State Ionics* **1989,** *36* (1–2), 53-58.
73. Islam, M. S.; Driscoll, D. J.; Fisher, C. A.; Slater, P. R., Atomic-scale investigation of defects, dopants, and lithium transport in the $LiFePO_4$ olivine-type battery material. *Chemistry of Materials* **2005,** *17* (20), 5085-5092.
74. Fang, H.; Pan, Z.; Li, L.; Yang, Y.; Yan, G.; Li, G.; Wei, S., The possibility of manganese disorder in $LiMnPO_4$ and its effect on the electrochemical activity. *Electrochemistry Communications* **2008,** *10* (7), 1071-1073.
75. Xie, J.; Imanishi, N.; Zhang, T.; Hirano, A.; Takeda, Y.; Yamamoto, O., Li-ion diffusion kinetics in $LiFePO_4$ thin film prepared by radio frequency magnetron sputtering. *Electrochimica Acta* **2009,** *54* (20), 4631-4637.
76. Srinivasan, V.; Newman, J., Existence of Path-Dependence in the $LiFePO_4$ Electrode. *Electrochemical and Solid-State Letters* **2006,** *9* (3), A110-A114.
77. Delmas, C.; Maccario, M.; Croguennec, L.; Le Cras, F.; Weill, F., Lithium deintercalation in $LiFePO_4$ nanoparticles via a domino-cascade model. *Nature Materials* **2008,** *7* (8), 665-671.
78. Delacourt, C.; Poizot, P.; Tarascon, J.-M.; Masquelier, C., The existence of a temperature-driven solid solution in Li_xFePO_4 for $0 \leq x \leq 1$. *Nature Materials* **2005,** *4* (3), 254-260.
79. Yang, S.; Song, Y.; Ngala, K.; Zavalij, P. Y.; Stanley Whittingham, M., Performance of $LiFePO_4$ as lithium battery cathode and comparison with manganese and vanadium oxides. *Journal of Power Sources* **2003,** *119-121* (0), 239-246.
80. Delacourt, C.; Poizot, P.; Levasseur, S.; Masquelier, C., Size Effects on Carbon-Free $LiFePO_4$ Powders: The Key to Superior Energy Density. *Electrochemical and Solid-State Letters* **2006,** *9* (7), A352-A355.
81. Kang, B.; Ceder, G., Battery materials for ultrafast charging and discharging. *Nature* **2009,** *458* (7235), 190-193.
82. Fey, G. T.-K.; Chen, Y. G.; Kao, H.-M., Electrochemical properties of $LiFePO_4$ prepared via ball-milling. *Journal of Power Sources* **2009,** *189* (1), 169-178.
83. Kim, D.-H.; Kim, J., Synthesis of $LiFePO_4$ nanoparticles in polyol medium and their electrochemical properties. *Electrochemical and Solid-State Letters* **2006,** *9* (9), A439-A442.

84. Zhang, W. J., Comparison of the rate capacities of $LiFePO_4$ cathode materials. *Journal of The Electrochemical Society* **2010,** *157* (10), A1040-A1046.
85. Zhang, W. J., Structure and performance of $LiFePO_4$ cathode materials: A review. *Journal of Power Sources* **2011,** *196* (6), 2962-2970.
86. Huang, H.; Yin, S.-C.; Nazar, L. S., Approaching theoretical capacity of $LiFePO_4$ at room temperature at high rates. *Electrochemical and Solid-State Letters* **2001,** *4* (10), A170-A172.
87. Kim, J.-K.; Cheruvally, G.; Ahn, J.-H.; Hwang, G.-C.; Choi, J.-B., Electrochemical properties of carbon-coated LiFePO4 synthesized by a modified mechanical activation process. *Journal of Physics and Chemistry of Solids* **2008,** *69* (10), 2371-2377.
88. Kadoma, Y.; Kim, J.-M.; Abiko, K.; Ohtsuki, K.; Ui, K.; Kumagai, N., Optimization of electrochemical properties of $LiFePO_4$/C prepared by an aqueous solution method using sucrose. *Electrochimica Acta* **2010,** *55* (3), 1034-1041.
89. Ding, Y.; Jiang, Y.; Xu, F.; Yin, J.; Ren, H.; Zhuo, Q.; Long, Z.; Zhang, P., Preparation of nano-structured $LiFePO_4$/graphene composites by co-precipitation method. *Electrochemistry Communications* **2010,** *12* (1), 10-13.
90. Sanchez, M. A. E.; Brito, G. E. S.; Fantini, M. C. A.; Goya, G. F.; Matos, J. R., Synthesis and characterization of $LiFePO_4$ prepared by sol–gel technique. *Solid State Ionics* **2006,** *177* (5–6), 497-500.
91. Lin, Y.; Gao, M. X.; Zhu, D.; Liu, Y. F.; Pan, H. G., Effects of carbon coating and iron phosphides on the electrochemical properties of $LiFePO_4$/C. *Journal of Power Sources* **2008,** *184* (2), 444-448.
92. Wang, K.; Cai, R.; Yuan, T.; Yu, X.; Ran, R.; Shao, Z., Process investigation, electrochemical characterization and optimization of $LiFePO_4$/C composite from mechanical activation using sucrose as carbon source. *Electrochimica Acta* **2009,** *54* (10), 2861-2868.
93. Hu, G. R.; Gao, X. G.; Peng, Z. D.; Du, K.; Liu, Y. J., Synthetic $LiFePO_4$/C without using inert gas. *Chinese Chemical Letters* **2007,** *18* (3), 337-340.
94. Doeff, M. M.; Wilcox, J. D.; Kostecki, R.; Lau, G., Optimization of carbon coatings on $LiFePO_4$. *Journal of Power Sources* **2006,** *163* (1), 180-184.
95. Chen, Z.; Dahn, J. R., Reducing Carbon in $LiFePO_4$/C Composite Electrodes to Maximize Specific Energy, Volumetric Energy, and Tap Density. *Journal of The Electrochemical Society* **2002,** *149* (9), A1184-A1189.
96. Yang, S. T.; Zhao, N. H.; Dong, H. Y.; Yang, J. X.; Yue, H. Y., Synthesis and characterization of $LiFePO_4$ cathode material dispersed with nano-structured carbon. *Electrochimica Acta* **2005,** *51* (1), 166-171.
97. Shin, H. C.; Cho, W. I.; Jang, H., Electrochemical properties of carbon-coated $LiFePO_4$ cathode using graphite, carbon black, and acetylene black. *Electrochimica Acta* **2006,** *52* (4), 1472-1476.
98. Kim, K.; Jeong, J. H.; Kim, I.-J.; Kim, H.-S., Carbon coatings with olive oil, soybean oil and butter on nano-$LiFePO_4$. *Journal of Power Sources* **2007,** *167* (2), 524-528.

99. Liang, G.; Wang, L.; Ou, X.; Zhao, X.; Xu, S., Lithium iron phosphate with high-rate capability synthesized through hydrothermal reaction in glucose solution. *Journal of Power Sources* **2008,** *184* (2), 538-542.
100. Lai, C.; Xu, Q.; Ge, H.; Zhou, G.; Xie, J., Improved electrochemical performance of $LiFePO_4$/C for lithium-ion batteries with two kinds of carbon sources. *Solid State Ionics* **2008,** *179* (27–32), 1736-1739.
101. Vadivel Murugan, A.; Muraliganth, T.; Manthiram, A., One-Pot Microwave-Hydrothermal Synthesis and Characterization of Carbon-Coated $LiMPO_4$ (M = Mn , Fe, and Co) Cathodes. *Journal of The Electrochemical Society* **2009,** *156* (2), A79-A83.
102. Wang, S.; Zhou, C.; Zhou, Q.; Ni, G.; Wu, J., Preparation of $LiFePO_4$/C in a reductive atmosphere generated by windward aerobic decomposition of glucose. *Journal of Power Sources* **2011,** *196* (11), 5143-5146.
103. Doeff, M. M.; Hu, Y.; McLarnon, F.; Kostecki, R., Effect of Surface Carbon Structure on the Electrochemical Performance of $LiFePO_4$. *Electrochemical and Solid-State Letters* **2003,** *6* (10), A207-A209.
104. Wang, G. X.; Needham, S.; Yao, J.; Wang, J. Z.; Liu, R. S.; Liu, H. K., A study on $LiFePO_4$ and its doped derivatives as cathode materials for lithium-ion batteries. *Journal of Power Sources* **2006,** *159* (1), 282-286.
105. Ying, J.; Lei, M.; Jiang, C.; Wan, C.; He, X.; Li, J.; Wang, L.; Ren, J., Preparation and characterization of high-density spherical $Li_{0.97}Cr_{0.01}PO_4$/C cathode material for lithium ion batteries. *Journal of Power Sources* **2006,** *158* (1), 543-549.
106. Roberts, M. R.; Vitins, G.; Owen, J. R., High-throughput studies of $Li_{1-x}Mg_{x/2}FePO_4$ and $LiFe_{1-y}Mg_yPO_4$ and the effect of carbon coating. *Journal of Power Sources* **2008,** *179* (2), 754-762.
107. Wang, D.; Li, H.; Shi, S.; Huang, X.; Chen, L., Improving the rate performance of $LiFePO_4$ by Fe-site doping. *Electrochimica Acta* **2005,** *50* (14), 2955-2958.
108. Wang, G. X.; Bewlay, S. L.; Konstantinov, K.; Liu, H. K.; Dou, S. X.; Ahn, J. H., Physical and electrochemical properties of doped lithium iron phosphate electrodes. *Electrochimica Acta* **2004,** *50* (2–3), 443-447.
109. Teng, T.-H.; Yang, M.-R.; Wu, S.-h.; Chiang, Y.-P., Electrochemical properties of $LiFe_{0.9}Mg_{0.1}PO_4$/carbon cathode materials prepared by ultrasonic spray pyrolysis. *Solid State Communications* **2007,** *142* (7), 389-392.
110. Sun, C. S.; Zhang, Y.; Zhang, X. J.; Zhou, Z., Structural and electrochemical properties of Cl-doped $LiFePO_4$/C. *Journal of Power Sources* **2010,** *195* (11), 3680-3683.
111. Shin, H. C.; Park, S. B.; Jang, H.; Chung, K. Y.; Cho, W. I.; Kim, C. S.; Cho, B. W., Rate performance and structural change of Cr-doped $LiFePO_4$/C during cycling. *Electrochimica Acta* **2008,** *53* (27), 7946-7951.
112. Liao, X.-Z.; He, Y.-S.; Ma, Z.-F.; Zhang, X.-M.; Wang, L., Effects of fluorine-substitution on the electrochemical behavior of $LiFePO_4$/C cathode materials. *Journal of Power Sources* **2007,** *174* (2), 720-725.

113. Lu, F.; Zhou, Y.; Liu, J.; Pan, Y., Enhancement of F-doping on the electrochemical behavior of carbon-coated $LiFePO_4$ nanoparticles prepared by hydrothermal route. *Electrochimica Acta* **2011,** *56* (24), 8833-8838.
114. Ravet, N.; Abouimrane, A.; Armand, M., From our readers: On the electronic conductivity of phospho-olivines as lithium storage electrodes. *Nature Materials* **2003,** *2* (11), 702-702.
115. Herle, P. S.; Ellis, B.; Coombs, N.; Nazar, L., Nano-network electronic conduction in iron and nickel olivine phosphates. *Nature Materials* **2004,** *3* (3), 147-152.
116. Xu, J.; Chen, G., Effects of doping on the electronic properties of $LiFePO_4$: A first-principles investigation. *Physica B: Condensed Matter* **2010,** *405* (3), 803-807.
117. Wagemaker, M.; Ellis, B. L.; Lutzenkirchen-Hecht, D.; Mulder, F. M.; Nazar, L. F., Proof of supervalent doping in olivine $LiFePO_4$. *Chemistry of Materials* **2008,** *20* (20), 6313-6315.
118. Dahn, J. R.; Zheng, T.; Liu, Y.; Xue, J. S., Mechanisms for Lithium Insertion in Carbonaceous Materials. *Science* **1995,** *270* (5236), 590-593.
119. Winter, M.; Besenhard, J. O.; Spahr, M. E.; Novák, P., Insertion Electrode Materials for Rechargeable Lithium Batteries. *Advanced Materials* **1998,** *10* (10), 725-763.
120. Wu, Y. P.; Rahm, E.; Holze, R., Carbon anode materials for lithium ion batteries. *Journal of Power Sources* **2003,** *114* (2), 228-236.
121. Cui, L.-F.; Yang, Y.; Hsu, C.-M.; Cui, Y., Carbon-silicon core-shell nanowires as high capacity electrode for lithium ion batteries. *Nano Letters* **2009,** *9* (9), 3370-3374.
122. Ji, L.; Zhang, X., Manganese oxide nanoparticle-loaded porous carbon nanofibers as anode materials for high-performance lithium-ion batteries. *Electrochemistry Communications* **2009,** *11* (4), 795-798.
123. Lee, K. T.; Lytle, J. C.; Ergang, N. S.; Oh, S. M.; Stein, A., Synthesis and Rate Performance of Monolithic Macroporous Carbon Electrodes for Lithium-Ion Secondary Batteries. *Advanced Functional Materials* **2005,** *15* (4), 547-556.
124. Lee, J.-H.; Kim, W.-J.; Kim, J.-Y.; Lim, S.-H.; Lee, S.-M., Spherical silicon/graphite/carbon composites as anode material for lithium-ion batteries. *Journal of Power Sources* **2008,** *176* (1), 353-358.
125. Boukamp, B. A.; Lesh, G. C.; Huggins, R. A., All-Solid Lithium Electrodes with Mixed-Conductor Matrix. *Journal of The Electrochemical Society* **1981,** *128* (4), 725-729.
126. Ryu, J. H.; Kim, J. W.; Sung, Y.-E.; Oh, S. M., Failure modes of silicon powder negative electrode in lithium secondary batteries. *Electrochemical and solid-state letters* **2004,** *7* (10), A306-A309.
127. Kasavajjula, U.; Wang, C.; Appleby, A., Silicon anodes for Li-ion battery–a review. *Journal of Power Sources* **2007,** *163*, 1003.
128. Guo, Z.; Wang, J.; Liu, H.; Dou, S., Study of silicon/polypyrrole composite as anode materials for Li-ion batteries. *Journal of Power Sources* **2005,** *146* (1), 448-451.

129. Cui, L.-F.; Ruffo, R.; Chan, C. K.; Peng, H.; Cui, Y., Crystalline-amorphous core-shell silicon nanowires for high capacity and high current battery electrodes. *Nano Letters* **2008,** *9* (1), 491-495.
130. Park, M.-H.; Kim, M. G.; Joo, J.; Kim, K.; Kim, J.; Ahn, S.; Cui, Y.; Cho, J., Silicon nanotube battery anodes. *Nano Letters* **2009,** *9* (11), 3844-3847.
131. Beaulieu, L.; Hewitt, K.; Turner, R.; Bonakdarpour, A.; Abdo, A.; Christensen, L.; Eberman, K.; Krause, L.; Dahn, J., The electrochemical reaction of Li with amorphous Si-Sn alloys. *Journal of The Electrochemical Society* **2003,** *150* (2), A149-A156.
132. Yang, X.; Wen, Z.; Huang, S.; Zhu, X.; Zhang, X., Electrochemical performances of silicon electrode with silver additives. *Solid State Ionics* **2006,** *177* (26–32), 2807-2810.
133. Hassoun, J.; Reale, P.; Scrosati, B., Recent advances in liquid and polymer lithium-ion batteries. *Journal of Materials Chemistry* **2007,** *17* (35), 3668-3677.
134. Hassoun, J.; Panero, S.; Scrosati, B., Electrodeposited Ni–Sn intermetallic electrodes for advanced lithium ion batteries. *Journal of Power Sources* **2006,** *160* (2), 1336-1341.
135. Hassoun, J.; Panero, S.; Simon, P.; Taberna, P. L.; Scrosati, B., High-Rate, Long-Life Ni–Sn Nanostructured Electrodes for Lithium-Ion Batteries. *Advanced Materials* **2007,** *19* (12), 1632-1635.
136. Wang, Y.; Lee, J. Y., One-Step, Confined Growth of Bimetallic Tin–Antimony Nanorods in Carbon Nanotubes Grown In Situ for Reversible Li^+ Ion Storage. *Angewandte Chemie International Edition* **2006,** *45* (42), 7039-7042.
137. Ohzuku, T.; Ueda, A.; Yamamoto, N., Zero-Strain Insertion Material of Li $[Li_{1/3}Ti_{5/3}]O_4$ for Rechargeable Lithium Cells. *Journal of the Electrochemical Society* **1995,** *142* (5), 1431-1435.
138. Yi, T.-F.; Jiang, L.-J.; Shu, J.; Yue, C.-B.; Zhu, R.-S.; Qiao, H.-B., Recent development and application of $Li_4Ti_5O_{12}$ as anode material of lithium ion battery. *Journal of Physics and Chemistry of Solids* **2010,** *71* (9), 1236-1242.
139. Zhu, G.-N.; Wang, Y.-G.; Xia, Y.-Y., Ti-based compounds as anode materials for Li-ion batteries. *Energy & Environmental Science* **2012,** *5* (5), 6652.
140. Scharner, S.; Weppner, W.; Schmid-Beurmann, P., Evidence of Two-Phase Formation upon Lithium Insertion into the $Li_{1.33}Ti_{1.67}O_4$ Spinel. *Journal of the Electrochemical Society* **1999,** *146* (3), 857-861.
141. Lu, W.; Belharouak, I.; Liu, J.; Amine, K., Electrochemical and Thermal Investigation of $Li_{4/3}Ti_{5/3}O_4$ Spinel. *Journal of The Electrochemical Society* **2007,** *154* (2), A114-A118.
142. Kavan, L.; Grätzel, M., Facile synthesis of nanocrystalline $Li_4Ti_5O_{12}$ (Spinel) exhibiting fast Li insertion. *Electrochemical and Solid-State Letters* **2002,** *5* (2), A39-A42.
143. Zaghib, K.; Simoneau, M.; Armand, M.; Gauthier, M., Electrochemical study of $Li_4Ti_5O_{12}$ as negative electrode for Li-ion polymer rechargeable batteries. *Journal of Power Sources* **1999,** *81*, 300-305.

144. Shu, J., Electrochemical behavior and stability of $Li_4Ti_5O_{12}$ in a broad voltage window. *Journal of Solid State Electrochemistry* **2009,** *13* (10), 1535-1539.
145. Colin, J.-F.; Godbole, V.; Novák, P., In-situ neutron diffraction study of Li insertion in $Li_4Ti_5O_{12}$. *Electrochemistry Communications* **2010,** *12* (6), 804-807.
146. Takai, S.; Kamata, M.; Fujine, S.; Yoneda, K.; Kanda, K.; Esaka, T., Diffusion coefficient measurement of lithium ion in sintered $Li_{1.33}Ti_{1.67}O_4$ by means of neutron radiography. *Solid State Ionics* **1999,** *123* (1), 165-172.
147. Ma, J.; Wang, C.; Wroblewski, S., Kinetic characteristics of mixed conductive electrodes for lithium ion batteries. *Journal of Power Sources* **2007,** *164* (2), 849-856.
148. Yao, X.; Xie, S.; Nian, H.; Chen, C., Spinel $Li_4Ti_5O_{12}$ as a reversible anode material down to 0V. *Journal of Alloys and Compounds* **2008,** *465* (1), 375-379.
149. Takami, N.; Hoshina, K.; Inagaki, H., Lithium diffusion in $Li_{4/3}Ti_{5/3}O_4$ particles during insertion and extraction. *Journal of the Electrochemical Society* **2011,** *158* (6), A725-A730.
150. Takami, N.; Inagaki, H.; Kishi, T.; Harada, Y.; Fujita, Y.; Hoshina, K., Electrochemical kinetics and safety of 2-volt class Li-ion battery system using lithium titanium oxide anode. *Journal of The Electrochemical Society* **2009,** *156* (2), A128-A132.
151. Liu, D.; Ouyang, C.; Shu, J.; Jiang, J.; Wang, Z.; Chen, L., Theoretical study of cation doping effect on the electronic conductivity of $Li_4Ti_5O_{12}$. P*hysica Status Solidi (b)* **2006,** *243* (8), 1835-1841.
152. Hao, Y.-J.; Lai, Q.-Y.; Lu, J.-Z.; Ji, X.-Y., Effects of dopant on the electrochemical properties of $Li_4Ti_5O_{12}$ anode materials. *Ionics* **2007,** *13* (5), 369-373.
153. Zhong, Z., Synthesis of Mo^{4+} Substituted Spinel $Li_4Ti_{5-x}Mo_xO_{12}$. *Electrochemical and Solid-State Letters* **2007,** *10* (12), A267-A269.
154. Wolfenstine, J.; Allen, J., Electrical conductivity and charge compensation in Ta doped $Li_4Ti_5O_{12}$. *Journal of Power Sources* **2008,** *180* (1), 582-585.
155. Li, X.; Qu, M.; Yu, Z., Structural and electrochemical performances of $Li_4Ti_5O_{12}$ as anode material for lithium-ion batteries. *Journal of Alloys and Compounds* **2009,** *487* (1), L12-L17.
156. Zhang, B.; Du, H.; Li, B.; Kang, F., Structure and electrochemical properties of Zn-doped $Li_4Ti_5O_{12}$ as anode materials in Li-ion battery. *Electrochemical and Solid-State Letters* **2010,** *13* (4), A36-A38.
157. Huang, S.; Wen, Z.; Zhu, X.; Lin , Z., Preparation and Electrochemical Performance of Spinel-Type Compounds $Li_4Al_yTi_{5-y}O_{12}$ ($y = 0$, 0.10, 0.15, 0.25). *Journal of The Electrochemical Society* **2005,** *152* (1), A186-A190.
158. Huang, S.; Wen, Z.; Zhu, X.; Lin, Z., Effects of dopant on the electrochemical performance of $Li_4Ti_5O_{12}$ as electrode material for lithium ion batteries. *Journal of Power Sources* **2007,** *165* (1), 408-412.
159. Liu, H.; Feng, Y.; Wang, K.; Xie, J., Synthesis and electrochemical properties of $Li_4Ti_5O_{12}$/C composite by the PVB rheological phase method. *Journal of Physics and Chemistry of Solids* **2008,** *69* (8), 2037-2040.

160. Yuan, T.; Yu, X.; Cai, R.; Zhou, Y.; Shao, Z., Synthesis of pristine and carbon-coated $Li_4Ti_5O_{12}$ and their low-temperature electrochemical performance. *Journal of Power Sources* **2010,** *195* (15), 4997-5004.
161. Lin, Z.; Hu, X.; Huai, Y.; Liu, L.; Deng, Z.; Suo, J., One-step synthesis of $Li_4Ti_5O_{12}$/C anode material with high performance for lithium-ion batteries. *Solid State Ionics* **2010,** *181* (8), 412-415.
162. Cheng, L.; Li, X.-L.; Liu, H.-J.; Xiong, H.-M.; Zhang, P.-W.; Xia, Y.-Y., Carbon-coated $Li_4Ti_5O_{12}$ as a high rate electrode material for Li-ion intercalation. *Journal of the Electrochemical Society* **2007,** *154* (7), A692-A697.
163. Wang, G. J.; Gao, J.; Fu, L. J.; Zhao, N. H.; Wu, Y. P.; Takamura, T., Preparation and characteristic of carbon-coated $Li_4Ti_5O_{12}$ anode material. *Journal of Power Sources* **2007,** *174* (2), 1109-1112.
164. Gao, J.; Ying, J.; Jiang, C.; Wan, C., High-density spherical $Li_4Ti_5O_{12}$/C anode material with good rate capability for lithium ion batteries. *Journal of Power Sources* **2007,** *166* (1), 255-259.
165. Li, X.; Qu, M.; Yu, Z., Preparation and electrochemical performance of $Li_4Ti_5O_{12}$ /graphitized carbon nanotubes composite. *Solid State Ionics* **2010,** *181* (13), 635-639.
166. Huang, S.; Wen, Z.; Zhu, X.; Gu, Z., Preparation and electrochemical performance of Ag doped $Li_4Ti_5O_{12}$. *Electrochemistry Communications* **2004,** *6* (11), 1093-1097.
167. Huang, S.; Wen, Z.; Zhang, J.; Gu, Z.; Xu, X., $Li_4Ti_5O_{12}$ -Ag composite as electrode materials for lithium-ion battery. *Solid State Ionics* **2006,** *177* (9), 851-855.
168. Hao, Y.-J.; Lai, Q.-Y.; Chen, Y.-D.; Lu, J.-Z.; Ji, X.-Y., In situ deposition method preparation of $Li_4Ti_5O_{12}$–SnO_2 composite materials for lithium ion batteries. *Journal of Alloys and Compounds* **2008,** *462* (1), 404-409.
169. Huang, S.; Wen, Z.; Lin, B.; Han, J.; Xu, X., The high-rate performance of the newly designed $Li_4Ti_5O_{12}$/Cu composite anode for lithium ion batteries. *Journal of Alloys and Compounds* **2008,** *457* (1), 400-403.
170. Thackeray, M., Lithium-ion batteries: An unexpected conductor. *Nature Materials* **2002,** *1* (2), 81-82.
171. Fisher, C. A.; Hart Prieto, V. M.; Islam, M. S., Lithium Battery Materials $LiMPO_4$ (M= Mn, Fe, Co, and Ni): Insights into Defect Association, Transport Mechanisms, and Doping Behavior. *Chemistry of Materials* **2008,** *20* (18), 5907-5915.
172. Thorat, I. V.; Mathur, V.; Wheeler, D. R., Performance of carbon-fiber-containing $LiFePO_4$ cathodes for high-power applications. *Journal of Power Sources* **2006,** *162* (1), 673-678.
173. Tarascon, J.-M.; Recham, N.; Armand, M.; Chotard, J.-N.; Barpanda, P.; Walker, W.; Dupont, L., Hunting for Better Li-Based Electrode Materials via Low Temperature Inorganic Synthesis. *Chemistry of Materials* **2009,** *22* (3), 724-739.
174. Chung, S. Y.; Kim, Y. M.; Choi, S. Y., Direct Physical Imaging and Chemical Probing of $LiFePO_4$ for Lithium-Ion Batteries. *Advanced Functional Materials* **2010,** *20* (24), 4219-4232.

175. Recham, N.; Chotard, J. N.; Dupont, L.; Delacourt, C.; Walker, W.; Armand, M.; Tarascon, J. M., A 3.6V lithium-based fluorosulphate insertion positive electrode for lithium-ion batteries. *Nature Materials* **2010,** *9* (1), 68-74.
176. Fey, G. T.-K.; Lu, T.-L., Morphological characterization of $LiFePO_4$/C composite cathode materials synthesized via a carboxylic acid route. *Journal of Power Sources* **2008,** *178* (2), 807-814.
177. Lu, Z.; Chen, H.; Robert, R.; Zhu, B. Y.; Deng, J.; Wu, L.; Chung, C. Y.; Grey, C. P., Citric acid-and ammonium-mediated morphological transformations of olivine $LiFePO_4$ particles. *Chemistry of Materials* **2011,** *23* (11), 2848-2859.
178. Maccario, M.; Croguennec, L.; Le Cras, F.; Delmas, C., Electrochemical performances in temperature for a C-containing $LiFePO_4$ composite synthesized at high temperature. *Journal of Power Sources* **2008,** *183* (1), 411-417.
179. Lee, K. T.; Cho, J., Roles of nanosize in lithium reactive nanomaterials for lithium ion batteries. *Nano Today* **2011,** *6* (1), 28-41.
180. Yamada, A.; Chung, S.-C.; Hinokuma, K., Optimized $LiFePO_4$ for lithium battery cathodes. *Journal of the Electrochemical Society* **2001,** *148* (3), A224-A229.
181. Piana, M.; Cushing, B. L.; Goodenough, J. B.; Penazzi, N., A new promising sol–gel synthesis of phospho-olivines as environmentally friendly cathode materials for Li-ion cells. *Solid State Ionics* **2004,** *175* (1–4), 233-237.
182. Meligrana, G.; Gerbaldi, C.; Tuel, A.; Bodoardo, S.; Penazzi, N., Hydrothermal synthesis of high surface $LiFePO_4$ powders as cathode for Li-ion cells. *Journal of Power Sources* **2006,** *160* (1), 516-522.
183. Choi, D.; Kumta, P. N., Surfactant based sol–gel approach to nanostructured $LiFePO_4$ for high rate Li-ion batteries. *Journal of Power Sources* **2007,** *163* (2), 1064-1069.
184. Lee, S. B.; Cho, S. H.; Cho, S. J.; Park, G. J.; Park, S. H.; Lee, Y. S., Synthesis of $LiFePO_4$ material with improved cycling performance under harsh conditions. *Electrochemistry Communications* **2008,** *10* (9), 1219-1221.
185. Zheng, J.C.; Li, X.H.; Wang, Z.-X.; Guo, H.J.; Zhou, S.Y., $LiFePO_4$ with enhanced performance synthesized by a novel synthetic route. *Journal of Power Sources* **2008,** *184* (2), 574-577.
186. Wang, Y.; Wang, Y.; Hosono, E.; Wang, K.; Zhou, H., The Design of a $LiFePO_4$/Carbon Nanocomposite With a Core-Shell Structure and Its Synthesis by an In Situ Polymerization Restriction Method. *Angewandte Chemie International Edition* **2008,** *47* (39), 7461-7465.
187. Yang, M.-R.; Ke, W.-H.; Wu, S.-H., Preparation of $LiFePO_4$ powders by co-precipitation. *Journal of Power Sources* **2005,** *146* (1–2), 539-543.
188. Xu, Y.; Lu, Y.; Yan, L.; Yang, Z.; Yang, R., Synthesis and effect of forming Fe_2P phase on the physics and electrochemical properties of $LiFePO_4$/C materials. *Journal of Power Sources* **2006,** *160* (1), 570-576.
189. Chen, Z. Y.; Zhu, H. L.; Ji, S.; Fakir, R.; Linkov, V., Influence of carbon sources on electrochemical performances of $LiFePO_4$/C composites. *Solid State Ionics* **2008,** *179* (27), 1810-1815.

190. Toprakci, O.; Toprakci, H. A.; Ji, L.; Zhang, X., Fabrication and electrochemical characteristics of $LiFePO_4$ powders for lithium-ion batteries. *KONA Powder and Particle Journal* **2010,** *28* (0), 50-73.
191. Sun, X.; Sun, K.; Chen, C.; Sun, H.; Cui, B., Controlled Preparation and Surface Structure Characterization of Carbon-Coated Lithium Iron Phosphate and Electrochemical Studies as Cathode Materials for Lithium Ion Battery. *International Journal of Materials and Chemistry* **2012,** *2* (5), 218-224.
192. Wang, G.; Liu, H.; Liu, J.; Qiao, S.; Lu, G. M.; Munroe, P.; Ahn, H., Mesoporous $LiFePO_4$/C nanocomposite cathode materials for high power lithium ion batteries with superior performance. *Advanced Materials* **2010,** *22* (44), 4944-4948.
193. Wilcox, J. D.; Doeff, M. M.; Marcinek, M.; Kostecki, R., Factors Influencing the Quality of Carbon Coatings on $LiFePO_4$. *Journal of The Electrochemical Society* **2007,** *154* (5), A389-A395.
194. Kuo, H. T.; Chan, T. S.; Bagkar, N. C.; Liu, R. S.; Shen, C. H.; Shy, D. S.; Xing, X. K.; Lee, J.-F., Effect of LiI Amount to Enhance the Electrochemical Performance of Carbon-Coated $LiFePO_4$. *Electrochemical and Solid-State Letters* **2009,** *12* (6), A111-A114.
195. Oh, S. W.; Myung, S.-T.; Bang, H. J.; Yoon, C. S.; Amine, K.; Sun, Y.-K., Nanoporous Structured $LiFePO_4$ with Spherical Microscale Particles Having High Volumetric Capacity for Lithium Batteries. *Electrochemical and Solid-State Letters* **2009,** *12* (9), A181-A185.
196. Liu, J.; Conry, T. E.; Song, X.; Yang, L.; Doeff, M. M.; Richardson, T. J., Spherical nanoporous $LiCoPO_4$/C composites as high performance cathode materials for rechargeable lithium-ion batteries. *Journal of Materials Chemistry* **2011,** *21* (27), 9984-9987.
197. Van Aken, P.; Liebscher, B.; Styrsa, V., Quantitative determination of iron oxidation states in minerals using Fe $L_{2,3}$-edge electron energy-loss near-edge structure spectroscopy. *Physics and Chemistry of Minerals* **1998,** *25* (5), 323-327.
198. Laffont, L.; Delacourt, C.; Gibot, P.; Wu, M. Y.; Kooyman, P.; Masquelier, C.; Tarascon, J. M., Study of the $LiFePO_4/FePO_4$ two-phase system by high-resolution electron energy loss spectroscopy. *Chemistry of Materials* **2006,** *18* (23), 5520-5529.
199. Wang, F.; Graetz, J.; Moreno, M. S.; Ma, C.; Wu, L.; Volkov, V.; Zhu, Y., Chemical distribution and bonding of lithium in intercalated graphite: Identification with optimized electron energy loss spectroscopy. *ACS Nano* **2011,** *5* (2), 1190-1197.
200. Porcher, W.; Moreau, P.; Lestriez, B.; Jouanneau, S.; Guyomard, D., Is $LiFePO_4$ Stable in Water? Toward Greener Li–Ion Batteries. *Electrochemical and Solid-State Letters* **2008,** *11* (1), A4-A8.
201. Sinha, N. N.; Shivakumara, C.; Munichandraiah, N., High rate capability of a dual-porosity $LiFePO_4$/C composite. *ACS Applied Materials & Interfaces* **2010,** *2* (7), 2031-2038.
202. Zhang, J.; Zhuo, L.; Zhang, L.; Wu, C.; Zhang, X.; Wang, L., Synthesis and electrochemical properties of $LiFePO_4$/C composite cathode material prepared by a

new route using supercritical carbon dioxide as a solvent. *Journal of Materials Chemistry* **2011,** *21* (19), 6975-6980.
203. Doeff, M. M.; Wilcox, J. D.; Yu, R.; Aumentado, A.; Marcinek, M.; Kostecki, R., Impact of carbon structure and morphology on the electrochemical performance of $LiFePO_4$/C composites. *Journal of Solid State Electrochemistry* **2008,** *12* (7-8), 995-1001.
204. Sides, C. R.; Croce, F.; Young, V. Y.; Martin, C. R.; Scrosati, B., A High-Rate, Nanocomposite $LiFePO_4$/Carbon Cathode. *Electrochemical and Solid-State Letters* **2005,** *8* (9), A484-A487.
205. Bhuvaneswari, M.; Bramnik, N. N.; Ensling, D.; Ehrenberg, H.; Jaegermann, W., Synthesis and characterization of Carbon Nano Fiber/$LiFePO_4$ composites for Li-ion batteries. *Journal of Power Sources* **2008,** *180* (1), 553-560.
206. Lu, J.; Tang, Z.; Zhang, Z.; Shen, W., Preparation of $LiFePO_4$ with inverse opal structure and its satisfactory electrochemical properties. *Materials Research Bulletin* **2005,** *40* (12), 2039-2046.
207. Yu, F.; Zhang, J.-J.; Yang, Y.-F.; Song, G.-Z., Up-scalable synthesis, structure and charge storage properties of porous microspheres of $LiFePO_4$@C nanocomposites. *Journal of Materials Chemistry* **2009,** *19* (48), 9121-9125.
208. Ellis, B.; Perry, L. K.; Ryan, D. H.; Nazar, L., Small Polaron Hopping in Li_xFePO_4 Solid Solutions: Coupled Lithium-Ion and Electron Mobility. *Journal of the American Chemical Society* **2006,** *128* (35), 11416-11422.
209. Brunetti, G.; Robert, D.; Bayle-Guillemaud, P.; Rouviere, J.; Rauch, E.; Martin, J.; Colin, J.; Bertin, F.; Cayron, C., Confirmation of the domino-cascade model by $LiFePO_4$/$FePO_4$ precession electron diffraction. *Chemistry of Materials* **2011,** *23* (20), 4515-4524.
210. Sharma, N.; Guo, X.; Du, G.; Guo, Z.; Wang, J.; Wang, Z.; Peterson, V. K., Direct evidence of concurrent solid-solution and two-phase reactions and the nonequilibrium structural evolution of $LiFePO_4$. *Journal of the American Chemical Society* **2012,** *134* (18), 7867-7873.
211. Bai, P.; Cogswell, D. A.; Bazant, M. Z., Suppression of phase separation in $LiFePO_4$ nanoparticles during battery discharge. *Nano Letters* **2011,** *11* (11), 4890-4896.
212. Seo, D. H.; Gwon, H.; Kim, S. W.; Kim, J.; Kang, K., Multicomponent olivine cathode for lithium rechargeable batteries: a first-principles study. *Chemistry of Materials* **2009,** *22* (2), 518-523.
213. Zaghib, K.; Mauger, A.; Gendron, F.; Julien, C., Surface effects on the physical and electrochemical properties of thin $LiFePO_4$ particles. *Chemistry of Materials* **2007,** *20* (2), 462-469.
214. Julien, C. M.; Mauger, A.; Zaghib, K., Surface effects on electrochemical properties of nano-sized $LiFePO_4$. *Journal of Materials Chemistry* **2011,** *21* (27), 9955-9968.
215. Malik, R.; Abdellahi, A.; Ceder, G., A critical review of the Li insertion mechanisms in $LiFePO_4$ electrodes. *Journal of The Electrochemical Society* **2013,** *160* (5), A3179-A3197.

216. Trudeau, M.; Laul, D.; Veillette, R.; Serventi, A.; Mauger, A.; Julien, C.; Zaghib, K., In situ high-resolution transmission electron microscopy synthesis observation of nanostructured carbon coated $LiFePO_4$. *Journal of Power Sources* **2011,** *196* (18), 7383-7394.
217. Teng, F.; Santhanagopalan, S.; Lemmens, R.; Geng, X.; Patel, P.; Meng, D. D., In situ growth of $LiFePO_4$ nanorod arrays under hydrothermal condition. *Solid State Sciences* **2010,** *12* (5), 952-955.
218. Li, Z.; Zhang, D.; Yang, F., Developments of lithium-ion batteries and challenges of $LiFePO_4$ as one promising cathode material. *Journal of Materials Science* **2009,** *44* (10), 2435-2443.
219. Liu, H.; Cao, Q.; Fu, L. J.; Li, C.; Wu, Y.; Wu, H., Doping effects of zinc on $LiFePO_4$ cathode material for lithium ion batteries. *Electrochemistry Communications* **2006,** *8* (10), 1553-1557.
220. Molenda, J.; Ojczyk, W.; Marzec, J., Electrical conductivity and reaction with lithium of $LiFe_{1-y}Mn_yPO_4$ olivine-type cathode materials. *Journal of Power Sources* **2007,** *174* (2), 689-694.
221. Chen, Y.-W.; Chen, J.-S., A study of electrochemical performance of $LiFePO_4$/C composites doped with Na and V. *Int. J. Electrochem. Sci* **2012,** *7*, 8128-8139.
222. Jheng, S.-C.; Chen, J.-S., The Synthesis of $LiFePO_4$/C Composite by the Precipitation Between Two Water/Oil Emulsions. *Int. J. Electrochem. Sci* **2013,** *8*, 4901-4913.
223. Ma, Z.; Shao, G.; Wang, G.; Du, J.; Zhang, Y., Electrochemical performance of Mo-doped $LiFePO_4$/C composites prepared by two-step solid-state reaction. *Ionics* **2013,** *19* (3), 437-443.
224. Song, J.; Zhang, Y.; Shao, G., Comparing the electrochemical performance of $LiFePO_4$/C modified by Mg doping and MgO coating. *Journal of Nanomaterials* **2013,** *2013*, 6.
225. Etacheri, V.; Marom, R.; Elazari, R.; Salitra, G.; Aurbach, D., Challenges in the development of advanced Li-ion batteries: a review. *Energy & Environmental Science* **2011,** *4* (9), 3243-3262.
226. Bruce, P. G.; Scrosati, B.; Tarascon, J. M., Nanomaterials for rechargeable lithium batteries. *Angewandte Chemie International Edition* **2008,** *47* (16), 2930-2946.
227. Wang, G.; Bradhurst, D.; Dou, S.; Liu, H., Spinel Li $[Li_{1/3}Ti_{5/3}]O_4$ as an anode material for lithium ion batteries. *Journal of Power Sources* **1999,** *83* (1), 156-161.
228. Leonidov, I.; Leonidova, O.; Perelyaeva, L.; Samigullina, R.; Kovyazina, S.; Patrakeev, M., Structure, ionic conduction, and phase transformations in lithium titanate $Li_4Ti_5O_{12}$. *Physics of the Solid State* **2003,** *45* (11), 2183-2188.
229. Aldon, L.; Kubiak, P.; Womes, M.; Jumas, J.; Olivier-Fourcade, J.; Tirado, J.; Corredor, J.; Pérez Vicente, C., Chemical and electrochemical Li-insertion into the $Li_4Ti_5O_{12}$ spinel. *Chemistry of Materials* **2004,** *16* (26), 5721-5725.
230. Wilkening, M.; Amade, R.; Iwaniak, W.; Heitjans, P., Ultraslow Li diffusion in spinel-type structured $Li_4Ti_5O_{12}$ - a comparison of results from solid state NMR and

impedance spectroscopy. *Physical Chemistry Chemical Physics,* **2007,** *9* (10), 1239-46.

231. Sorensen, E. M.; Barry, S. J.; Jung, H.-K.; Rondinelli, J. M.; Vaughey, J. T.; Poeppelmeier, K. R., Three-dimensionally ordered macroporous $Li_4Ti_5O_{12}$: effect of wall structure on electrochemical properties. *Chemistry of Materials* **2006,** *18* (2), 482-489.
232. Mukai, K.; Kato, Y.; Nakano, H., Understanding the Zero-Strain Lithium Insertion Scheme of $Li[Li_{1/3}Ti_{5/3}]O_4$: Structural Changes at Atomic Scale Clarified by Raman Spectroscopy. *The Journal of Physical Chemistry C* **2014,** *118* (6), 2992-2999.
233. Xie, H. M.; Wang, R. S.; Ying, J. R.; Zhang, L. Y.; Jalbout, A. F.; Yu, H. Y.; Yang, G. L.; Pan, X. M.; Su, Z. M., Optimized $LiFePO_4$-Polyacene Cathode Material for Lithium-Ion Batteries. *Advanced Materials* **2006,** *18* (19), 2609-2613.
234. Cheng, L.; Liu, H. J.; Zhang, J. J.; Xiong, H. M.; Xia, Y. Y., Nanosized $Li_4Ti_5O_{12}$ prepared by molten salt method as an electrode material for hybrid electrochemical supercapacitors. *Journal of the Electrochemical Society* **2006,** *153* (8), A1472-A1477.
235. Jiang, C.; Hosono, E.; Ichihara, M.; Honma, I.; Zhou, H., Synthesis of nanocrystalline $Li_4Ti_5O_{12}$ by chemical lithiation of anatase nanocrystals and postannealing. *Journal of The Electrochemical Society* **2008,** *155* (8), A553-A556.
236. Yin, S.; Song, L.; Wang, X.; Zhang, M.; Zhang, K.; Zhang, Y., Synthesis of spinel $Li_4Ti_5O_{12}$ anode material by a modified rheological phase reaction. *Electrochimica Acta* **2009,** *54* (24), 5629-5633.
237. Ji, S.; Zhang, J.; Wang, W.; Huang, Y.; Feng, Z.; Zhang, Z.; Tang, Z., Preparation and effects of Mg-doping on the electrochemical properties of spinel $Li_4Ti_5O_{12}$ as anode material for lithium ion battery. *Materials Chemistry and Physics* **2010,** *123* (2-3), 510-515.
238. Huang, S.; Wen, Z.; Zhu, X.; Yang, X., Research on $Li_4Ti_5O_{12}$/Cu_xO Composite Anode Materials for Lithium-Ion Batteries. *Journal of the Electrochemical Society* **2005,** *152* (7), A1301-A1305.
239. Huang, S.; Wen, Z.; Yang, X.; Gu, Z.; Xu, X., Improvement of the high-rate discharge properties of $LiCoO_2$ with the Ag additives. *Journal of Power Sources* **2005,** *148*, 72-77.
240. Bai, Y.-J.; Gong, C.; Qi, Y.-X.; Lun, N.; Feng, J., Excellent long-term cycling stability of La-doped $Li_4Ti_5O_{12}$ anode material at high current rates. *Journal of Materials Chemistry* **2012,** *22* (36), 19054-19060.
241. Song, H.; Yun, S.-W.; Chun, H.-H.; Kim, M.-G.; Chung, K. Y.; Kim, H. S.; Cho, B.-W.; Kim, Y.-T., Anomalous decrease in structural disorder due to charge redistribution in Cr-doped $Li_4Ti_5O_{12}$ negative-electrode materials for high-rate Li-ion batteries. *Energy & Environmental Science* **2012,** *5* (12), 9903-9913.
242. Yuan, T.; Cai, R.; Shao, Z., Different effect of the atmospheres on the phase formation and performance of $Li_4Ti_5O_{12}$ prepared from ball-milling-assisted solid-phase reaction with pristine and carbon-precoated TiO_2 as starting materials. *The Journal of Physical Chemistry C* **2011,** *115* (11), 4943-4952.

243. Shi, Y.; Wen, L.; Li, F.; Cheng, H.-M., Nanosized $Li_4Ti_5O_{12}$/graphene hybrid materials with low polarization for high rate lithium ion batteries. *Journal of Power Sources* **2011,** *196* (20), 8610-8617.
244. Yang, L.; Gao, L., $Li_4Ti_5O_{12}$/C composite electrode material synthesized involving conductive carbon precursor for Li-ion battery. *Journal of Alloys and Compounds* **2009,** *485* (1-2), 93-97.
245. Jung, H.-G.; Myung, S.-T.; Yoon, C. S.; Son, S.-B.; Oh, K. H.; Amine, K.; Scrosati, B.; Sun, Y.-K., Microscale spherical carbon-coated $Li_4Ti_5O_{12}$ as ultra high power anode material for lithium batteries. *Energy & Environmental Science* **2011,** *4* (4), 1345-1351.
246. Zhu, G.-N.; Liu, H.-J.; Zhuang, J.-H.; Wang, C.-X.; Wang, Y.-G.; Xia, Y.-Y., Carbon-coated nano-sized $Li_4Ti_5O_{12}$ nanoporous micro-sphere as anode material for high-rate lithium-ion batteries. *Energy & Environmental Science* **2011,** *4* (10), 4016-4022.
247. Fang, W.; Cheng, X.; Zuo, P.; Ma, Y.; Yin, G., A facile strategy to prepare nano-crystalline $Li_4Ti_5O_{12}$/C anode material via polyvinyl alcohol as carbon source for high-rate rechargeable Li-ion batteries. *Electrochimica Acta* **2013,** *93*, 173-178.
248. Zhu, Z.; Cheng, F.; Chen, J., Investigation of effects of carbon coating on the electrochemical performance of $Li_4Ti_5O_{12}$/C nanocomposites. *Journal of Materials Chemistry A* **2013,** *1* (33), 9484-9490.
249. Fang, W.; Ma, Y.; Zuo, P.; Cheng, X.; Yin, G., Nano-$Li_4Ti_5O_{12}$ Pore Microspheres: A High Power Electrode Material for Lithium Ion Batteries. *International Journal of Electrochemical Science* **2013,** *8* (2).
250. Wang, C.; Li, H.; Fu, A.; Liu, J.; Ye, W.; Guo, P.; Pang, G.; Zhao, X. S., An RAPET approach to in situ synthesis of carbon modified $Li_4Ti_5O_{12}$ anode nanocrystals with improved conductivity. *New Journal of Chemistry* **2014,** *38* (2), 616.
251. Luo, H.; Shen, L.; Rui, K.; Li, H.; Zhang, X., Carbon coated $Li_4Ti_5O_{12}$ nanorods as superior anode material for high rate lithium ion batteries. *Journal of Alloys and Compounds* **2013,** *572*, 37-42.
252. Guan, X.; Chen, X.; Li, G.; Zang, Y.; Lin, H.; Luo, D.; Li, L., Direct synthesis of carbon-coated $Li_4Ti_5O_{12}$ mesoporous nanoparticles for high-rate lithium-ion batteries. *RSC Advances* **2013,** *3* (9), 3088-3094.
253. Li, X.; Hu, H.; Huang, S.; Yu, G.; Gao, L.; Liu, H.; Yu, Y., Nano-sized $Li_4Ti_5O_{12}$ anode material with excellent performance prepared by solid state reaction: The effect of precursor size and morphology. *Electrochimica Acta* **2013,** *112*, 356-363.
254. Wang, R.; Wang, J.; Qiu, T.; Chen, L.; Liu, H.; Yang, W., Effects of different carbon sources on the electrochemical properties of $Li_4Ti_5O_{12}$/C composites. *Electrochimica Acta* **2012,** *70*, 84-90.
255. Cheng, L.; Yan, J.; Zhu, G.-N.; Luo, J.-Y.; Wang, C.-X.; Xia, Y.-Y., General synthesis of carbon-coated nanostructure $Li_4Ti_5O_{12}$ as a high rate electrode material for Li-ion intercalation. *Journal of Materials Chemistry* **2010,** *20* (3), 595-602.

256. Li, B.; Han, C.; He, Y.-B.; Yang, C.; Du, H.; Yang, Q.-H.; Kang, F., Facile synthesis of $Li_4Ti_5O_{12}$/C composite with super rate performance. *Energy & Environmental Science* **2012,** *5* (11), 9595-9602.
257. Zhu, G.-N.; Wang, C.-X.; Xia, Y.-Y., A Comprehensive Study of Effects of Carbon Coating on $Li_4Ti_5O_{12}$ Anode Material for Lithium-Ion Batteries. *Journal of The Electrochemical Society* **2011,** *158* (2), A102.
258. Ming, H.; Ming, J.; Li, X.; Zhou, Q.; Wang, H.; Jin, L.; Fu, Y.; Adkins, J.; Zheng, J., Hierarchical $Li_4Ti_5O_{12}$ particles co-modified with C&N towards enhanced performance in lithium-ion battery applications. *Electrochimica Acta* **2014,** *116*, 224-229.
259. Wang, Y.; Liu, H.; Wang, K.; Eiji, H.; Wang, Y.; Zhou, H., Synthesis and electrochemical performance of nano-sized $Li_4Ti_5O_{12}$ with double surface modification of Ti (III) and carbon. *Journal of Materials Chemistry* **2009,** *19* (37), 6789-6795.
260. Li, H.; Shen, L.; Yin, K.; Ji, J.; Wang, J.; Wang, X.; Zhang, X., Facile synthesis of N-doped carbon-coated $Li_4Ti_5O_{12}$ microspheres using polydopamine as a carbon source for high rate lithium ion batteries. *Journal of Materials Chemistry A* **2013,** *1* (24), 7270-7276.
261. Zhao, L.; Hu, Y. S.; Li, H.; Chen, L., Porous $Li_4Ti_5O_{12}$ coated with N-doped carbon from ionic liquids for Li-ion batteries. *Advanced Materials* **2011,** *23* (11), 1385-8.
262. Inagaki, M., Carbon coating for enhancing the functionalities of materials. *Carbon* **2012,** *50* (9), 3247-3266.
263. Li, H.; Zhou, H., Enhancing the performances of Li-ion batteries by carbon-coating: present and future. *Chemical Communications* **2012,** *48* (9), 1201-1217.
264. Gaberscek, M.; Jamnik, J., Impact of electrochemical wiring topology on the kinetics of insertion electrodes. *Solid State Ionics* **2006,** *177* (26), 2647-2651.
265. Dominko, R.; Bele, M.; Gaberscek, M.; Remskar, M.; Hanzel, D.; Pejovnik, S.; Jamnik, J., Impact of the carbon coating thickness on the electrochemical performance of $LiFePO_4$/C composites. *Journal of the Electrochemical Society* **2005,** *152* (3), A607-A610.
266. Sun, X.; Hegde, M.; Zhang, Y.; He, M.; Gu, L.; Wang, Y.; Shu, J.; Radovanovic, P. V.; Cui, B., Structure and Electrochemical Properties of Spinel $Li_4Ti_5O_{12}$ Nanocomposites as Anode for Lithium-Ion Battery. *Int. J. Electrochem. Sci* **2014,** *9*, 1583-1596.
267. http://unicorn.mcmaster.ca/aXis2000.html.
268. Wang, J.; Liu, X.-M.; Yang, H.; Shen, X.-D., Characterization and electrochemical properties of carbon-coated $Li_4Ti_5O_{12}$ prepared by a citric acid sol–gel method. *Journal of Alloys and Compounds* **2011,** *509* (3), 712-718.
269. Pennycook, S., Z-contrast STEM for materials science. *Ultramicroscopy* **1989,** *30* (1), 58-69.

270. Van Aert, S.; Batenburg, K. J.; Rossell, M. D.; Erni, R.; Van Tendeloo, G., Three-dimensional atomic imaging of crystalline nanoparticles. *Nature* **2011,** *470* (7334), 374-377.
271. LeBeau, J. M.; Findlay, S. D.; Allen, L. J.; Stemmer, S., Standardless atom counting in scanning transmission electron microscopy. *Nano Letters* **2010,** *10* (11), 4405-4408.
272. Lu, X.; Zhao, L.; He, X.; Xiao, R.; Gu, L.; Hu, Y. S.; Li, H.; Wang, Z.; Duan, X.; Chen, L., Lithium storage in $Li_4Ti_5O_{12}$ spinel: the full static picture from electron microscopy. *Advanced Materials* **2012,** *24* (24), 3233-3238.
273. Sun, Y.; Zhao, L.; Pan, H.; Lu, X.; Gu, L.; Hu, Y.-S.; Li, H.; Armand, M.; Ikuhara, Y.; Chen, L., Direct atomic-scale confirmation of three-phase storage mechanism in $Li_4Ti_5O_{12}$ anodes for room-temperature sodium-ion batteries. *Nature Communications* **2013,** *4*, 1870.
274. Su, D.; Wang, F.; Ma, C.; Jiang, N., Engineering nano-composite $Li_4Ti_5O_{12}$ anodes via scanning electron-probe fabrication. *Nano Energy* **2013,** *2* (3), 343-350.
275. Wang, Y.-Q.; Gu, L.; Guo, Y.-G.; Li, H.; He, X.-Q.; Tsukimoto, S.; Ikuhara, Y.; Wan, L.-J., Rutile-TiO_2 nanocoating for a high-rate $Li_4Ti_5O_{12}$ anode of a lithium-ion battery. *Journal of the American Chemical Society* **2012,** *134* (18), 7874-7879.
276. Lippens, P.-E.; Womes, M.; Kubiak, P.; Jumas, J.-C.; Olivier-Fourcade, J., Electronic structure of the spinel $Li_4Ti_5O_{12}$ studied by ab initio calculations and X-ray absorption spectroscopy. *Solid State Sciences* **2004,** *6* (2), 161-166.
277. Peng-Fei, Y.; Zhong-Hui, C.; Jian-Wei, M.; Xiang-Xin, G., Variation of Ti Valence with Lithium Content in Lithiated/Delithiated $Li_4Ti_5O_{12}$ Studied by X-Ray Absorption near the Edge Structure. *Chinese Physics Letters* **2013,** *30* (3), 036102.
278. Sun, X.; Hegde, M.; Wang, J.; Zhang, Y.; Liao, J.; Radovanovic, P. V.; Cui, B., Structural Analysis and Electrochemical Studies of Carbon Coated $Li_4Ti_5O_{12}$ Particles Used as Anode for Lithium-Ion Battery. *ECS Transactions* **2014,** *58* (14), 79-88.
279. Yang, S.; Wang, D.; Liang, G.; Yiu, Y. M.; Wang, J.; Liu, L.; Sun, X.; Sham, T.-K., Soft X-ray XANES studies of various phases related to $LiFePO_4$ based cathode materials. *Energy & Environmental Science* **2012,** *5* (5), 7007-7016.
280. Venkateswarlu, M.; Chen, C. H.; Do, J. S.; Lin, C. W.; Chou, T. C.; Hwang, B. J., Electrochemical properties of nano-sized $Li_4Ti_5O_{12}$ powders synthesized by a sol–gel process and characterized by X-ray absorption spectroscopy. *Journal of Power Sources* **2005,** *146* (1–2), 204-208.
281. Song, H.; Jeong, T.-G.; Moon, Y. H.; Chun, H.-H.; Chung, K. Y.; Kim, H. S.; Cho, B. W.; Kim, Y.-T., Stabilization of Oxygen-deficient Structure for Conducting $Li_4Ti_5O_{12}$ by Molybdenum Doping in a Reducing Atmosphere. *Scientific Reports* **2014,** *4*.
282. Jung, H. G.; Jang, M. W.; Hassoun, J.; Sun, Y.-K.; Scrosati, B., A high-rate long-life $Li_4Ti_5O_{12}$/Li $[Ni_{0.45}Co_{0.1}Mn_{1.45}]$ O_4 lithium-ion battery. *Nature Communications* **2011,** *2*, 516.
283. Tang, J.; Gao, L., Electrochemical performance of $Li_4Ti_5O_{12}$/C anode material prepared with a stearic acid carbon source. *Physica Scripta* **2012,** *85* (4), 045802.

284. Li, B.; Ning, F.; He, Y.-B.; Du, H.; Yang, Q.-H.; Ma, J.; Kang, F.; Hsu, C.-T., Synthesis and Characterization of Long Life $Li_4Ti_5O_{12}$/C Composite Using Amorphous TiO_2 Nanoparticles. *International Journal of Electrochemical Science* **2011,** *6*.
285. Chen, J.; Yang, L.; Fang, S.; Tang, Y., Synthesis of sawtooth-like $Li_4Ti_5O_{12}$ nanosheets as anode materials for Li-ion batteries. *Electrochimica Acta* **2010,** *55* (22), 6596-6600.
286. Hong, Z.; Zheng, X.; Ding, X.; Jiang, L.; Wei, M.; Wei, K., Complex spinel titanate nanowires for a high rate lithium-ion battery. *Energy & Environmental Science* **2011,** *4* (5), 1886-1891.
287. Yuan, T.; Cai, R.; Wang, K.; Ran, R.; Liu, S.; Shao, Z., Combustion synthesis of high-performance $Li_4Ti_5O_{12}$ for secondary Li-ion battery. *Ceramics International* **2009,** *35* (5), 1757-1768.
288. Shenouda, A. Y.; Murali, K., Electrochemical properties of doped lithium titanate compounds and their performance in lithium rechargeable batteries. *Journal of Power Sources* **2008,** *176* (1), 332-339.
289. Li, X.; Qu, M.; Huai, Y.; Yu, Z., Preparation and electrochemical performance of $Li_4Ti_5O_{12}$/carbon/carbon nano-tubes for lithium ion battery. *Electrochimica Acta* **2010,** *55* (8), 2978-2982.
290. Liu, G.; Kuo, H.; Liu, R.; Shen, C.; Shy, D.; Xing, X.; Chen, J., Study of electrochemical properties of coating ZrO_2 on $LiCoO_2$. *Journal of Alloys and Compounds* **2010,** *496* (1), 512-516.
291. Chou, S.-L.; Wang, J.-Z.; Liu, H.-K.; Dou, S.-X., Rapid synthesis of $Li_4Ti_5O_{12}$ microspheres as anode materials and its binder effect for lithium-ion battery. *The Journal of Physical Chemistry C* **2011,** *115* (32), 16220-16227.